Multiphoton Absorption and Multiphoton Excited Photoluminescence in Transition-Metal-Doped ZnSe/ZnS Quantum Dots

XING GUICHUAN

(B. Sc. Fudan University)

A THESIS SUBMITTED

FOR THE DEGREE OF DOCTOR OF PHILOSOPHY

DEPARTMENT OF PHYSICS

NATIONAL UNIVERSITY OF SINGAPORE

2010

ACKNOWLEDGEMENTS

It is my great pleasure to have this opportunity to thank the following people who have been important in helping me complete this thesis. Their assistance and support have been invaluable to me at various stages of this long and enduring journey.

First and foremost, I would like to express my heartfelt appreciation to my supervisors, Prof. Ji Wei and Asst. Prof. Xu Qing-Hua, for their unfailing and indispensable guidance, constructive criticism and constant encouragement in guiding me through my thesis.

I would like to express my sincerest gratitude to Asst. Prof. Tze Chien Sum, and Prof. Cheng Hon Alfred Huan (NTU), for their support and guidance; Sincerest appreciation to Dr. Zheng Yuangang and Prof. Jackie Y. Ying (Institute of Bioengineering and Nanotechnology), for providing the precious semiconductor quantum dot samples.

I would wish to express my appreciation to my group members and friends in NUS. To Dr. Qu Yingli, Mr. Mi Jun, Mr. Mohan Singh Dhoni, Mr. Chen Weizhe, Dr. He Jun, Dr. Hendry Izaac Elim and Dr. Li Heping for their kind support and fruitful discussions. To Dr. Guo Hongchen, Dr. Liu Weiming, Dr. You Guanzhong, Dr. Pan Hui, Mr. Sha Zhengdong, Dr. Fan Haiming and Dr. Chen Ao, for their cooperation, valuable discussion and help.

I would thank my parents and sisters, for their support, tolerance, consistent understanding, encouragement and love.

Particularly, I should thank my wife, Qi Chenyue, for her believing and understanding, everlasting support and love.

Table of Contents

SUMMARY

This thesis presents the nonlinear optical investigations of the multiphoton absorption (MPA) and multiphoton excited charge carrier dynamics in ZnSe/ZnS and transition-metal-doped ZnSe/ZnS core/shell semiconductor quantum dots (QDs).

In view of the applications of semiconductor QDs in multiphoton bio-imaging, upconversion lasing and three dimension data storage, the 2PA, 3PA and the MPA generated charge carrier dynamics in ZnSe/ZnS and Cu- and Mn-doped ZnSe/ZnS QDs were systematically investigated. Transition metal doping not only greatly enhanced the quantum yields of semiconductor QDs, but also greatly enlarged the 2PA and 3PA cross-sections. The later was mainly caused by the introduction of new doping and defect energy levels by the incorporated transition metal ions. Transition metal doping provided an option to manipulate MPA cross-sections, in addition to adjusting the size of semiconductor QDs. With this method, the tailoring of MPA cross-sections and emission wavelengths could be simultaneously realized with varying the dopant and size of the QDs. We also developed an experimental method to separate the 2PA and 3PA contributions in semiconductor QDs when the excitation photon energy was near half of the bandgap. The work in this thesis is grouped into four parts as follows.

The first, 3PA and three-photon-excited photoluminescence (PL) of ZnSe/ZnS and Zn(Cu)Se/ZnS QDs in aqueous solutions have been unambiguously determined by Z-scan and PL measurements with femtosecond laser pulses at 1000 nm, which is close to a semi-transparent window for many biological specimens. The 3PA cross-section is as high as 3.5×10^{-77} cm^6 s^2 photon^{-2} for the 4.1-nm-sized, Zn(Cu)Se/ZnS QDs, while their

below-band-edge PL has a nearly cubic dependence on excitation intensity, with a quantum efficiency enhanced by ~ 20 fold compared to the undoped ZnSe/ZnS QDs.

Secondly, previous studies on the MPA in semiconductor QDs were mainly focused in $E_g/2 < \hbar w < E_g$ range for 2PA and in $E_g/3 < \hbar w < E_g/2$ range for 3PA. When the photon energy is near half of the QDs bandgap energy, both the 2PA and 3PA have significant contributions to the nonlinear absorption. The contributions of 2PA and 3PA in this regime have never been previously investigated. In this thesis we have demonstrated that the 2PA and 3PA of semiconductor QDs in a matrix can be unambiguously determined under this situation. In the spectral region where the photon energy is greater than but near $E_g/2$, the 2PA coefficient is determined by open-aperture Z-scans at relatively lower irradiances, and the 3PA coefficient is then extracted from open-aperture Z-scans conducted at higher irradiances. At photon energies below but close to $E_g/2$, both open-aperture Z-scans and multiphoton-excited PL measurements have to be employed to distinguish 2PA from 3PA.

Next, with the above method, the 3PA of 4.4-nm-sized ZnSe/ZnS QDs and 4.1-nm-sized Mn-doped ZnSe/ZnS QDs have been unambiguously determined in a wide spectrum range (from 800 nm to 1064 nm). The two-photon-enhanced 3PA in transition-metal-doped ZnSe/ZnS QDs has been revealed by comparing the theoretically calculated 3PA cross-sections with the experimentally measured ones in the near infrared spectral region. Due to the degeneracy between two-photon transitions mainly to the states of dopants and three-photon transitions to excitionic states, the 3PA cross-section is enhanced by two orders of magnitude at 1064 nm. Taking into account the enhancement in the PL, such double enhancements make ZnSe/ZnS QDs doped with transition-metal ions a promising candidate for applications based on three-photon-excited fluorescence.

Lastly, we have shown that the transition-metal-doping greatly enhanced PL can be further increased by directly exciting the electrons from the ground states to the defect states rather than to the conduction bands in ZnSe/ZnS QDs. At an optimal wavelength of commercial Ti:sapphire femtosecond laser (800 nm); despite a reduction of the 2PA cross-section when the QD size is decreased from 4.1 nm to 3.2 nm, the overall two photon action cross-section ($\sigma_2\eta$) is increased due to the greatly enhanced quantum yield. The 2PA generated electrons exhibit a single exponential decay (~ 580 ns) from the copper-related defect states to the t_2 energy level of Cu^{2+} ions. These results open a new avenue for the application of Cu-doped semiconductor QDs in upconversion lasing, multiphoton bio-imaging and three dimensional optical data storage.

LIST OF TABLES

LIST OF FIGURES

LIST OF PUBLICATIONS

1. **“**Fe_3O_4-Ag nanocomposites for optical limiting: broad temporal response and low threshold,”
G. C. Xing, J. Jiang, J. Y. Ying, and W. Ji, **Opt. Express 18**, 6183 (2010).

2. “Surface Plasmon enhanced third-order nonlinear optical effects in Ag-Fe_3O_4 nanocomposites,”
V. Mamidala, **G. C. Xing**, and W. Ji, **J. Phys. Chem. C 114**, 22466 (2010).

3. “Two-photon-enhanced three-photon absorption in transition-metal-doped semiconductor quantum dots,” (Invited)
X. B. Feng, **G. C. Xing**, and W. Ji, **J. Opt. A 11**, 024004 (2009).

4. “Two- and three-photon absorption of semiconductor quantum dots in the vicinity of half of lowest exciton energy,”
G. C. Xing, W. Ji, Y. G. Zheng, and J. Y. Ying, **Appl. Phys. Lett. 93**, 241114 (2008).

5. **“**High efficiency and nearly cubic power dependence of below-band-edge photoluminescence in water-soluble, copperdoped ZnSe/ZnS Quantum dots,”
G. C. Xing, W. Ji, Y. G. Zheng, and J. Y. Ying, **Opt. Express 16**, 5715 (2008).

6. “Novel CdS Nanostructures: Synthesis and Field Emission,”
H. Pan, C. K. Poh, Y. W. Zhu, **G. C. Xing**, K. C. Chin, Y. P. Feng, J. Y. Lin, C. H. Sow, W. Ji, and A. T. S. Wee, **J. Phys. Chem. C 112**, 11227 (2008).

7. “Color tunable organic light-emitting diodes using coumarin dopants,”
Z. W. Xu, G. H. Ding, G. Y. Zhong, **G. C. Xing**, F. Y. Li, W. Huang, and H. Tian, **Res. Chem. Intermed. 34**, 249 (2008).

8. "Stimulated emission of CdS nanowires grown by thermal evaporation,"
H. Pan, **G. C. Xing**, Z. H. Ni, W. Ji, and Y. P. Feng, **Appl. Phys. Lett. 91**, 193105 (2007).

9. "Two-dimensional AlGaInP/GaInP photonic crystal membrance lasers operating in the visible regime at room temperature,"
A. Chen, S. J. Chua, **G. C. Xing**, W. Ji, X. H. Zhang, J. R. Dong, L. K. Jian, and E. A. Fitzgerald, **Appl. Phys. Lett. 90**, 011113 (2007).

PATENT:

1. "Optical Limiting with Nanohybrid Composites,"
J. Y. Ying, W. Ji, J. Jiang, and **G. C. Xing**, RI File Ref: IBN-231, filed by the US provisional application in 2009.

Chapter 1

Introduction

1.1 Background

Semiconductor quantum dots (QDs), also known as nanocrystals, are fragments of semiconductor consisting of hundreds to several thousands of atoms with the bulk bonding geometry. They usually are a few nanometers in diameter and their size and shape can be precisely controlled by the duration, temperature, and ligand molecules used in the synthesis. [1.1] The synthesized semiconductor QDs are free-standing or embedded in a material which has a larger bandgap. Due to their small size and high potential well for the delocalized electrons and holes, QDs have molecular-like discrete energy levels which exhibit strong size dependence. [1.2] This provides an opportunity for a wide-range tailoring of their electronic and optical properties. These controllable physical and chemical properties, narrow and symmetric photoluminescence (PL) as well as broad and intense absorption of luminescent semiconductor QDs have attracted tremendous attention in the last decade for their potential application as biomedical imaging labels, light emitting diodes (LEDs), upconversion lasers, solar cells and sensors, etc. [1.2]

Among the II-VI and III-V semiconductors, cadmium chalcogenides, especially CdSe and related core/shell QDs are the focus of many research efforts for their high quantum efficiency and easy processing. [1.1, 1.3] However, experimental results indicate that any leakage of cadmium from these QDs would be toxic and fatal to a biological system; [1.4] and cadmium products are environmentally unfriendly. This puts a big disadvantage for practical applications. For this reason, scientists now are trying to find substitution for cadmium-related QDs. Manganese (Mn)- and Copper (Cu)-doped ZnSe QDs are shown to be very promising candidates. [1.5] These transition-metal-doped QDs have many advantages compared to the traditional semiconductor QDs, such as low toxicity, reduced self-quenching due to large Stokes shift, greatly suppressed host emission, and improved stabilities over thermal, chemical, and photochemical disturbances. [1.4]

For potential high-power applications, such as multiphoton biomedical imaging labels, LEDs and QD lasers, the nonlinear optical and ultra-fast dynamical properties of these transition-metal-doped QDs must be fully understood. [1.6] Nonlinear optics and ultra-fast dynamics were developed in the 1960s after the invention of lasers. They have been systematically investigated and exploited in the realization of various technological and industrial applications in the last two decades, but these applications are still limited by the existing nonlinear materials. Among various nonlinear materials, semiconductor QDs are very promising candidates for these nonlinear optical applications. The idea is that optical nonlinearity of the semiconductor QDs can be enhanced by artificially confining the electrons and holes in regions smaller than their natural delocalization length in the bulk. This enhancement is also called quantum confinement effect, which was discovered by Jain and Lind in 1983. [1.7]

To give a clear understanding of the nonlinear mechanisms and ultrafast carrier dynamics as well as their relation to the electronic structure of the transition-metal-doped semiconductor QDs, a concise review of the semiconductor QDs, transition-metal-doped QDs and their nonlinear optical and dynamical properties will be given below.

1.2 Previous research on semiconductor QDs and transition-metal-doped semiconductor QDs

1.2.1 Semiconductor QDs

Semiconductor QDs were first discovered by Louis E. Brus at Bell Labs in 1983 [1.8] and was termed as "Quantum Dot" by Mark Reed at Yale University [1.9]. In bulk semiconductor, an electron and a hole can easily form an electron-hole pair (or exciton), which is a hydrogen like bound state that forms due to the Coulomb attraction between the electron and hole. A semiconductor QD is a semiconductor whose excitons are confined in all three spatial dimensions. Accordingly, they have properties that are between those of bulk semiconductor and those of discrete molecules. QDs are nanocrystalline materials (or materials that contain nanocrystals) in which the dimension of the crystal is smaller (in all directions) than the Bohr radius (a_B) of the exciton. The Bohr radius is used to describe the natural length scale of the electron, hole or exciton and is defined as:

$$a_B = \varepsilon \frac{m}{m^*} a_0 \tag{1.1}$$

where ε is the dielectric constant of the material, m^* is the mass of the particle (electron, hole or exciton), m is the rest mass of the electron, and a_0 is the Bohr radius of the hydrogen atom [1.10]. For semiconductor, there are three different Bohr radii: one for the electron (a_e), one for the hole (a_h), and one for the exciton (a_{exc}). With these values, three different kinds of confinement can be defined. First, if the nanocrystal radius, R, is much smaller than a_e, a_h, and a_{exc} (i.e. $R < a_e, a_h, a_{exc}$), the electron and hole are both strongly confined by the nanocrystal boundary. This is referred to as the strong confinement regime. Second, when R is larger than both a_e and a_h, but is smaller than a_{exc} (i.e. when a_e,

$a_h < R < a_{exc}$), only the center-of-mass motion of the exciton is confined. This limit is called the weak confinement regime. Finally, when R is between a_e and a_h, one particle is strongly confined and the other is not. This is referred to as the intermediate confinement regime.

In bulk semiconductor materials, the electrons have a range of energies. One electron with a different energy from another electron is described as being in a different energy level, and it is established that only two electrons can fit in any given level due to the spin degeneracy. The energy levels are very close together in bulk semiconductor, so close that they are described as continuous, meaning there is almost no energy difference between them. It is also well established that some energy levels are simply off limits to electrons; this region of forbidden electron energies is called the bandgap, and it is different for each bulk material. Electron occupying energy levels below the bandgap are described as being in the valence band. Electrons occupying energy levels above the bandgap are described as being in the conduction band [1.11].

In semiconductor QDs, the small size induced excition confinement split the continuous energy bands of a bulk material to a discrete structure of energy levels (Figure 1.1) [1.12, 1.13]. As the QD size decreases, the energy bandgap splitting increases. This will lead to a blue shift of absorption and emission wavelength. To quantitatively describe the quantum confinement induced energy band splitting, the particle in a sphere model was first utilized in 1982 [1.14, 1.15]. In this model, the semiconductor QD was considered as a sphere with spatial extension larger than the lattice constants. In this range of sizes the crystalline structure of the bulk has already been developed. In bulk crystalline solids according to Bloch's theorem, the electronic behaviors can be described with

$$\mathrm{H}\psi(\vec{r}) = [-\frac{\hbar^2}{2m}\nabla^2 + V(\vec{r})]\psi(\vec{r}) = E\psi(\vec{r}) \tag{1.2}$$

where $V(\vec{r}) = V(\vec{r}+\vec{R})$ is the periodic potential well, $\vec{R}$ is all lattice vectors.

In general, the wave function can be expressed as

$$\psi_{\nu,\vec{k}}(\vec{r}) = e^{i\vec{k}\cdot\vec{r}} u_{\nu,\vec{k}}(\vec{r}) \tag{1.3}$$

where $e^{i\vec{k}\cdot\vec{r}}$ is the envelope function, $u_{\nu,\vec{k}}(\vec{r}) = u_{\nu,\vec{k}}(\vec{r}+\vec{R})$ is the Periodical Block function.

Now in semiconductor QDs with the particle in a sphere model, the charge carrier is considered as a particle of mass m_0 inside a spherical potential well of radius R,

$$r < R; \quad V(r) = 0 \tag{1.4}$$

$$r > R; \quad V(r) = \infty \tag{1.5}$$

Then the wave function can be expanded in products of the cell periodic parts $u_{\nu,\vec{k}}(\vec{r})$ (same as in bulk) of the Bloch functions together with a specific envelope function $\phi(\vec{r})$. If the coulomb interaction is first neglected, the normalized wave function $\phi_i\ (\vec{r})$ for electrons and holes are

$$\phi^i_{nlm}(\vec{r}) = \mathrm{Y}^m_l \cdot \sqrt{\frac{2}{R^3}}\frac{J_l(\chi_{nl}\frac{r}{R})}{J_{l+1}(\chi_{nl})} \tag{1.6}$$

with $-l \le m \le$; l = 0, 1, 2…; n = 1, 2, 3 … here J_l are the Bessel functions, and Y^m_l are the spherical harmonics. The energy of the electron and hole quantum-size levels, can be characterized by angular momentum quantum number l, and can be written in parabolic approximation as

$$E_{nl}^{e,h} = \frac{\hbar^2}{2m_{e,h}} \frac{\chi_{nl}^2}{R^2} \tag{1.7}$$

$m_{e,h}$ is the electron and hole effective mass respectively, χ_{nl} is the n-th zero of the spherical Bessel function of the order l. Labeling the quantum numbers l = 0, 1, 2… with the letters s, p, d…, the first roots are:

$\chi_{1,s} = \pi \quad \chi_{1,p} = 4.493 \quad \chi_{1,d} = 5.763 \quad \chi_{2,s} = 2\pi \quad \chi_{2,p} = 7.725$, etc..

From Equation (1.7), the energy of the lowest electron and hole quantum-size levels increase with decreasing QD size ($\sim 1/R^2$) hence increases the total energy of the band edge optical transitions.

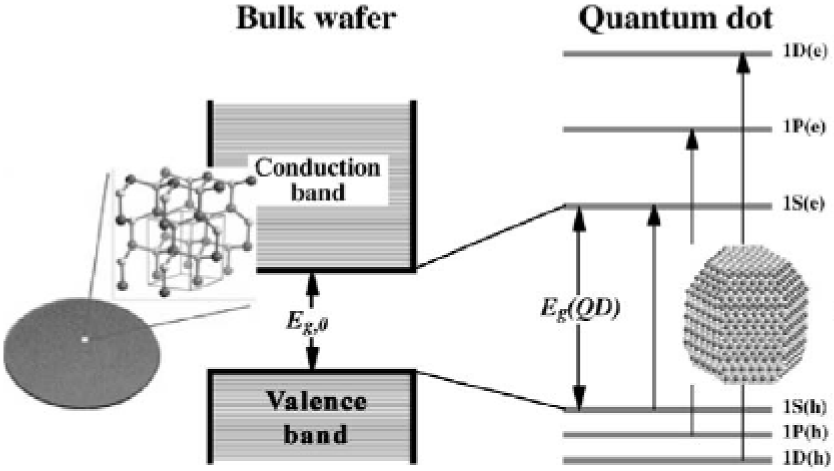

Figure 1.1. Schematical diagram of a semiconductor bulk crystal with continuous conduction and valence energy bands separated by a fixed energy gap, E_{g0}, and a QD discrete atomic like states with energies that are determined by the QD radius R [1.12, 1.13].

With the particle in a sphere model, the one-photon transition in semiconductor QDs can be calculated by using time dependent perturbation theory. Assuming the volume fraction of QDs is f_c, the one-photon absorption (1PA) coefficient can be expressed as [1.16, 1.17]:

$$\alpha(\omega) = 2\frac{\hbar\omega}{I}\frac{2\pi}{\hbar}\frac{f_c}{\frac{4}{3}\pi R^3}\left(\frac{e\left|\vec{A}\right|}{m_0}\right)^2\left|\left\langle \psi_f \middle| \vec{e}\cdot\vec{p} \middle| \psi_i \right\rangle\right|^2 \tag{1.8}$$

where $\vec{e}\cdot\vec{p}$ is dipole operator ($\vec{e}$ denotes the polarization). ψ_i and ψ_f are the initial and the final states of the optical transition, respectively. In QD system:

$$\psi_i(\vec{r}) = u_{vi}\cdot\phi_i(\vec{r})$$

$$\psi_f(\vec{r}) = u_{cf}\cdot\phi_f(\vec{r}) \qquad \phi^i_{nlm}(\vec{r}) = \mathrm{Y}^m_l\cdot\sqrt{\frac{2}{R^3}}\frac{J_l(\chi_{nl}\frac{r}{R})}{J_{l+1}(\chi_{nl})}$$

where *i* and *f* indicate the initial and final states respectively. Here only the interband part is considered. The overlap integral can be rewritten as

$$\left\langle \psi_f \middle| \vec{e}\cdot\vec{p} \middle| \psi_i \right\rangle = \left\langle u_{cf} \middle| \vec{e}\cdot\vec{p} \middle| u_{vi} \right\rangle \cdot \left\langle \phi_f \middle| \phi_i \right\rangle \tag{1.9}$$

The integration can be separated into the integration of the fast oscillating Bloch part and the integration of the envelope part. The integration of the Bloch part results in the size-independent interband dipole matrix element p_{cv} of the bulk. The selection rules originate from the integration of ϕ function over the quantum-dot volume. In the simple particle in a box model, we obtain the well-known selection rule that all transitions conserve n and l.

$$\alpha(\omega) = 2\frac{\hbar\omega}{I}\frac{2\pi}{\hbar}\frac{f_v\left|p_{cv}\right|^2}{\frac{4}{3}\pi R^3}\left(\frac{e\left|\vec{A}\right|}{m_0}\right)^2\sum_{n,l}(2l+1)\cdot\delta(\hbar\omega - E^e_{nl} - E^h_{nl}) \tag{1.10}$$

However, the Coulomb interaction between the optically created electron and hole strongly affects the QD optical spectra; and its energy is on the order of $e^2/\kappa R$, where κ is the dielectric constant of the semiconductor. Because the quantization energy increases with decreasing size as $1/R^2$, the Coulomb energy becomes a small correction to the quantization energies in small crystals ($\leq 2.5nm$) and reduces transition energies by only a relatively small amount. But in large QDs, the Coulomb interaction is more important than the quantization energies. Theoretical analysis shows that the optical properties of QDs strongly depend on the ratio of its radius *R*, to the Bohr radius of the bulk exciton $a_B = \hbar^2\kappa / ue^2$, where *u* is the exciton reduced mass [1.18-1.20]. One needs to consider the three different regimes: $R >> a_B$, $R \approx a_B$ and $R << a_B$. In the strong confinement regime, the electron-hole Coulomb interaction lowers the energy of the transition slightly. The selection rules remain the same: transitions are allowed only between the levels with the same quantum numbers. As a result, the resonant absorption spectra are given by

$$\hbar\omega_v = E_g + E_v^h(R) + E_v^e(R) - 1.8\frac{e^2}{4\pi\varepsilon_0\varepsilon_r R} \tag{1.11}$$

The particle in a sphere model is simple, but no real semiconductors have such simple a parabolic band structure. Fig 1.2 shows the band structure of a typical direct-gap semiconductor with cubic or zinc blende lattice structure (e.g. GaAs, InAs, CdSe, CdTe, CdS, and InSb) and band edge at the Γ point of the Brillouim zone [1.21]. The conduction band is parabolic only at the bottom of the band. The top of the valence band consists of a 4-fold degenerate sub-band, Γ_8, describing the dispersion of the light and heavy hole branches for non-zero *k*, and the spin-orbit split off sub-band Γ_7. The simple parabolic band approximation is useful only for obtaining a qualitative understanding, not for a quantitative description, of the optical properties of real semiconductors. The optical properties of small QDs arise from transitions between the quantum levels of

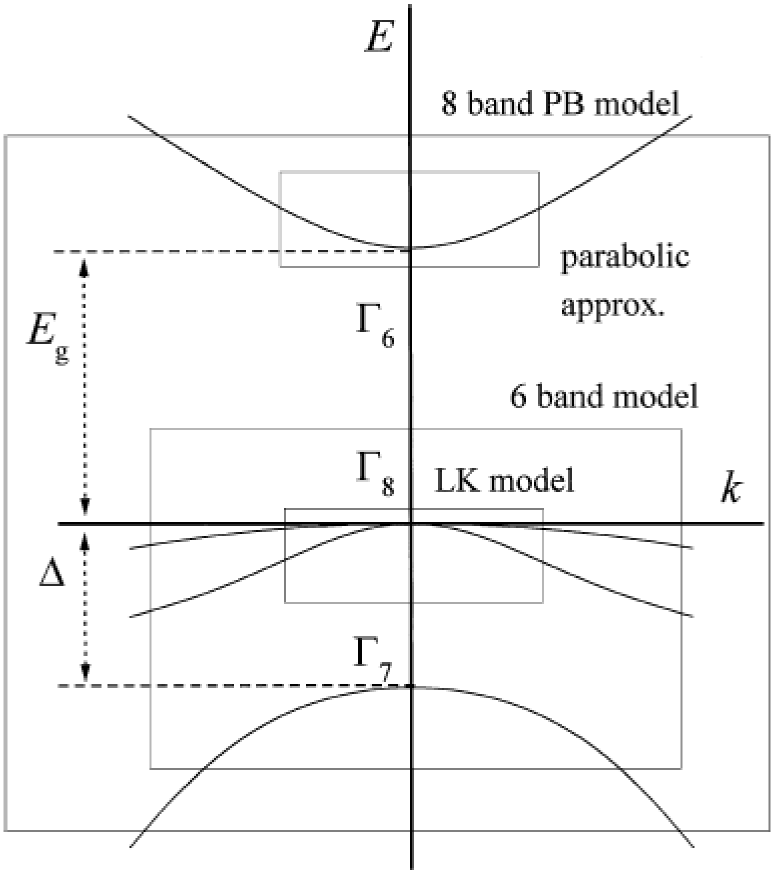

Figure 1.2. The bulk band structure of a direct gap semiconductor with cubic or zinc blend lattice structure and band edge at the Γ-point of the Brillouin Zone. The boxes show the region of applicability of the various models used for the calculation of electron and hole quantum size levels [1.21].

electrons and holes, but in calculating the energies of these levels we must take into account the real band structure found in these semiconductors. In 1990 Ekimov considered the non-parabolic of the conduction band and quantum confinement caused mixing of the six valence bands to obtain electron and hole energy spectra, and one-photon absorption spectra [1.22]. This is called the 6-band model; it doesn't take into account coupling between the conduction and valence bands but rather considers the confined electron and hole levels as independent of each other. This is a good approach for wide-gap semiconductors such as CdSe and CdS, but certainly wouldn't be appropriate for narrow-gap semiconductors.

Due to the complexity of the real band structure, a better description of the bulk bands must be considered in the QDs theory. Therefore the $k \cdot p$ method is usually used, which is a more sophisticated effective mass method. [1.23] Within the $k \cdot p$ method, bulk bands are typically expanded analytically around $k = 0$ point in k-space. Around this point, the wave functions and band energies are then expressed in terms of the periodic functions u_{nk} and their energies E_{nk}. According to the general expressions for u_{nk} and E_{nk} in Eq. (2) and Eq. (3), it is easy to verify that u_{nk} satisfy the equation

$$[H_0 + \frac{1}{m_0}(k \cdot p)]u_{nk} = \lambda_{nk} u_{nk} \tag{1.12}$$

where $\lambda_{nk} = E_{nk} - \frac{k^2}{2m_0}$. u_{n0} and E_{n0} are known values, Eq. (1.12) can be solved within nondegenerate second-order perturbation theory around $k = 0$ with $H^{'} = \frac{k \cdot p}{m_0}$. We can obtain the energies

$$E_{nk} = E_{n0} + \frac{k^2}{2m_0} + \frac{1}{m_0^2} \sum_{m \neq n} \frac{\left| \vec{k} \cdot \vec{p}_{nm} \right|^2}{E_{n0} - E_{m0}} \tag{1.13}$$

and the periodic functions u_{nk}

$$u_{nk} = u_{n0} + \frac{1}{m_0} \sum_{m \neq n} u_{m0} \frac{\vec{k} \cdot \vec{p}_{nm}}{E_{n0} - E_{m0}} \tag{1.14}$$

where $\vec{p}_{nm} = \langle u_{n0} | \vec{p} | u_{m0} \rangle$. From the above discussion, we can see that the dispersion of band n is caused by the coupling with nearby bands. The spin-orbit coupling terms are neglected here. They can be easily added.

As shown in Figure 1.2, the six-fold degenerate valence band can be described by the Luttinger Hamiltonian for bulk diamond like semiconductors. [1.24, 1.25] This 6 × 6 matrix is derived within the degenerate $k \cdot p$ perturbation theory [1.26]. The Hamiltonian is usually simplified further with the spherical approximation [1.27-1.29]. With this method, only the spherical symmetry terms are considered. Cubic symmetry warping terms are neglected or treated as a perturbation. For semiconductor QDs, the Luttinger Hamiltonian (sometimes call the six-band model) is the initial starting point for including the valence-band degeneracies and obtaining the hole eigenstates and their energies.

The Luttinger Hamiltonian is especially useful for describing the hole levels near k equal zero. However, it does not include the coupling between valence and conduction bands, which is very important in narrow bandgap semiconductors. To solve this problem, we can deal with higher order $k \cdot p$ perturbation theory. However, higher order $k \cdot p$ perturbation theory can be very complicated. Then Kane developed another method for bulk semiconductor. [1.30-1.32] In this method, a small subset of bands is considered exactly by explicit diagonalization of Eq. (1.12). (or the equivalent expression with the spin-orbit interaction induced). This subset usually contains the bands of interest (e.g., the valence band and conduction band). Then, the influence of outlying bands is included within the second-order $k \cdot p$ approach. Due to the exact treatment of the important subset, the dispersion of each band is no longer strictly quadratic, as in Eq. (1.13). Therefore, the Kane method can give a better nonparabolic band description. Especially, this method is the necessary to deal with narrow bandgap semiconductors where the coupling between valence band and conduction band cannot be ignored. In semiconductor QDs, due to the strong quantum confinement, even in large bandgap semiconductor QDs, the coupling between valence band and conduction band is significant. So the Kane method is widely used in nanosystems. A Kane-like treatment for semiconductor QDs was first discussed by Sercel and Vahala [1.33, 1.34]. More recently, such a theoretical treatment has been used to successfully describe experimental data on narrow bandgap InAs nanocrystals [1.35] and wide bandgap CdSe QDs. [1.36]

1.2.2 Transition-metal-doped high-quality semiconductor QDs

Doping of transition metals to the II-VI semiconductors can change the electronic and optical properties. This kind of research has been carried out for three decades. The first experimental research of transition-metal doping in ZnSe single crystal was carried out by Grimmeiss and Ovren in 1977. [1.37] In the photo-capacitance investigation, they found that the incorporation of Cu ions into the ZnSe would introduce an energy level at about 0.68 eV above the valence band and they attributed this energy level to Cu. Now this energy level is known as the $4T_1$ energy level of the Cu^{2+} ions. In 1980, Sokolov and Konstantinov further found that the excitons formed in Cu- or Mn-doped ZnSe single crystal were bounded to doping centers; and the bounding energy for the Cu doped ZnSe were around 32 meV. [1.38] One year later, Dean and Herbert published similar results, [1.39] and confirmed that the electrons and holes were bounded to the doping center. They also calculated the bounding energy for various doping centers in ZnSe single crystal based on the electron effective mass. These calculated values well matched their experimental results. In the same year, Godlewski investigated the recombination processes in Cu-doped ZnSe single crystal by monitoring the Cu-green, Cu-red and infrared emission. [1.40] He interpreted his experimental results as direct Donor-Acceptor recombination involving Cu_{Zn} and Cu-X centers combined with indirect recombination via excited states of these centers. Doping introduced energy levels were interpreted for the first time as a contribution by both the doped transition-metal ions and host materials. Now, the electronic energy levels of these transition-metal-doped ZnSe are clearly understood. In summary, when transition metals such as Cu, Mn substitute isoelectronically for Zn atoms and form deep acceptor levels in the bandgap of ZnSe single crystal, the occupation ordering of the *d* and *s* electron shells of these elements is modified so that they can be in two charge states: Cu and Mn with d_{10} electron configuration or Cu and Mn with d_9 electron configuration. Due to mixing of the *d, p* and *s* states, the acceptor levels formed in the bandgap are electronically and optically active.

The transition-metal doping in ZnSe QDs was first conducted by Mikulec et. al. in 2000. [1.41] They reported that the quality of Mn-doped ZnSe crystallites were much lower than the best pure materials. Based on their experimental results, and Counio's [1.42] and Levy's [1.43] research work, Mikulec drew two conclusions: (1) room temperature reactions can easily produce low-quality, transition-metal-doped QDs, and (2) High-quality transition-metal-doped ZnSe QDs can be made by using a high-temperature approach, but Mn^{2+} ions will segregate to the QDs surface (self-purification). In the following years, there were two kinds of conflicting experimental evidence about Mikulec's conclusions. Norris showed that Mikulec's conclusions were not correct under his experiment in 2000. [1.44] He successfully prepared high-quality Mn-doped ZnSe

QDs via a high-temperature reaction. Moreover, he proved that Mn was actually embedded inside the QDs. However, in 2001, Suyver's experimental results confirmed Mikulec's conclusions [1.45]. He synthesized the Cu-doped ZnSe QD under low temperature, but the quality of these QDs is very poor. Then in 2005, Erwin systematically investigated the doping mechanism, [1.46] and found the underlying mechanism that controls doping is the initial adsorption of impurities on the QDs surface during growth. He also found that the doping efficiency is determined by three main factors: surface morphology, QD shape, and surfactants in the growth solution. Based on his work, specific ion doping prediction can be made by calculating adsorption energy and equilibrium shapes for the QDs. He successfully incorporated Mn ions into previously un-dopable CdSe QDs by this prediction. In 2005, for heavy doping in QDs, Pradhan gave another quite different solution when compared to the researches mentioned above. [1.47] His technique is to decouple the doping from nucleation or growth through nucleation-doping and growth-doping. Using this method, he easily prepared CuSe/ZnSe and MnSe/ZnSe QDs of very high quality. Based on the studies referenced above, we can draw the following conclusion: transition-metals doping in ZnSe QDs will face self-purification effect. This problem can be solved by calculating the adsorption energy and equilibrium shape and then choosing certain surfactants to add to the growth solution at the proper time. This problem can also be solved by synthesizing the doping core first, and then synthesizing the host layer. Both strategies can overcome the self-purification effect. However, the first one, which can dope the transition metals at a lower concentration, requires more research work to find the proper surfactants for certain kinds of transition-metal doping, and the second can only be applied under high concentration doping. Synthesizing Cu- and Mn-doped ZnSe QDs with high quality at low-doping level still needs more research efforts.

1.2.3 Multiphoton absorption and related optical nonlinearities in semiconductor QDs

Semiconductor QDs are a very hot research topic for their wide potential applications such as: multiphoton biomedical imaging labels, LEDs and QD lasers. For these applications, the QDs interact with high-power lasers. Under this condition, their nonlinear optical properties especially the nonlinear absorption properties dominate in these applications. The nonlinear optical and ultra-fast dynamical properties of semiconductor QDs have been largely investigated in the last few years. The aim is to identify and develop QDs with large nonlinearities, while satisfying various technological and economical requirements.

Firstly, a short review on nonlinear absorption will be presented here. The first idea about two-photon-absorption was developed by Albert Einstein in his famous Nobel Prize paper of 1905 in Ann Physik. [1.48] It is based on the simultaneous absorption of two photons to produce excitation to a level at the sum of the two photon energies (see Figure 1.3). Then in 1931, Maria Goeppert-Mayer published the quantum mechanical formulas for two-photon absorption in an atomic or a molecular system using second-order quantum perturbation theory which were developed in her doctorate thesis. [1.49] Then after 30 years, the pump lasers were advanced strong enough to reach ~10^{32} photons/cm^2/s to observe the two-photon absorption in experiment, [1.50-1.52] where a photon density during a second of ~10^{32} photons/cm^2 is the necessary pump light intensity for a molecule with ~10^{-16} cross-sections to absorb two photons during the Heisenberg uncertainly principle time of ~10^{-16} sec. The first two-photon absorption induced upconversion fluorescence experiment was conducted by Kaiser and Garrett in 1961. [1.53] Since then, due to the rapid development of intense lasers, not only the two-photon absorption but also multiphoton absorption (n>2) has been studied in a wide variety of materials. Especially in the last two decades, nonlinear absorption in organic molecules, semiconductor bulk materials, semiconductor and metal nano materials has been largely investigated both experimentally and theoretically.

Based on the second-order perturbation theory, the two- and three-photon generation rate of electron-hole pair in a system can be expressed as: [1.54]

$$W^{(2)} = \frac{2\pi}{\hbar}\sum_{v_1,v_0}\left|M_{v_1,v_0}\right|^2 \delta(E_{v_1} - E_{v_0} - 2\hbar\omega),\ M_{v_1,v_0} = \sum_{v_2}\frac{V_{v_1,v_2}V_{v_2,v_0}}{E_{v_2} - E_{v_0} - \hbar\omega - i\hbar\gamma_{v_2}} \tag{1.15}$$

$$W^{(3)} = \frac{2\pi}{\hbar}\sum_{v_1,v_0}\left|M_{v_1,v_0}\right|^2 \delta(E_{v_1} - E_{v_0} - 3\hbar\omega) \tag{1.16}$$

$$M_{v_1,v_0} = \sum_{v_3}\sum_{v_2}\frac{V_{v_1,v_3}V_{v_3,v_2}}{E_{v_3} - E_{v_2} - 2\hbar\omega}\frac{V_{v_2,v_0}}{E_{v_2} - E_{v_0} - \hbar\omega} \tag{1.17}$$

v_0, v_1, *and* v_2 denote sets of quantum numbers for initial, final, and intermediate states of an electron system (see the schematic Figure 1.3). γ_v is the inverse lifetime of the state v.

V is the electron-photon interaction $V_{m,n} = <\psi_m\left|\frac{e}{mc}\vec{A}\cdot\vec{P}\right|\psi_n>$.

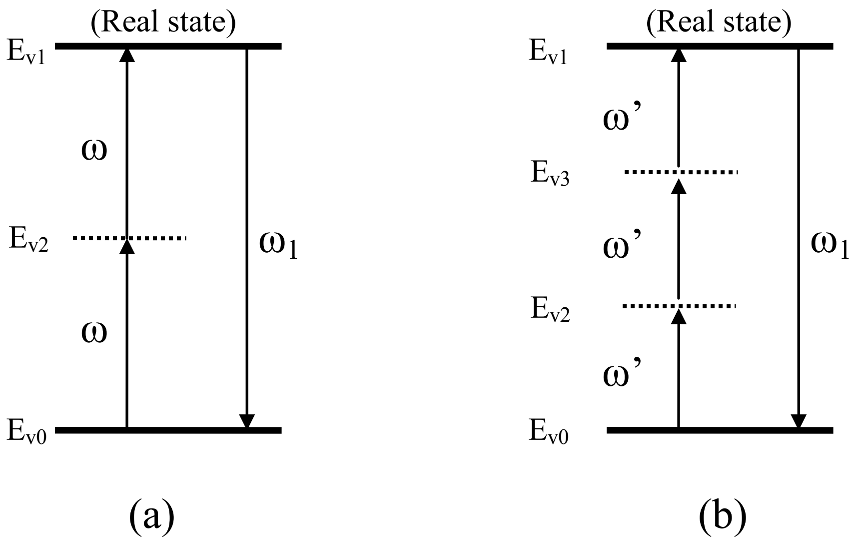

Figure 1.3. Schematic diagrams show two-photon absorption and three-photon absorption in a two-energy-level system.

The above mentioned basic multiphoton absorption theory can be applied to any system. Nonetheless, it is essential to investigate the MPA properties and relation to the MPA theory in light of the unique energy levels and wavefunctions of the new systems. In semiconductor QDs, largely due to the size and shape tunable energy states and wave functions as well as many other advantages, [1.55] multiphoton absorption of semiconductor QDs has been a very hot research topic since 1987. In the following sections, the phenomenological quantifications of multiphoton absorption and associated optical nonlinearities are outlined.

a) Two-photon absorption (2PA) and multiphoton absorption (MPA)

Two-photon absorption (2PA) [1.56, 1.57] is the simultaneous absorption of two photons of identical or different frequencies in order to excite an electron from a lower lying state to an upper lying energy state. The energy difference between these two energy states is the same as the sum of the energies of the two photons, as schematically shown in Figure 1. 3(a). It differs from one-photon absorption in that the strength of absorption depends on the square of the light intensity. The attenuation of the incident light is described by

$$\frac{dI}{dz} = -\beta I^2 \tag{1.18}$$

where I is the light intensity within the sample, z is the position along the beam propagation direction within the sample, β is the 2PA coefficient. The 2PA coefficient, β is a macroscopic parameter characterizing the material. Often, there is interest in the individual molecule's or nanoparticle's 2PA property that is described by the 2PA cross-section σ_2. In the frequency-degenerate case, the relation between β and σ_2 is given by

$$\sigma_2 = \frac{\hbar\omega\beta}{N} \tag{1.19}$$

where N is the number density of the molecules or nanoparticles in the system and $\hbar\omega$ is the energy of photons of the excitation light. The 2PA coefficient is also related to the third-order susceptibility. This coefficient is also related to the third-order nonlinear susceptibility $\chi^{(3)}$ and is given by

$$\beta = \frac{3\pi}{\varepsilon_0 n^2 c\lambda} \mathrm{Im}[\chi^3_{xxxx}(-\omega;\omega,\omega,-\omega)] \tag{1.20}$$

in SI unit, or

$$\beta = \frac{48\pi^3}{n^2 c\lambda} \mathrm{Im}[\chi^3_{xxxx}(-\omega;\omega,\omega,-\omega)] \tag{1.21}$$

in CGS units.

The selection rules for 2PA are totally different from one-photon absorption, which is dependent on the first-order susceptibility. Based on quantum mechanical theory, one photon carries one angular momentum. So an electron in a ground *s*-state only can be excited to a higher *p*-state. That means the total angular momentum of the electron can only be changed +1 or -1 by absorbing one photon. When the electron absorbs two photons simultaneously, the electron will change the total angular momentum by +2, 0, or -2. This allows an *s*-state electron to transition to anther *s*-state or to a *d*-state, as schematically shown in Figure 1.4.

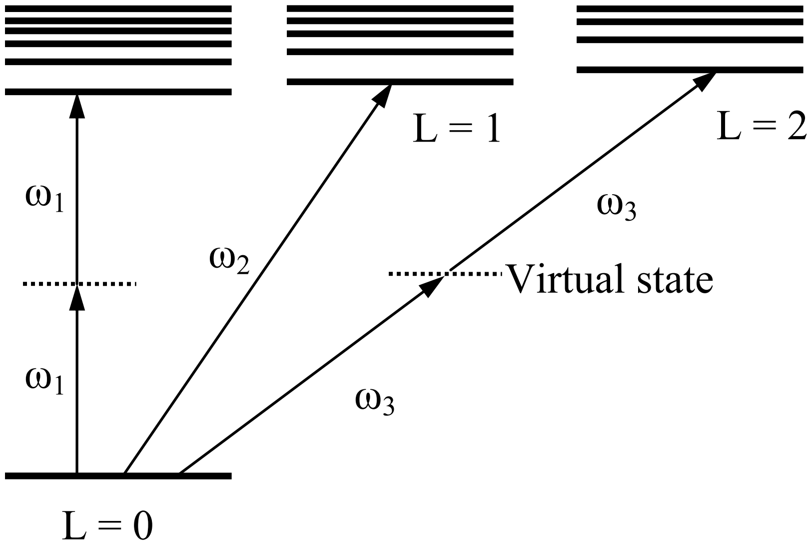

Figure 1.4. Schematical diagram of the total angular momentum conservation between the photons and electrons for one-photon absorption transition and two-photon absorption transition.

Three-photon or multiphoton absorption involves a transition from the lower lying state to an upper lying state by simultaneously absorbing three, as shown in Figure 1.3(b), or more number of photons via multi numbers of virtual states. In this situation, the attenuation of the incident light can be described by [1.56, 1.57]

$$\frac{dI}{dz} = -\alpha_n I^n \tag{1.22}$$

where α_n is the *n*-photon absorption coefficient.

b) Excited state absorption (ESA)

Under high intensity light pumping, due to the significant population of the excited states, the excited state absorption becomes very important. The excited states' electrons can rapidly make a transition to higher excited states before it decays back to the ground state. This phenomenon is obviously of paramount importance if the excited state absorption is resonant with another higher-lying state. [1.58-1.63] As shown in Figure 1.5, if the absorption cross-section of the excited state (σ_{ex}) is smaller than that of the ground state (σ_g), the transmission increases with the pump intensity, as more and more electrons are excited to the excited state N_2. This process is called saturable absorption (SA). Another situation is if the absorption cross-section of the excited state is bigger than that of the ground state, then the system will be less transmissive when excited. This situation gives rise to the opposite result as saturable absorption and is thus called reverse saturable absorption (RSA). RSA gains special interest for the potential application such as optical limiting materials to protect human eyes and sensitive optical equipments. The concept is that this kind of materials can show high linear transmittance at low excitation level but display large nonlinear attenuation at high excitation level.

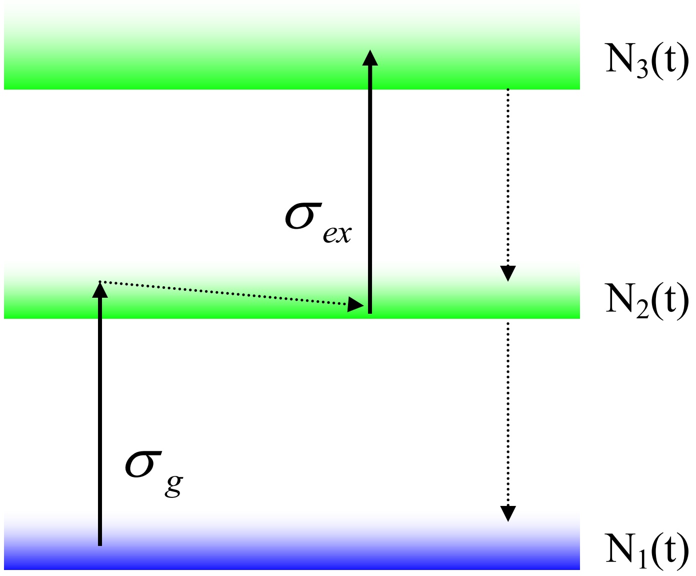

Figure 1.5. Schematic diagram of excited-state absorption (SA or RSA).

The attenuation of the incident light can be described by

$$\frac{dI(z,t)}{dz} = -\sigma_g N_1(z,t)I(z,t) - \sigma_{ex} N_2(t)I(z,t) \tag{23}$$

The sum of N_1, N_2 and N_3 should equal to the total electron density N_0.

The ESA mechanism for organic molecular nonlinear absorption, usually understood by a five-level schema that refers to five distinct electronic states as shown in Figure 1.6.[1.62, 1.63] When an electron is excited from the ground state to the first excited singlet state S_1, the following situations can happen: (1) the electron can relax back to the ground state by radiative or nonradiative transition, with transition rate k_f; (2) the electron can undergo spin flip transition to a lower-lying triplet state T_1, with an intersystem crossing rate k_{isc}; or (3) the electron can transit to a higher-lying singlet state S_2 by absorbing another photon. The electron in the first triplet state T_1 also has two options. It can relax back to the ground state by another spin flip with a transition rate of k_{ph} or transit to a higher-lying triplet state T_2 by absorbing another photon.

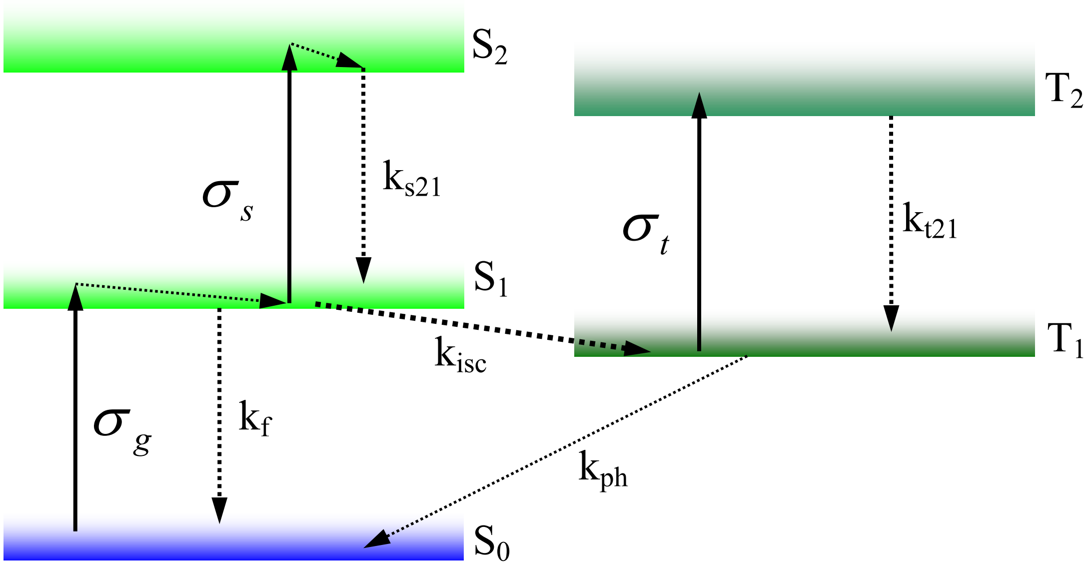

Figure 1.6. Schematic diagram of a five-level model for organic molecular excited-state absorption.

c) Free-carrier absorption (FCA)

In bulk semiconductor, when the electrons are excited to the conduction band, these electrons can contribute to the current flow when an electromagnetic field is applied. They are also called free charge carriers or free carriers. When the electrons are excited to the conduction band, they will undergo ultrafast intraband carrier-carrier and carrier-optical phonon scattering and thermalize to equilibrium state, couple with acoustic phonons and cool down to the bottom of the conduction band. From there it will recombine with a hole in the valence band. Under high intensity light pumping, before these excited carriers recombine, these free carriers have a very high probability to absorb another photon and make a transition within the bands. This process is called free-carrier absorption (FCA). Under relative low light intensity pumping, the attenuation of the incident light due to FCA can be described by [1.63, 1.64]

$$\frac{dI}{dz} = -\alpha_0 I - \sigma_c N_c(I) I \tag{1.24}$$

where σ_c is the free-carrier absorption cross-section and $N_c(I)$ is the pump intensity dependent free-carrier density and is governed by a rate equation

$$\frac{dN_c}{dt} = \frac{\alpha_0 I}{\hbar\omega} - \frac{N_c}{\tau_c} \tag{1.25}$$

where τ_c is the free carrier relaxation time.

Above is the description about one-photon-absorption-generated free carrier absorption. If the pump photon energy is below the bandgap, the MPA-generated free carrier absorption also can be observed in the regime of high laser intensities. After multiphoton excitation, the excited charge carriers will relax to the band edge with few hundreds picoseconds usually. At the same time, the carriers may also make transitions instantaneously to higher energy states by absorbing another incoming photon. In this case, the attenuation of the incident light due to MPA-generated FCA can be described by

$$\frac{dI}{dz} = -[\alpha_0 + \alpha_n I^{n-1} + \sigma_c N_c(I)] I \tag{1.26}$$

where α_n is the n-photon absorption coefficient; $N_c(I)$ is the pump intensity dependent MPA-generated free-carrier density and is governed by a rate equation

$$\frac{dN_c}{dt} = \frac{\alpha_n I^n}{n\hbar\omega} - \frac{N_c}{\tau_c} \tag{1.27}$$

d) MPA-generated Auger recombination

If MPA-generated e-h pair is more than the unity in a system, one e-h pair can be annihilated by exciting another carrier (electron or hole) to a higher energy level. This MPA-generated Auger process is more efficient in nano materials due to the enhanced carrier-carrier interaction in the confined space as compared with bulk materials. Auger process usually occurs on a time scale of several tens picoseconds in direct-gap semiconductor QDs. Therefore, it has little effect on the MAP within one laser pulse (100 fs). However, it greatly affects the MPA-excited fluorescence and leads to a saturation in the overall efficiency. [1.62-1.64]

e) Nonlinear refraction

Nonlinear refraction is the change in the value or spatial distribution of refractive index due to the presence of a high external electromagnetic field. In turn, nonlinear refraction changes the phase of the incident light beam, while nonlinear absorption alters the amplitude of the incident light beam. The pump light intensity dependent refractive index of a material can be written as [1.63]

$$n = n_0 + \Delta n(I) \tag{1.28}$$

where n is the total refractive index, n_0 is the linear refractive index, $\Delta n(I)$ is the pump light intensity dependent nonlinear refractive index. If the sign of $\Delta n(I)$ is positive, it is a self-focusing material. If the sign of $\Delta n(I)$ is negative, it is a self-defocusing material.

f) Nonlinear scattering

Especially for nanomaterials and colloidal QDs, if under high power light excitation, these materials can be heated up to ultrahigh temperature and be evaporated, ionized or gasified to form gas bubbles. The size of these newly generated objects is in the nanometer to micrometer range and expands rapidly. These objects can strongly scatter the incident light away from its original propagation direction and attenuate the transmitted light intensity. These processes are especially useful for optical limiting application. [1.63]

Having introduced the basics of multiphoton absorption and related optical nonlinearities, which lay the foundation for the subject presented in this thesis, we can now provide a review on related research. The first reported experimental work on the study of the nonlinear optical properties of semiconductor QDs is by Wang and Mahler in 1987. [1.65] They used 10 nanosecond laser pulses at 505 nm to study the nonlinear optical absorption of 5-nm-sized CdS QDs doped in glass. The enhancement of two-photon absorption was observed when compared with CdS bulk. They also observed saturable absorption with laser intensities up to 2.5 MW/cm^2. In the following six years, only a few papers focused on multiphoton absorption in semiconductor QDs. Based on single or two wavelength, these studies claimed that two-photon absorption in semiconductor QDs is greatly enhanced when compared with their bulk counterpart. Now this kind of enhancement is known as quantum confinement effect, which was further confirmed by some recent research work. [1.66-1.70] However, in 1994, Banfi et al reported their study of the spectrum of two-photon absorption in CdSe and CdTe QDs. [1.71] In their work, Banfi et al. normalized the 2PA coefficient with bandgap energy and linear refractive index, and concluded that the 2PA in these QDs were quite close to those in the bulk. No enhancement of the two-photon absorption was observed. Some other groups made similar conclusions. For example, in 2003 Y. C. Ker reported an absence of nonlinear absorption in ZnSe QDs embedded in glass matrix. [1.72]

Beyond these experimental observations, in 1996, Fedorov et al. established the frequency-degenerate two-photon absorption theory in CdS QDs under the framework of both effective mass approximation and the well-known four-band model. Their results clearly show that the 2PA cross-section is increased with the pump photon energy. The 2PA cross-section spectra have featured resonance peaks. However, these resonance peaks submerge to the overall trends with the large QD size distribution. [1.73] In 2005, Padilha et al. extended Fedorov's theory to frequency-non-degenerate 2PA in CdTe QDs. Beside the trend that 2PA is increased with pump photon energy, they also obtained that the bigger the QD size, the larger the 2PA cross-section. Their theoretical predictions fit very well their experimental results which were conducted with ~150 fs laser pulses. [1.74] In 2007, Padilha et al. further developed the 2PA theory in semiconductor QDs with the $k \cdot p$ method and took into account the valence band mixing. This work confirmed their previous findings. That's the smaller the QDs size, the smaller 2PA cross-section even taking into account the volume fraction. According to their theoretical and experimental findings, the 2PA cross-sections for CdSe and CdTe QDs within 10 nm diameter are in 10^3 to 10^4 GM range (1 GM = 10^{-50}cm^4/s/photon).[1.75] In 2009, Qu et al. further extended the 2PA theory of QDs by considering both the valence bands mixing and valence-conduction bands mixing based on a spherical eight-band Pidgen and Brown model. This kind of consideration is very important for strong quantum confinement QDs and narrow bandgap QDs. Their theory can give quantitative predictions on the 2PA spectra of CdTe QDs. [1.76]

At the same time, other experimental results also confirmed these theoretical predictions. In 2006, Pu et al. examined the 2PA cross-section of different size CdSe and CdTe QDs at fixed wavelength. They observed a similar trend that the 2PA cross-section is increased with QD size. The empirical relationship is determined to be $\sigma_2 \propto R^n$, where R is the radius of the QD and n is between 3 to 6 for CdSe and CdTe QDs. [1.77] The next year, He et al. measured the size dependent 2PA and three-Photon absorption (3PA) cross-sections of CdSe QDs. They obtained a similar empirical equation that $\sigma_2 \propto R^4$ and $\sigma_3 \propto R^{3.3}$. [1.78]

Besides the size dependence, the nanoparticle shape-dependent 2PA was also experimentally and theoretically investigated recently. In 2009, Li et al. reported the greatly enhanced 2PA in CdS nanorods (10^5 GM). [1.79] In the same year, Feng et al. theoretically calculated the shape-dependent 2PA based on a four-band model under effective mass approximation. They conclude that 2PA is strongly dependent on the nanoparticle’s shape which can cause the splitting of degenerate energy levels. Based on their calculations, one can conclude that the nanocuboids and nanocubes have larger 2PA cross-sections than nanocylinders and nanospheres of similar sizes. [1.80]

In summary, the 2PA of semiconductor QDs is widely investigated both experimentally and theoretically. The established relationships between 2PA cross-section and QDs size, QD shape, excitation laser wavelength, and excitation laser pulse duration can be summarized below:

1) The greater the spherical QD size, the larger of the 2PA cross-section. This trend is mainly caused by the QD's density of states which is increased with QD size.

2) The 2PA cross-section is strongly shape dependent. Based on the second-order perturbation theory, the 2PA and MPA are determined by the energy levels and corresponding wave-functions. The difference in shape can cause subtle changes in the energy levels and wave-functions which change the 2PA and MPA cross-sections. For similar lateral sizes nanocuboids and nanocubes exhibit larger 2PA cross-sections than nanocylinders and nanospheres.

3) The shorter the pump wavelength, the larger the 2PA cross-section. This is also mainly caused by the difference in the density of states. The higher the energy levels, the smaller the energy level separations.

4) With longer excitation laser pulse duration, the larger nonlinear absorption can be observed. This is mainly caused by the thermal effect and excited state absorption.

Though 3PA has many advantages for the potential applications when compared with one-photon absorption (1PA) and 2PA, the research on 3PA in semiconductor QDs is still very limited. The first QD's 3PA experiment was conducted by Chon et. al with ~100 fs laser puses in 2004. Through the upconversion PL experiment, the 3PA cross-section of CdS QDs was determined to be around 10^{-79} $cm^6s^2photon^{-2}$, which is about 3 or 4 orders of magnitude bigger than common UV fluorescent dyes. [1.81] The second QD's 3PA experiment was conducted on ZnS by He et al. with 120 fs laser pulses in 2006. The 3PA cross-section was measured to be ~2.7×10^{-78} $cm^6s^2photon^{-2}$. [1.82] In 2007, the 3PA cross-sections of ZnSe and ZnSe/ZnS QDs were measured to be on the order of 10^{-75} $cm^6s^2photon^{-2}$ with 35 picosecond laser pulses. From the experiments, it could be also concluded by Lad et al. that the 3PA cross-section was inversely proportional to the QD's radius. This is the opposite size dependence compared with widely accepted 2PA size dependence in QDs. [1.83] Their obtained σ_3 values are also near 4 orders of magnitude larger than previous reports. If we calculate the excited electron-hole pairs per QD and per laser pulse under their conditions, the calculated value is much larger than one. It implies that the previously discussed excited state absorption must be considered in their experiments. Their 3PA cross-sections are overestimated. In the same year 2007, He et al. measured the size dependent 3PA cross-section of CdSe QDs with 160 fs laser pulses. According to their results, the 3PA cross-section of CdSe QDs is on the order of ~10^{-78} $cm^6s^2photon^{-2}$, which is comparable with the reported values on CdS and ZnS QDs, but much smaller than the reported value for ZnSe and ZnSe/ZnS QDs by Lad et al. Similar to the 2PA size dependence, He et al. also obtained a clear trend that the 3PA cross-section increases with the QDs size. The empirical relation is established as $\sigma_3 \propto R^{3.3}$. [1.78] In 2008, with picosecond laser pulses, extremely larger 3PA cross-section was observed in CdS QDs. [1.84] It is believed that these authors have made the same kind of mistakes as in Ref. [76] and overestimated the 3PA cross-section.

In summary, the research on 3PA of semiconductor QDs is limited. Though some of the general characteristics are expected to be the same as 2PA, more experimental and theoretical work are still required to confirm these characteristics.

Table 1.1. QDs, QD diameters, lasers used and measured 3PA cross-sections.

QDs	Diameter (nm)	Laser source	3PA cross-section σ_3 ($cm^6s^2photon^{-2}$)	Publication year
CdS	NA.	100 fs, 900-1000 nm	$\sim 10^{-79}$	2004 [1.81]
ZnS	2.5	120 fs, 780 nm	$\sim 2.7 \times 10^{-78}$	2006 [1.82]
ZnSe **ZnSe/ZnS**	3.5, 4.5	35 ps, 1064 nm	$\sim 10^{-75}$	2007 [1.83]
CdSe	2.0 – 3.9	160 fs, 1300 nm	$\sim 10^{-78}$	2007 [1.78]
SC-CdS	2.5	25 ps, 1064 nm	$\sim 8 \times 10^{-73}$	2008 [1.84]
ZnS	1.3	120 fs, 620-720 nm	$\sim 10^{-78}$	2008 [1.85]

Overall, semiconductor QDs have many advantages, such as high PL quantum yield, good stability, easy chemical processability, large stokes shift and size tunable optoelectronic properties. Due to these advantages, especially that for the size tunable optoelectronic properties, semiconductor QDs have received attention for both basic physics and potential applications over the last two decades. For applications in optical switching (for optical communications), three-dimensional optical data storage, three dimensional confocal imaging for biological specimens, optical limiting (for protection of human eyes and sensitive optoelectronic equipment), and photodynamic therapy, the 2PA and MPA in semiconductor QDs have been investigated to some extent. The 2PA and MPA are determined by the energy levels and wavefunctions. By changing the QD's size, QD's shape and excitations sources, we can tailor the 2PA and MPA cross-sections to some extent. However, these cross-sections are still relatively small in the quantum confinement range (where the QD radius is smaller than the exciton Bohr radius). So we may ask the following questions: can we increase the 2PA and MPA cross-sections through some other methods? Another point is the 2PA and MPA properties in semiconductor QDs are still not fully understood. For example, previous research work was conducted in either the 2PA-dominated regime ($E_g/2<\hbar\omega<E_g$) or the 3PA-dominated regime ($E_g/3<\hbar\omega<E_g/2$). The situation of the excitation photon energy coming near to the edge ($\hbar\omega\sim E_g/2$) has never been previously investigated. This kind of uncertainty will prevent one from clearly understanding the entire MPA spectrum as well as unambiguously determining the 2PA and MPA cross-sections. Recently, transition-metal-doped semiconductor QDs show lots of improved properties if compared with traditional QDs. [1.86, 1.87] For example, transition-metal doping can suppress undesirable QD's surface reactions, enhance the PL quantum yields, enlarge Stokes shift, and endow magneto-optical properties. The transition-metal doping is expected to provide some new energy levels inside the QDs, alter and rearrange the QD's original energy levels. As a result, the 2PA and MPA properties of semiconductor QDs are modified by transition-metal doping. However, the effects of such modification on the 2PA/MPA properties are still unclear. In this thesis, it is our aim to provide answers to these un-resolved issues.

1.3 Objectives and scope

The purpose of this research was to study the nonlinear optical and exciton dynamical properties of ZnSe/ZnS and transition-metal-doped ZnSe/ZnS semiconductor QDs with experimental methods. More specifically, the objectives are:

i) To study the three-photon absorption in ZnSe/ZnS and transition-metal-doped ZnSe/ZnS QDs by transmittance open-aperture Z-scan technique. Here the transition metals involved are copper and manganese which give higher quantum efficiency when compared with others. The Z-scan method [1.88] was used because it is not only a very simple method, but also a very accurate technique for characterizing the quantities of the nonlinear absorption coefficient as well as the nonlinear refractive index of a material. The wavelengths were limited to the range between 850 nm and 1064 nm. In this range, the photon energy is $\frac{E_g}{3} < \hbar w < \frac{E_g}{2}$.

ii) To study the intensity-dependent interplay of two- and three-photon absorption in water-soluble manganese-doped ZnSe/ZnS QDs. Here both multiphoton excited PL and Z-scan experiments are conducted with 800 nm, femtosecond laser pulses. Z-scan is effective at high laser intensity where the nonlinear absorption drop is greater than one percent. Multiphoton excited PL technique is more sensitive than Z-scan in determining the nonlinear absorption at low excitation intensity. By combining these two techniques, the interplay of two- and three-photon absorption can be studied over a wide laser intensity range from 0.001 GW/cm^2 to 1000 GW/cm^2.

iii) To study the exciton formation and recombination processes in ZnSe/ZnS and Cu- and Mn-doped ZnSe/ZnS QDs by femtosecond time-resolved pump-probe ($\leq$ 1ns) measurement ($\leq$ 1ms) techniques. The pump-probe measurement that consists of two laser beams of a weak probe and a strong pump, respectively, is a well-known technique used to observe the photon dynamics in a nonlinear optical material. Here the pump beam is 400 nm and the probe beam is white light which is generated by focusing 800 nm laser into a sapphire template.

The above-said three studies provide relevant information for the applications of transition-metal-doped ZnSe/ZnS QDs as multiphoton biomedical imaging labels, light emitting diodes (LEDs), upconversion lasers, and solar cells. The results of the nonlinear optical studies will enhance our understanding of the influence of transition-metal doping on the nonlinear optical properties of semiconductor QDs. The results of exciton dynamics study will lead to a better understanding of how the quantum confinement changes the spin-forbidden transitions in QDs.

The experiment setups and principles of Z-scan, pump-probe, and multiphoton-excited PL will be detailed in the next chapter. The above-mentioned three experimental studies and findings will be presented in Chapters 3, 4, 5 and 6, respectively. A final conclusion and future work will be summarized in Chapter 7.

References:

[1.1] X. Michalet, F. F. Pinaud, L. A. Bentolila, J. M. Tsay, S. Doose, J. J. Li, G. Sundaresan, A. M. Wu, S. S. Gambhir, and S. Weiss, "Quantum dots for live cells, in vivo imaging, and diagnostics," *Science* **307**, 538 (2005).

[1.2] A. P. Alivisatos, "Semiconductor clusters, nanocrystals, and quantum dots," *Science* **271**, 933 (1996).

[1.3] D. J. Norris and M. G. Bawendi, "Measurement and assignment of the size-dependent optical spectrum in CdSe quantum dots," *Phys. Rev. B* **53**, 16338 (1996).

[1.4] A. M. Derfus, W. C. W. Chan, and S. N. Bhatia, "Probing the cytotoxicity of semiconductor quantum dots," *Nano Lett.* **4**, 11 (2004).

[1.5] N. Pradhan, D. M. Bataglia, Y. Liu, and X. Peng, "Efficient, stable, small, and water-soluble doped ZnSe nanocrystal emitters as non-cadmium biomedical labels," *Nano Lett* **7**, 312 (2007).

[1.6] G. Banfi, V. Degiorgio, and D. Ricard, "Nonlinear optical properties of semiconductor nanocrystals," *Adv. Phys.* **47**, 447 (1998).

[1.7] R. K. Jain and R. C. Lind, "Degenerate 4-wave mixing in semiconductor-doped glasses," *J. Opt. Soc. Am*. **73**, 647 (1983).

[1.8] R. Rossetti, S. Nakahara, and L. E. Brus, "Quantum size effects in the redox potentials, resonance raman-spectra, and electronic-spectra of cds crystallites in aqueous-solution," *J. Chem. Phys.* **79**, 1086 (1983).

[1.9] M. A. Reed, R. T. Bate, K. Bradshaw, W. M. Duncan, W. R. Frensley, J. W. Lee, and H. D. Shih, "Spatial quantization in gaas-algaas multiple quantum dots," *J. Vac. Sci. Technol.* **4B**, 358 (1986).

[1.10] N. W. Ashcroft and N. D. Mermin, Solid State Physics (W. B. Saunders Co., Orlando, FL., USA, 1976).

[1.11] H. Haug and S. Koch, Quantum Theory of the Optical and Electronic Properties of Semiconductors (World Scientific Publishing, Singapore, 2004).

[1.12] V. I. Klimov, "Mechanisms for photogeneration and recombination of multiexcitons in semiconductor nanocrystals: implications for lasing and solar energy conversion," *J. Phys. Chem. B* **110**, 16827 (2006).

[1.13] V. I. Klimov and D. W. McBranch, "Femtosecond 1P-to-1S electron relaxation in strongly confined semiconductor nanocrystals," *Phys. Rev. Lett.* **80**, 4028 (1998).

[1.14] Al. L. Efros and A. L. Efros, "Interband absorption of light in a semiconductor sphere," *Sov. Phys. Semicond.* **16**, 772 (1982).

[1.15] A. I. Ekimov and A. A. Onushchenko, "Quantum size effect in the optical-spectra of semiconductor micro-crystals," *JETP Lett.* **34**, 345, (1982).

[1.16] S. V. Gaponenko, Optical Properties of Semiconductor Nanocrystals. Cambridge, UK, Cambridge Univ. Press (1998).

[1.17] U. Woggon, Optical Properties of Semiconductor Quantum Dots, Springer, Berlin (1997).

[1.18] L. E. Brus, "A simple-model for the ionization-potential, electron-affinity, and aqueous redox potentials of small semiconductor crystallites," *J. Chem. Phys*. **79**, 5566 (1983).

[1.19] L. E. Brus, "Electron-electron and electron-hole interactions in small semiconductor crystallites - the size dependence of the lowest excited electronic state," *J. Chem. Phys*. **80**, 4403 (1984).

[1.20] A. I. Ekimov, F. Hache, M. C. Schanne-Klein, D. Richard, C. Flytzanis, I. A. Kudryavtsev, T. V. Yazeva, A. V. Rodina, and Al. L. Efros, "Absorption and intensity-dependent photoluminescence measurements on cdse quantum dots - assignment of the 1st electronic-transitions," *J. Opt. Soc. Am. B* **10**, 100 (1993).

[1.21] Al. L. Efros and M. Rosen, "The electronic structure of semiconductor nanocrystals," *Annu. Rev. Mater. Sci.* **30**, 475 (2000).

[1.22] D. I. Chepic, A. L. Efros, A. I. Ekimov, M.G. Ivanov, V. A. Kharchenko, I. A. Kudriavtsev, and T. V. Yazeva, "Auger ionization of semiconductor quantum drops in a glass matrix," *J. Luminescence* **47**, 113 (1990).

[1.23] C. Kittel, Quantum Theory of Solids. New York: Wiley (1987).

[1.24] J. M. Luttinger, "Quantum theory of cyclotron resonance in semiconductors - general theory," *Phys. Rev. B* **102**, 1030 (1956).

[1.25] J. M. Luttinger and W. Kohn, "Motion of electrons and holes in perturbed periodic fields," *Phys. Rev.* **97**, 869 (1955).

[1.26] G. L. Bir and G. E. Pikus, Symmetry and Strain-Induced Effects in Semiconductors. New York: Wiley (1974).

[1.27] N. O. Lipari and A. Baldereschi, "Angular momentum theory and localized stats in solids - investigation of shallow acceptor states in semiconductors," *Phys. Rev. Lett.* **42**, 1660 (1970).

[1.28] B. L. Ge'lmont and M. I. D'yakonov, "Acceptor levels in diamond-type semiconductors," *Sov. Phys. Semicond.* **5**, 1905 (1972).

[1.29] A. Baldereschi and N. O. Lipari, "Spherical model of shallow acceptor states in semiconductors," *Phys. Rev. B* **8**, 2697 (1973).

[1.30] E. O. Kane, "Band structure of indium antimonide," *J. Phys. Chem. Solids* **1**, 249 (1957).

[1.31] C. R. Pidgeon and R. N. Brown, "Interband magneto-absorption and faraday rotation in insb," *Phys. Rev.* **146**, 575 (1966).

[1.32] E. O. Kane, In Narrow Band Semiconductors, Physics and Aplications, Lecture Notes in Physics; Zawadski W. ed. Berlin: Springer-Verlag, Vol. **133** (1980).

[1.33] K. J. Vahala and P. C. Sercel, "Application of a total-angular-momentum basis to quantum-dot band-structure," *Phys. Rev. Lett.* **65**, 239 (1990).

[1.34] P. C Sercel and K. J. Vahala, "Analytical formalism for determining quantum-wire and quantum-dot band-structure in the multiband envelope-function approximation," *Phys. Rev. B* **42**, 3690 (1990).

[1.35] U. Banin, C. J. Lee, A. A. Guzelian, A. V. Kadavanich, A. P. Alivisatos, W. Jaskolski, G. W. Bryant, Al. L. Efros, and M. Rosen, "Size-dependent electronic level structure of InAs nanocrystal quantum dots: test of multiband effective mass theory," *J. Chem. Phys.* **109**, 2306 (1998).

[1.36] Al. L. Efros and M. Rosen, "Quantum size level structure of narrow-gap semiconductor nanocrystals: effect of band coupling," *Phys. Rev. B* **58**, 7120 (1998).

[1.37] H. G. Grimmeriss, C. Ovren, W. Ludwig, and R. Mach, "Identification of deep centers in ZnSe," *J. Appl. Phys.* **48**, 5122 (1977).

[1.38] V. I. Sokolov and V. L. Konstantinov, "Discovery of bound exciton in ZnSe-Cu," *Solid State Commun.* **33**, 471 (1980).

[1.39] P. J. Dean, D. C. Herbert, C. J. Werkhoven, B. J. Fitzpatrick, and R. N. Bhargava, "Donor bound-exciton excited-states in zinc selenide," *Phys. Rev. B* **23**, 4888 (1981).

[1.40] M. Godlewski, W. E. Lamb, and B. C. Cavenett, "Odmr investigations of recombination processes in ZnSe-Cu," *Solid State Commun.* **39**, 595 (1981).

[1.41] F. V. Mikulec, M. Kuno, M. Bennati, D. A. Hall, R. G. Griffin, and M. G. Bawendi, "Self-assembly of CdSe-ZnS quantum dot bioconjugates using an engineered recombinant protein," *J. Am. Chem. Soc.* **122**, 2532 (2000).

[1.42] G. Counio, S. Esnouf, T. Gacoin, and J. P. Boilot, "CdS:Mn nanocrystals in transparent xerogel matrices: synthesis and luminescence properties," *J. Phys. Chem*. **100**, 20021 (1996).

[1.43] L. Levy, N. Feltin, D. Ingert, and M. P. Pileni, "Three dimensionally diluted magnetic semiconductor clusters $Cd_{1-y}Mn_yS$ with a range of sizes and compositions: dependence of spectroscopic properties on the synthesis mode," *J. Phys. Chem. B* **101**, 9153 (1997).

[1.44] D. J. Norris, Nan Yao, F. T. Charnock, and T. A. Kennedy, "High-quality manganese-doped ZnSe nanocrystals," *Nano Lett*. **1**, 3 (2001).

[1.45] J. F. Suyver, T. Van der Beek, S. F. Wuister, J. J. Kelly, and A. Meijerink, "Luminescence of nanocrystalline ZnSe : Cu," *Appl. Phys. Let.* **79**, 4222 (2001).

[1.46] S. C. Erwin, L. Zu, M. I. Haftel, A. L. Efros, T. A. Kennedy, and D. J. Norris, “Doping semiconductor nanocrystals,” *Nature* **436**, 91 (2005).

[1.47] N. Pradhan, D. Goorskey, J. Thessing, and X. Peng, “An alternative of CdSe nanocrystal emitters: pure and tunable impurity emissions in ZnSe nanocrystals,” *J. Am. Chem. Soc,* **127**, 17586 (2005).

[1.48] Einstein, A. Creation and Conversion of Light. Ann. Physik **17**, 132 (1905).

[1.49] Goeppert-Mayer, M. Elementary processes with two quantum jumps. Ann. Physik **9**, 273 (1931).

[1.50] P. A. Franken, G. Weinreich, C. W. Peters, and A. E. Hill, “Generation of optical harmonics,” *Phys. Rev. Lett.* **7**, 118 (1961).

[1.51] E. J. Woodbury and W. K. Ng, “Ruby laser operation in near ir,” *Proc. IRE.* **50**, 2347 (1962).

[1.52] T. H. Maiman, “Stimulated optical radiation in ruby,” *Nature* **187**, 493 (1960).

[1.53] W. Kaiser and C. G. B. Garrett, “2-photon excitation in CaF_2 - Eu^{2+},” *Phys. Rev. Lett.* **7**, 229 (1961).

[1.54] D. C. Hutchings and E. W. Van Stryland, “Nondegenerate 2-photon absorption in zinc blende semiconductors,” *J. Opt. Soc. Am. B* **9**, 2065 (1992).

[1.55] A. P. Alivisatos, “Semiconductor clusters, nanocrystals, and quantum dots,” *Science* **271**, 933 (1996).

[1.56] Y. R. Shen, The Principles of Nonlinear Optics, John Wiley, New York (1984).

[1.57] R. W. Boyd, Nonlinear Optics, Academic Press, New York (1992).

[1.58] F. P. Schafer, Principles of dye laser operation, Dye Lasers (F. P. Schafer, ed), Springer-Verlag, New York 1977.

[1.59] C. R. Giuliano and L. D. Hess, "Nonlinear absorption of light: optical saturation of electronic transitions in organic molecules with high intensity laser radiation," *IEEE J. Quantum Electr. QE* **3**, 358 (1967).

[1.60] L. Huff and L. G. Deshazer, "Nonlinear absorption behavior of indanthrone dyes: comparison of optical saturation and photochemical processes," *J. Appl. Phys*. **40**, 4336 (1969).

[1.61] L. Huff and L. G. DeShazer, "Saturation of optical transitions in organic compounds by laser flux," *J. Opt. Soc. Am*. **60**, 157 (1970).

[1.62] G. S. He and S. H. Liu, Physics of Nonlinear Optics, World Scientific Publishing Co. Pvt. Ltd., Singapore (1999).

[1.63] R. L. Sutherland, Handbook of Nonlinear Optics, Marcel Dekker Inc., New York (1996).

[1.64] D. G. McLean, R. L. Sutherland, M. C. Brant, D. M. Brandelik, P. A. Fleitz, and T. Pottenger, "Nonlinear absorption study of a C_{60}-toluene solution," *Opt. Lett*. **18**, 858 (1993).

[1.65] Y. Wang and W. Mahler, "Degenerate 4-wave-mixing of CdS/polymer composite," *Opt. Commun*. **61**, 233 (1987).

[1.66] D. L. Young, T. J. Coutts V. I. Kaydanov, A. S. Gilmore, and W. P. Mulligan, "Direct measurement of density-of-states effective mass and scattering parameter in transparent conducting oxides using second-order transport phenomena," *J. Vac. Sci. Technol. A* 2978 (2000).

[1.67] X. Wang, Y. Du, S. Ding, Q. Wang, G. Xiang, M. Xie, X. Chen, and D. Peng, "Preparation and third-order optical nonlinearity of self-assembled chitosan/CdSe-ZnS core-shell quantum dots multilayer films," *J. Phys. Chem. B* **110**, 1566 (2006).

[1.68] A. D. Lad, P. P. Kiran, G. R. Kumar, and S. Mahamuni, "Three-photon absorption in ZnSe and ZnSe/ZnS quantum dots," *Appl. Phys. Lett.* **79**, 4222 (2007).

[1.69] V. V. Nikesh, A. Dharmadhikari, H. Ono, S. Nozaki, G. R. Kumar, and S. Mahamuni, "Optical nonlinearity of monodispersed, capped ZnS quantum particles," *Appl. Phys. Lett*. **84**, 4602 (2004).

[1.70] I. Gerdova and A. Haache, "Third-order non-linear spectroscopy of CdSe and CdSe/ZnS core shell quantum dots," *Optics Commun.* **26**, 205 (2005).

[1.71] G. P. Banfi, V. Degiorgio, H. M. Tan, and A. Tomaselli, "Two-photon absorption in semiconductor nanocrystals," *Phys. Rev. B* **50**, 5699 (1994).

[1.72] Y. C. Ker, J. H. Lin, and W. F. Hsieh, "Saturation of large nonresonant third and fifth order optical nonlinearities from ZnSe quantum dots in glass-matrix thin films," *Jpn. J. Appl. Phys.* **42**, 1258 (2003).

[1.73] A. V. Fedorov, A. V. Baranov, and K. Inoue, "Two-photon transitions in systems with semiconductor quantum dots," *Phys. Rev. B* **54**, 8627 (1996).

[1.74] L. A. Padilha, J. Fu, D. J. Hagan, and E. W. V. Stryland, "Two-photon absorption in CdTe quantum dots," *Opt. Express* **13**, 6460 (2005).

[1.75] L. A. Padilha, J. Fu, D. H. Hagan, E. W. Van Stryland, C. L. Cesar, L. C. Barbosa, C. H. B. Cruz, D. Buso, and A. Martucci, "Frequency degenerate and nondegenerate two-photon absorption spectra of semiconductor quantum dots," *Phys. Rev. B* **75**, 075325 (2007).

[1.76] Y. L. Qu and W. Ji, "Frequency degenerate and nondegenerate two-photon absorption spectra of semiconductor quantum dots," *J. Opt. Soc. Am. B* **26**, 1897 (2009).

[1.77] S. C. Pu, M. J. Yang, C. C. Hsu, C. W. Lai, C. C. Hsieh, S. H. Lin, Y. M. Cheng, and P. T. Chou, "The empirical correlation between size and two-photon absorption cross section of CdSe and CdTe quantum dots," *Small* **2**, 1308 (2006).

[1.78] G. S. He, K. T. Yong, Q. D. Zheng, Y. Sahoo, A. Baev, A. I. Ryasnyanskiy, and P. N. Prasad, "Multi-photon excitation properties of CdSe quantum dots solutions and optical limiting behavior in infrared range," *Opt. Express* **15**, 12818 (2007).

[1.79] X. P. Li, J. Embden, W. M. Chon, and M. Gu, "Enhanced two-photon absorption of CdS nanocrystal rods," *Appl. Phys. Lett.* **94**, 103117 (2009).

[1.80] X. B. Feng and W. Ji, "Shape-dependent two-photon absorption in semiconductor nanocrystals," *Opt. Express* **17**, 13140 (2009).

[1.81] J. W. M. Chon, M. Gu, C. Bullen, and P. Mulvaney, "Three-photon excited band edge and trap emission of CdS semiconductor nanocrystals," *Appl. Phys. Lett.* **84**, 4472 (2004).

[1.82] J. He, W. Ji, J. Mi, Y. G. Zheng, and J. Y. Ying, "Three-photon absorption in water-soluble ZnS nanocrystals," *Appl. Phys. Lett.* **88**, 181114 (2006).

[1.83] A. D. Lad, P. P. Kiran, G. R. Kumar, and S. Mahamuni, "Three-photon absorption in ZnSe and ZnSe/ZnS quantum dots," *Appl. Phys. Lett.* **90**, 133113 (2007).

[1.84] Y. Gao, A. Tonizzo, A. Walser, M. Potasek, and R. Dorsinville, "Enhanced optical nonlinearity of surfactant-capped CdS quantum dots embedded in an optically transparent polystyrene thin film," *Appl. Phys. Lett.* **92**, 033106 (2008).

[1.85] J. He, G. D. Scholes, Y. L. Ang, W. Ji, C. W. J. Beh, and W. S. Chin, "Direct observation of three-photon resonance in water-soluble ZnS quantum dots," *Appl. Phys. Lett.* **92**, 131114 (2008).

[1.86] S. T. Ochsenbein, Y. Feng, K. M. Whitaker, E. Badaeva, W. K. Liu, X. Li, and D. R. Gamelin, "Charge-controlled magnetism in colloidal doped semiconductor nanocrystals," *Nature Nanotech.* **4**, 681 (2009).

[1.87] D. A. Bussian, S. A. Crooker, M. Yin, M. Brynda, A. L. Efros, and V. I. Klimov, "Tunable magnetic exchange interactions in manganese-doped inverted core-shell ZnSe-CdSe nanocrystals," *Nature Mater.* **8**, 35 (2009).

[1.88] M. Sheik-Bahae, A. A. Said, T. H. Wei, D. J. Hagan, and E. W. V. Styland, "Sensitive measurement of optical nonlinearities using a single beam," *IEEE J. Quantum Electron.* **26**, 760 (1990).

Chapter 2

Experimental methodologies

A wide range of experimental techniques have been utilized for the investigations reported in this thesis. To investigate the linear and nonlinear optical properties of semiconductor QDs, we have performed the experiments of ultraviolet-visible-infrared absorption spectroscopy, photoluminescence (PL) spectroscopy, time-resolved PL spectroscopy, energy-dependent nonlinear transmission (or Z-scan) measurement, upconversion PL and time-resolved transient absorption (or pump-probe) measurements. To establish the relationships between the optical properties and semiconductor QD size, shape and structure, we have conducted the experiments by using scanning electron microscope (SEM), transmission electron microscope (TEM) and X-ray diffraction (XRD).

Among the above experimental methodologies, some of them are the standard ones, and their operational principles and details are well-explained in many textbooks. Thereby, they will not be repeated here. In this chapter, we will concentrate on the operational principles and details of the Z-scan technique, pump-probe technique, upconversion PL and time-resolved PL measurements in the following sections. These techniques were designed and set up in our laboratories. Since all these techniques involve lasers, we will begin to detail the lasers employed.

2.1 Lasers

In the above-mentioned nonlinear optics measurements and ultrafast spectroscopy, we used 1 kHz-repetition-rate, 120-fs (FWHM), and 780-nm-wavelength laser pulses provided by a Ti:Sapphire regenerative amplifier (Quantronix, Titan). The amplifier was seeded by an erbium-doped fiber laser (Quantronix, IMRA). For other laser wavelengths, we used an optical parametric amplifier (TOPAS). Generally, a low-repetition-rate Ti: Sapphire amplifier and an optical parametric amplifier were combined to provide large fluence and broad wavelength tenability.

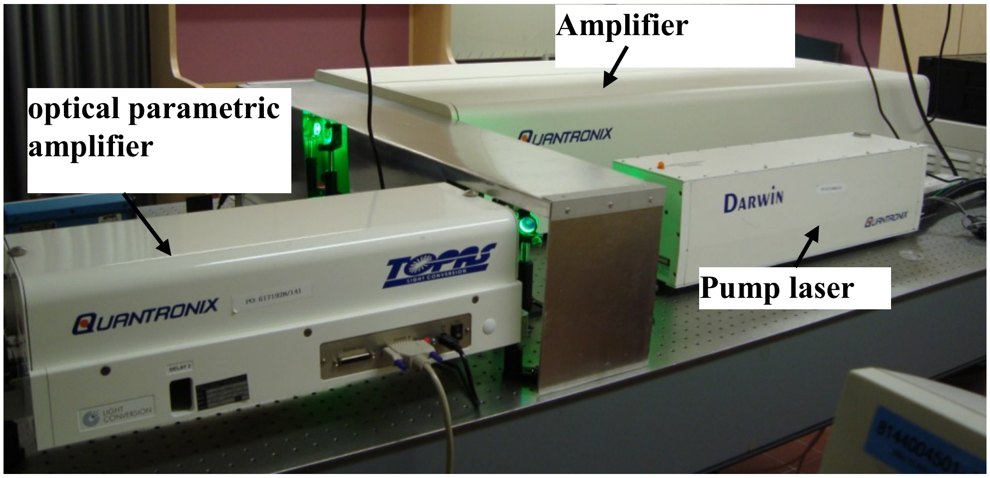

Figure 2.1. Photograph of the Quantronix laser system.

In some of the wavelength dependent Z-scan measurements, the laser pulses were provided by a Coherent Legend (seeded by Mira) pumped TOPAS-C operation at 1 kHz repetition rate. In some of the upconversion PL experiments, the excitation source was a femtosecond Ti:Sapphire oscillator (Spectra Physics, Tsunami, pulse duration = 40 fs, repetition rate = 76 MHz and center wavelength = 800 nm).

2.1.1 Chirped pulse amplifier

Nowadays, most of the amplified femtosecond laser pulses were generated in a Ti: Sapphire regenerative amplifier system, which is based on the chirped pulse amplification (CPA) technique. [1] If femtosecond laser pulses are directly amplified, the short pulse duration results in very high peak power intensity. Such high peak intensity would easily damage the gain materials or reach the saturation of the gain which prevents further pulse amplification. The CPA technique first stretches the femtosecond pulses by a large factor (~10^5) and then amplifies the long pulses safely. At last, these amplified long pulses are compressed to the original pulse duration with a pulse compressor, which can also compensate the group velocity dispersion introduced by the previous step.

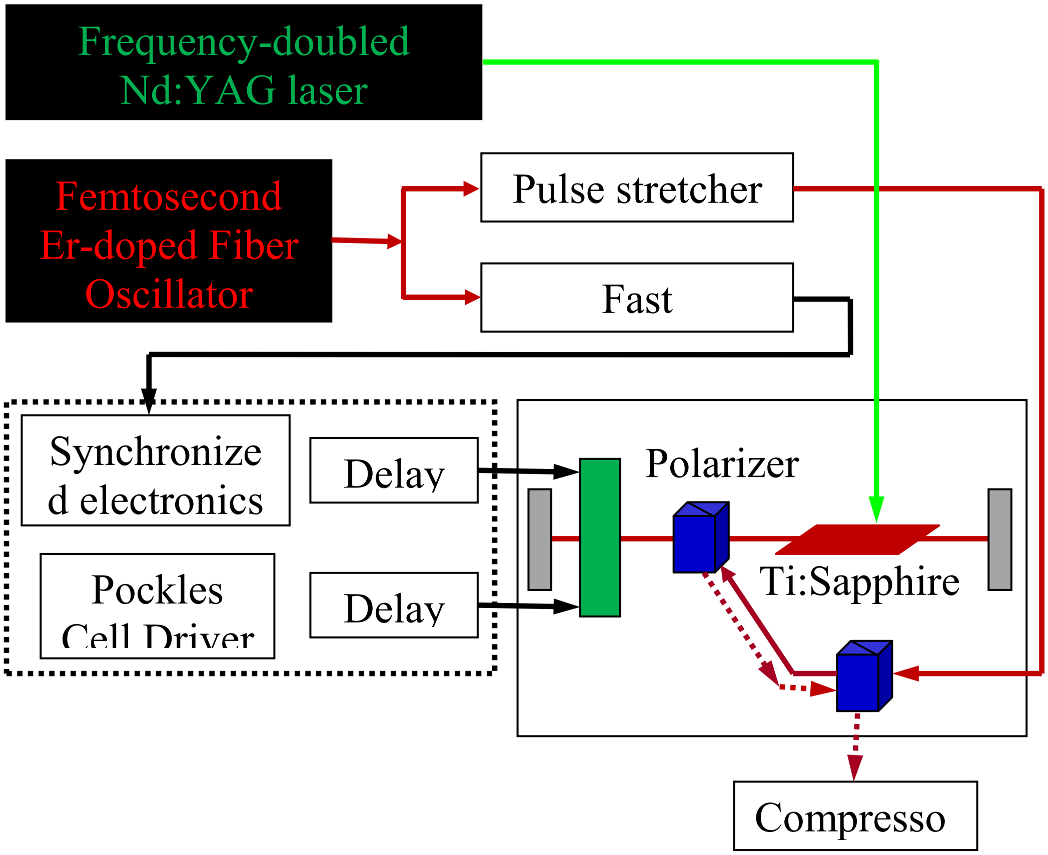

Figure 2.2. Sketch of the Quantronix laser system.

Our Ti:Sapphire regenerative amplifier system was purchased from Quantronix Titan, which was seeded by an erbium-doped fiber laser (Quantronix, IMRA, pumped by semiconductor diode laser). The doped fiber laser provided ~120 femtosecond laser pulses with repetition rate of 78 MHz. These femtosecond pulses went through the pulse stretcher and fed into, as a seed, into the Ti:Sapphire regenerative amplifier cavity. The gain medium is a Ti:Sapphire crystal pumped by the frequency-doubled Nd:YAG laser (532 nm). A fast photodiode outside the IMRA collected part of the seed laser pulses and then provided an input signal to the Pockels Cell Driver, which generated a reference signal to synchronize the timing of seed pulses, pump laser pulses and cavity damping. Finally, the pulse compressor compressed the cavity-damped, amplified pulses to the duration of around 120 fs. The CPA produced pulses of radiation with a wavelength of 780 nm, a pulse energy of ~ 1 mJ, and a pulse duration of ~ 120 fs at a tunable repetition rate up to 1 KHz by adjusting the external triggering of the Pockels cell. The basic layout of this system is shown in Figure 2.2.

2.1.2 Optical parametric amplifier

To study the wavelength-dependent nonlinear optics and ultrafast dynamics of semiconductor QDs, we utilized an optical parametric amplifier. Our system was a Quantronix light conversion TOPAS, which was based on a second-order nonlinear optical process and could provide tunable short pulses from 260 nm to 2500 nm. There were three stages in the TOPAS system. In the first stage, 10% of the pump beam from the amplifier generated superfluorescence in the nonlinear crystal (Sapphire). Then the desired wavelength from the superfluorescence was selected and amplified by part (20%)

of the remaining strong pump beam with appropriately angle and spatiotemporal overlap (Preamplifier) within a BBO crystal. In which the optical parametric process was employed to generate and amplify signal and idler photons by temporal and spatial overlap with the first pass pump light. After this, another amplification stage is set up using a different position in the same BBO crystal. The wavelength tuning of the OPA was done by selecting the phase match angle of the BBO crystal and the appropriate OPG generated light as well as by a harmonic generator setup using one or two additional BBO crystal. The average power of our TOPAS system was strongly wavelength and pump-power dependent, around 10 mW at 1000 nm with 1 W of 780-nm-wavelength light pump. The pulsewidth of the TOPAS beam was slightly longer than the pump laser and the repetition rate was the same as the pump laser (1 kHz).

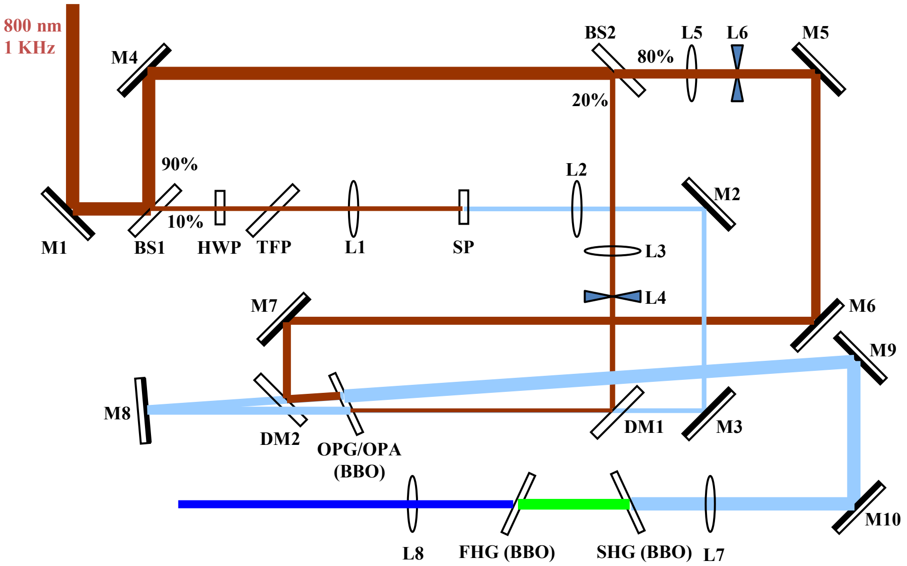

Figure 2.3. Optical parametric generator/amplifier schematic setup. M – mirror, DM – dichroic mirror, L – lens, HWP – half wave plate, TFP – thin film polarizer, BS – beam splitter, SP – sapphire plate, S(F)HG – second (fourth) harmonic generation.

2.1.3 Focused Gaussian laser beam [2, 3]

To study the nonlinear optical and ultrafast dynamical properties, the output laser pulses are usually focused into the samples to achieve the desired high pump intensity and small excitation volume by an optical focal lens. The electric field of a TEM_{00} mode focused Gaussian laser beam can be expressed as:

$$E(r,z,t) = \hat{e}A(z,t)\frac{w_0}{w(z)}\exp\{i[kz - \tan^{-1}(\frac{z}{z_0}) - \omega t + \frac{kr^2}{2q(z)}]\} + c.c. \tag{2.1}$$

where k is the wave vector of propagation and ω is the circular frequency of the rapidly oscillating wave. $A(r, t)$ is the wave amplitude which has a space and time dependence. $\hat{e}$ is the polarization unit vector of the wave. The notation "c.c." implies complex conjugate. $r = (x^2 + y^2)^{1/2}$ is the radial coordinate, $q(z) = z - iz_0$ is the complex radius of wave front curvature. $w(z)$ is the variable beam radius, which is defined as the half-width of the Gaussian curve at the point r, where the curve is at $1/e$ of its maximum value. $2w_0$ is defined as the beam waist, which is the minimum beam diameter at $z = 0$. The relationship between $w(z)$ and w_0 is given by

$$w(z) = w_0[1 + (\frac{z}{z_0})^2]^{1/2} \tag{2.2}$$

z_0 is called the Rayleigh range and is defined by

$$z_0 = \frac{\pi w_0^2}{\lambda} \tag{2.3}$$

where λ is the optical wavelength in free space. The distance between the points ± z_0 is called the confocal parameter b ($b = 2z_0$). This beam form is illustrated in Figure 2.4.

If converted to light intensity, the expression for a focused Gaussian laser beam can be simplified as

$$I(z,r,t) = I_{00}\exp(-\frac{2r^2}{w^2}) \times \exp(-\frac{t^2}{\tau_p^2}) \times (1+\frac{z^2}{z_0^2})^{-1} \tag{2.4}$$

I_{00} is the on-axis peak irradiance at focus point and τ_p is the pulse duration.

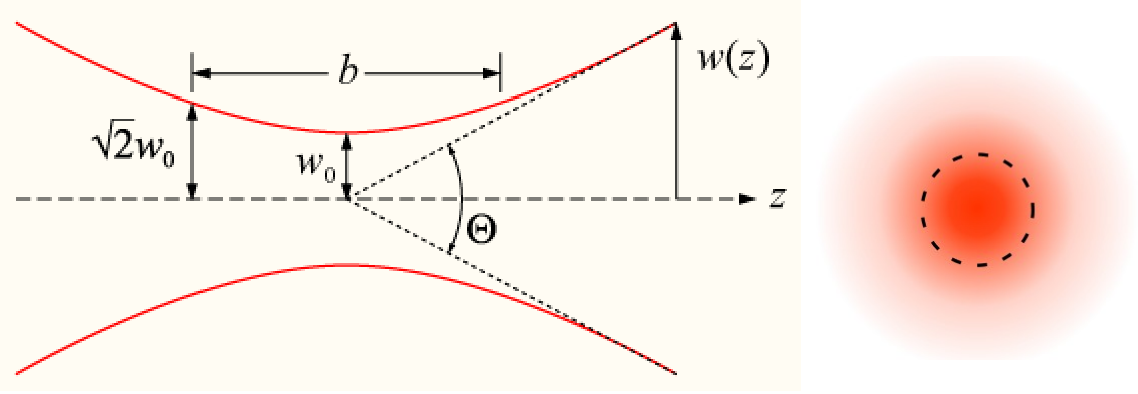

Figure 2.4. Schematic illustration of a TEM_{00} mode Gaussian laser beam propagation profile and cross section profile. [2, 3]

2.2 Z-scan technique

To quantitatively determine the nonlinear optical properties of materials, many techniques have been employed in the last few decades. The typical ones are nonlinear interferometry [4, 5], degenerate four-wave mixing [6], nearly degenerate three-wave mixing [7], ellipse rotation [8], beam-distortion measurements [9], and Z-scan [10, 11]. The first four methods are potential sensitive techniques. However, these techniques need complicate setups and skillful personnel. Compared with these four techniques, Z-scan provides a much easier and quicker determination of both the sign and magnitude of nonlinear refraction and nonlinear absorption. The Z-scan technique was introduced and first theoretically modeled by Sheik-Bahae et al. in 1990. Since then, it has been widely used as a standard method to characterize various nonlinear optical properties. Generally speaking, it is based on the transformation of phase distortion to amplitude change during the beam propagation. In experiment, we record the far field aperture energy transmittance as the sample is moved along the z direction through the focused Gaussian laser beam. In recent years, the Z-scan technique has been largely extended with the modifications as: EZ scan [12], two-color Z-scan [13, 14], Z-scan with top-hat beams [15], and time-resolved Z-scan [16].

For the standard Z-scan experiments, the schematic experimental setup is illustrated in Figure 2.5.

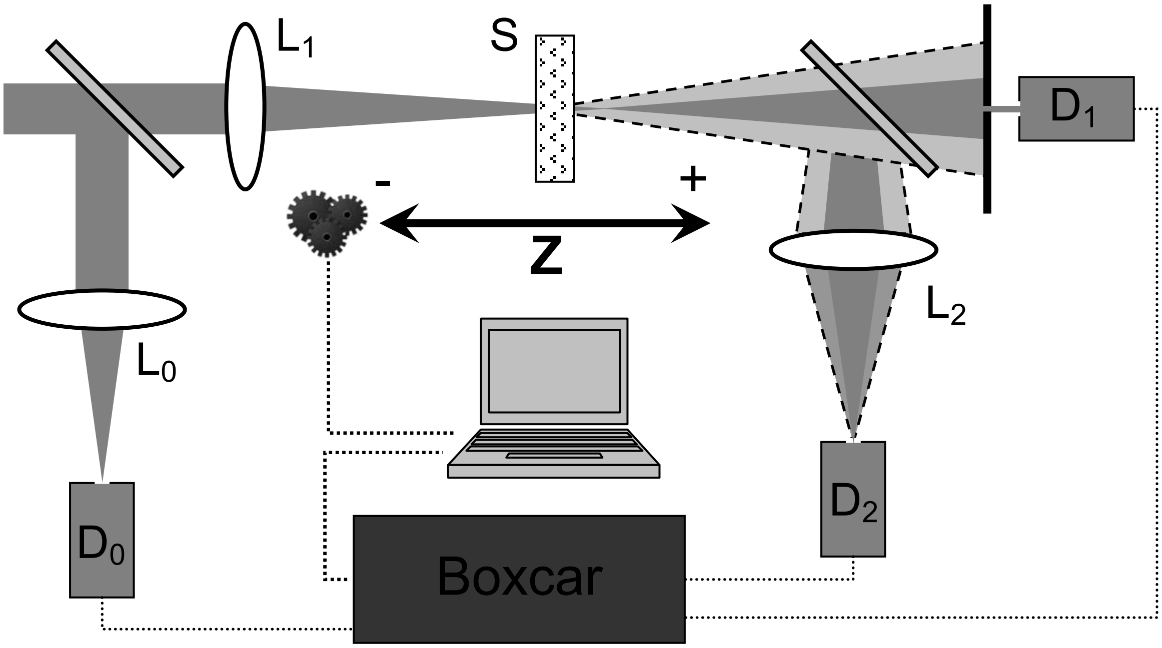

Figure 2.5. Z-scan setup in which the energy ratio D_1/D_0 (close-aperture) and D_2/D_0 (open-aperture) is recorded as a function of the sample position Z. *L* is lens, *S* is ample.

Two types of Z-scan are usually conducted. The first type is **open-aperture Z-scan** which is used to determine the nonlinear absorption of materials. In this experiment, all the transmitted light through the sample is collected with a focus lens and directed to the energy detector D_2. Then the energy ratio D_2/D_0 is recorded as a function of the sample position z. The second type is **closed aperture Z-scan** which is used to determine the nonlinear refraction of materials. In this experiment, only the small part of light beam near the Z axis can pass through the pinhole which is placed in the far field and before the energy detector. As illustrated in Figure 2.5, the energy ratio D_1/D_0 is recorded as the function of z.

2.2.1. Z-scan data analysis

Nonlinear optics is the discipline in physics in which the electric polarization density of the medium is studied as a nonlinear function of the electromagnetic field of the light. [17] In general, the electric field of a monochromatic light beam at angular frequency ω can be expressed as

$$E(t) = 1/2\ E_\omega \exp(-\mathrm{i}\omega t) + \mathrm{c.c.} \tag{2.5}$$

Correspondingly, the electric field induced medium polarization is

$$P(t) = 1/2\ P_\omega \exp(-\mathrm{i}\omega t) + \mathrm{c.c.} \tag{2.6}$$

At low pump light intensity, the polarization P is almost linearly dependent on the pump electric field E. If neglecting anisotropy of the medium, the optical properties can be fully described with the refractive index $\tilde{n}(\omega)$ (or the relative dielectric constant $\varepsilon_r(\omega)$ or the susceptibility $\chi(\omega)$. $\varepsilon_r(\omega) = \tilde{n}(\omega)^2 = 1 + \chi$). That is: $P_\omega = \varepsilon_0\chi(\omega)E_\omega$ where ε_0 is the dielectric constant of vacuum.

At high pump light intensity, the polarization P is not linearly dependent on E anymore. The E higher order terms must be taken into account. [18, 19] Now, the P can be expressed as: $P = P^{(L)} + P^{(NL)}$, where $P^{(L)}$ is the linear response part and $P^{(NL)}$ is the nonlinear response part. For central symmetric medium, only the odd powers of E need to be considered. Then the lowest nonlinear order terms is the cubic term, which is the third-order nonlinear term.

Here we use the determination of third-order nonlinear optical properties with Z-scan as an example. Then the third-order susceptibility ($\chi^{(3)}$) need to be considered. The pump laser intensity dependent refractive index and absorption coefficient can be expressed as [20, 21]

$$n = n_0 + n_2 \mathrm{I} \tag{2.7}$$

$$\alpha = \alpha_0 + \alpha_2 \mathrm{I} \tag{2.8}$$

where I is the incident pump light intensity, n_0 is the linear refractive index, α_0 is the linear absorption coefficient, and n_2 ($= \frac{3}{4}\frac{\mathrm{Re}(\chi^{(3)})}{n_0^2 c\varepsilon_0}$) and α_2 ($= \frac{3}{2}\frac{\omega}{\varepsilon_0 n_0^2 c^2}\mathrm{Im}(\chi^{(3)})$) are the nonlinear refraction index and nonlinear absorption coefficient respectively.

Eq. (2.7) means that when a focused laser beam is incident on the sample, the refractive index is changed according to the laser beam spatiotemporal intensity distribution. This effect is similar to creating a lens inside the sample when the incident laser beam possesses a spatial Gaussian intensity distribution. In a closed aperture Z-scan experiment, when the sample is moved along the beam propagation axis in vicinity to the focal point of an external lens, the far field energy transmitted through a small aperture, which is inserted on the beam propagation axis, is collected as a function of position z (As shown in Figure 2. 5). At each position z, the Gaussian laser beam is focused to different peak intensity. Then the lens created by this beam inside the sample is of different focal length. The nearer the sample is moved to the external focal point, the shorter the induced lens focal length becomes. The induced lens is a convergent lens or a divergent lens is determined by the sign of n_2. For an induced **convergent lens** (positive n_2) and a negative sample position (see Figure 2. 5), the transmitted beam converges before the external focal point. Therefore, the transmitted laser beam is enlarged at the aperture position compared with the case without the sample, and the energy collected by the detector decreases. When the sample moved to the external lens focal point ($z = 0$), the transmitted beam size at the aperture is the same as the original one without the sample, hence the energy collected by the detector is also the same. However, when the sample is moved to the positive z, the divergence of the beam is reduced by the induced sample lens. The beam size is reduced at the aperture position and the energy collected by the detector increases. Correspondingly, the overall closed aperture Z-scan curve is a valley followed by a peak (As shown by the solid line in Figure 2. 6 (a)). For an induced **divergent lens** (negative n_2), a reverse closed aperture Z-scan trend is observed. That is a peak followed by a valley (As shown by the dashed line in Figure 2. 6 (a)).

Eq. (2.8) means that the third-order nonlinear absorption coefficient is dependent on the pump intensity. When the total incident photon energy is fixed, the nearer the sample is moved to the external lens focal point, the higher nonlinear absorption can be obtained. However, the sign of the Z-scan signal is dependent on the sign of α_2. If the nonlinear absorption is a saturable absorption process whose α_2 is negative, then the signal is positive (by the dashed line in Figure 2. 6 (b)). Otherwise, the nonlinear absorption like two-photon absorption ($\alpha_2 > 0$) produces a negative Z-scan signal (by the solid line in Figure 2. 6 (b)).

In closed aperture Z-scan, when both third-order nonlinear refraction and third-order nonlinear absorption are co-present and co-dominate, the overall curve is the superimposition of the pure nonlinear refraction and pure nonlinear absorption as shown in Figure 2. 6 (c) and (d).

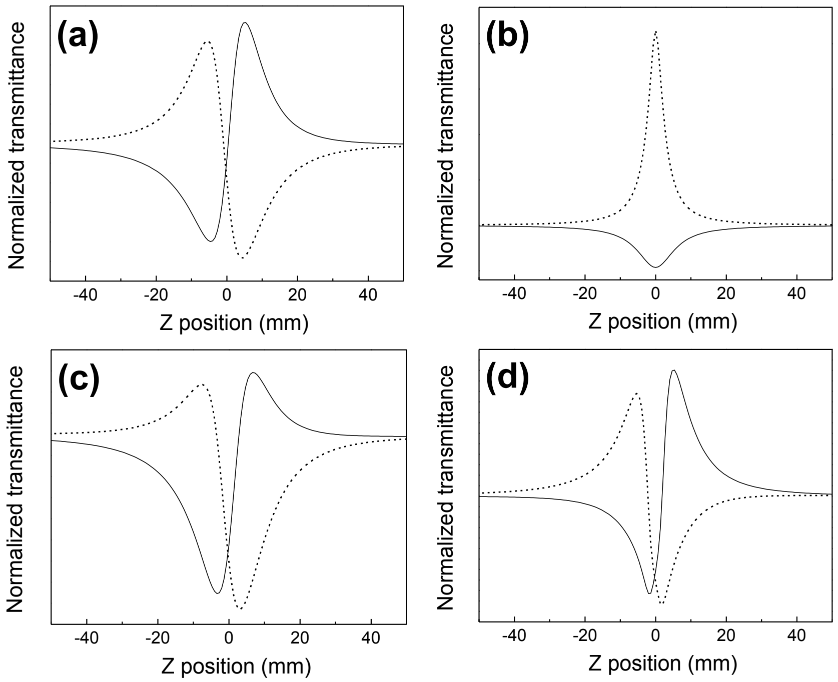

Figure 2.6. Typical Z-scan curves for (a) closed-aperture pure nonlinear refraction with $n_2>0$ (solid line) and $n_2<0$ (dashed line). (b) open-aperture pure nonlinear absorption with $\alpha_2>0$ (solid line) and $\alpha_2<0$ (dashed line). (c) closed-aperture nonlinear absorption ($\alpha_2>0$) with $n_2<0$ (dashed line) and $n_2>0$ (solid line). (d) closed-aperture saturable absorption ($\alpha_2<0$) with $n_2<0$ (dotted line) and $n_2>0$ (solid line).

To quantitatively relate these Z-scan traces with the nonlinear parameters of the medium, for simplicity, here we still take the third-order nonlinear optics as a demonstration. To simplify the data analysis, the "thin sample" approximation is usually applied. It means the sample is so thin that when a Gaussian laser beam is focused into the medium, the change in beam diameter within the sample due to either diffraction or nonlinear refraction is negligible. This requirement can be reached once the sample length (L) is smaller than the diffraction length (z_0). Then the intensity (I) and phase (ϕ) of the optical electrical field can be expressed as

$$\frac{d\Delta\phi}{dz'} = kn_2 I \tag{2.9}$$

$$\frac{dI}{dz'} = -(\alpha_0 + \alpha_2 I)I \tag{2.10}$$

where k is the magnitude of wave vector, and z' is the propagation depth inside the sample.

For **open-aperture Z-scan**, all the transmitted light is collected by another focal lens L_2 to D_2. Hence only the Eq. (2.10) needs to be considered. Integrate Eq. (2.10) over the whole sample length; the light intensity at the exit surface of the sample can be expressed as

$$I_e(z,r,t) = \frac{(1-R)^2 I_i(z,r,t)e^{-\alpha_0 L}}{1+q(z,r,t)} \tag{2.11}$$

where

$$q(z,r,t) = (1-R)\alpha_2 I_i(z,r,t)L_{eff} \tag{2.12}$$

and

$$L_{eff} = \frac{(1-e^{-\alpha_0 L})}{\alpha_0} \tag{2.13}$$

Here the reflection on the sample front surface has been considered. Further, taking into account the spatiotemporal Gaussian laser beam distribution, the normalized energy transmittance can be calculated as

$$T(z) = \frac{\mathrm{E}_e(z)}{\mathrm{E}_i(z)} = \frac{\int_{-\infty}^{\infty}\int_0^{\infty} I_e 2\pi r \cdot dr \cdot dt}{\int_{-\infty}^{\infty}\int_0^{\infty} I_i 2\pi r \cdot dr \cdot dt}$$

$$= \frac{\int_{-\infty}^{\infty}\int_{0}^{\infty} \frac{(1-R)^2 e^{-\alpha_0 L} I_{00} \exp(-\frac{t^2}{\tau_p^2}) \exp(-\frac{2r^2}{w^2})(1+\frac{z^2}{z_0^2})^{-1}}{1+\alpha_2 L_{eff}(1-R) I_{00} \exp(-\frac{t^2}{\tau_p^2}) \exp(-\frac{2r^2}{w^2})(1+\frac{z^2}{z_0^2})^{-1}} 2\pi r \cdot dr \cdot dt}{\int_{-\infty}^{\infty}\int_{0}^{\infty} I_{00} \exp(-\frac{t^2}{\tau_p^2}) \exp(-\frac{2r^2}{w^2})(1+\frac{z^2}{z_0^2})^{-1} 2\pi r \cdot dr \cdot dt}$$

$$= \frac{(1-R)^2 e^{-\alpha_0 L}}{\sqrt{\pi} q(z,0,0)} \int_{-\infty}^{\infty} \ln \cdot \left[1+q(z,0,0)\cdot e^{-x^2}\right] \cdot dx \qquad (2.14)$$

This result is the quantitative description of the sample position (*z*) dependent normalized energy transmittance. In Eq. (2.14), all the parameters are known or can be determined with other experiments except the nonlinear absorption coefficient (α_2). From the best fitting to the experiment curves, α_2 can be unambiguously determined.

For the concern of this thesis, the three photon absorption is also deduced with the same method as below:

$$\frac{dI}{dz'} = -(\alpha_0 + \alpha_3 I) I \qquad (2.15)$$

Similarly, the transmitted intensity can be expressed as

$$I_e(z,r,t) = \frac{(1-R)^2 I_i(z,r,t) e^{-\alpha_0 L}}{(1+p^2(z,r,t))^{1/2}} \qquad (2.16)$$

where $$p(z,r,t) = (2(1-R)^2 \alpha_3 I_i^2(z,r,t) L_{eff}^{'})^{1/2} \qquad (2.17)$$

$$L_{eff}^{'} = \frac{(1-e^{-2\alpha_0 L})}{2\alpha_0} \qquad (2.18)$$

The normalized energy transmittance can be calculated to

$$\begin{aligned} T(z) &= \frac{\mathrm{E}_e(z)}{\mathrm{E}_i(z)} \\ &= \frac{(1-R)^2 \exp(-\alpha_0 L)}{\sqrt{\pi} p(z,0,0)} \int_{-\infty}^{\infty} In[\sqrt{1+p^2(z,0,0)\cdot \exp(-2x^2)} + p(z,0,0)\exp(-x^2)]dx \end{aligned} \qquad (2.19)$$

For **closed aperture Z-scan**, only the transmitted light passing through the aperture is collected. The phase variation changes the energy transmittance through the aperture. The phase change can be deduced from Eq. (2.9) and (2.10)

$$\Delta\phi(z,r,t) = \frac{kn_2}{\alpha_2}\ln[1+q(z,r,t)] \tag{2.20}$$

The electric field at the exit surface of the medium can be deduced by combining Eq. (2.11) and (2.15):

$$E(z,r,t) = \frac{2}{\varepsilon_0 c n_0} e^{i\Delta\phi}\sqrt{I_e(z,r,t)} \tag{2.21}$$

At the far field position of the aperture, based on the Huygens-Fresnel theory, the electric field is determined by

$$E_a(z,r,t) = \frac{2\pi}{i\lambda(d-z)} e^{\frac{i\pi r^2}{\lambda(d-z)}} \int_0^{\infty} r' E(z,r',t) e^{\frac{i\pi r'^2}{\lambda(d-z)}} J_0[\frac{2\pi r r'}{\lambda(d-z)}]dr' \tag{2.22}$$

where *d* is the distance between the focal point and the aperture. $J_0(x)$ is the zero order Bessel's function. The transmitted power at time *t* through the aperture is then given as:

$$P_t(z,t) = c\varepsilon_0 n_0 \pi \int_0^{r_a} \left|E_a(z,r,t)\right|^2 rdr \tag{2.23}$$

where r_a is the radius of the aperture. Then the normalized energy transmittance is:

$$T(z,s) = \frac{\int_{-\infty}^{\infty} P_t(z,t)dt}{s\int_{-\infty}^{\infty} P_i(t)dt} \tag{2.24}$$

where $p_i(t) = I_{00}\frac{\pi\omega_0^2}{2} e^{-(\frac{t}{\tau_p})^2}$ and $s = 1 - e^{-2(\frac{r_a}{\omega_a})^2}$

Under the condition of small refraction and absorption change, the closed aperture Z-scan normalized energy transmittance can be expressed as [22-24]

$$T_{cl}(z) \cong 1 + \frac{kn_2 \mathrm{I}_{00} L_{eff}}{\sqrt{2}} \frac{4x}{(1+x^2)(9+x^2)} - \frac{\alpha_2 \mathrm{I}_{00} L_{eff}}{2\sqrt{2}} \frac{(3+x^2)}{(1+x^2)(9+x^2)} \tag{2.25}$$

where ω_a is the beam waist at the aperture position, $x = z/z_0$ and s is the linear transmittance of the aperture. By fitting Eq. (2.14) to the open-aperture Z-scan, α_2 can be obtained. Fitting Eq. (2.20) to the closed aperture Z-scan curves with this obtained α_2, n_2 value can be obtained.

Eq. (2.20) is quite complicate. For a faster and easier determination of n_2, the closed aperture Z-scan data is usually divided by the open-aperture one which is obtained under the same pump intensity. This ratio data closely represents the pure nonlinear refraction curve. From Eq. (2.20), the transmittance difference between peak and valley in this closed aperture Z-scan data can be deduced as:

$$\Delta \mathrm{T}_{p-v} \cong 0.406 \frac{1}{\sqrt{2}} (1-s)^{0.25} |\Delta \phi_0| \tag{2.26}$$

where $\Delta \phi_0 = \frac{2\pi}{\lambda} n_2 I_{00} L_{eff}$.

The analysis of the third-order nonlinear optical experiments has been presented above. In addition, the Z-scan analysis for the fifth-order nonlinear process is also demonstrated. In general, for higher-order nonlinear processes, Z-scan can still be applied, though the analysis details vary. Our Z-scan setup picture is shown in Figure 2.7.

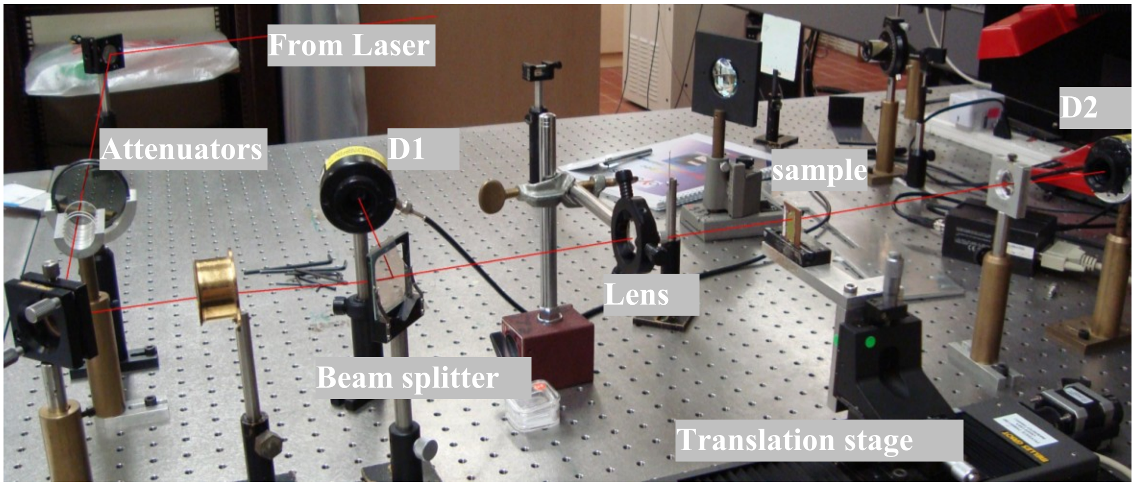

Figure 2.7. A picture of our open-aperture Z-scan setup. The transmittance (energy ratio of D_2/D_1) is recorded as a function of the sample position z. D_1 and D_2 are the energy detectors. The sample is moved along the optical propagation axis in vicinity of the focus point by a translation stage controlled by a computer. The closed-aperture Z-scan is conducted with an aperture inserted before the collecting lens.

2.3 Pump-probe technique

The ultrafast carrier dynamics within different energy states were studied with a home-built set-up for standard measurements on femtosecond time-resolved frequency-degenerate transient absorption. [25-27]. This kind of measurements is also called the pump-probe technique. In the past three decades, this technique has been widely applied to study the excited state absorption, saturable absorption and stimulated emission, carrier-carrier scattering, carrier-optical and carrier–acoustic phonon coupling and etc. A typical schematic setup for our pump-probe measurements is shown in Figure 2.8. Here, the pulse train produced by the laser is split by a beam splitter into a strong pump train and a weaker probe train. The probe train optical path length is usually under the control of computer-controlled delay stage. This mechanical delay stage allows one to access the dynamics of the sample at a controllable time after the arrival of the pump pulse. Since the speed of light is so large, performing measurements with high-resolution is relatively easy using this mechanical scheme. An alternate pump-probe setup might send the pump train into a delay stage which shortens or lengthens the path of the pump relative to the probe. Both these two setup are equivalent. The longest delay achievable with this system corresponds to the delay stage length and the passed times of the delayed train through the delay stage. The above mentioned method seems quite easy. However, to obtain the desired data in real experiments is quite difficult. Since the pump induced probe transmittance change is usually quite small. This signal is easily swamped by environmental noise such as vibrations, temperature changes in the room, and instability in the laser output. There are several established methods to recover the signal from these complicated factors. The common method is the lock-in technique. In experiment, we can use a chopper to periodically modulate the pulse train. This periodicity should be reflected in the sample and influence the probe train with the same periodicity. Then we can use a lock-in amplifier referenced to the modulation frequency in order to recover the desired signal even if it is buried within noise orders of magnitude larger. Here, we must choose a modulation frequency that does not convolve the signal with a particularly common source of noise, such as multiples of electric frequency.

In our experiment, the polarization of the pump beam was set perpendicular to the probe beam. The intensity of the probe beam was controlled by a quarter wave plate and a polarizer. The intensity of the pump beam was controlled by neutral density filters. For white light probe experiments, the probe beam was focused into a 2 mm sapphire plate to generate broad band white which was recollected with another lens. In some of the experiments, we doubled the frequency of the red pump light (780 nm) to blue one (390 nm) (As schematically shown in Figure 2.8). The real experiment setup is shown in Figure 2.9.

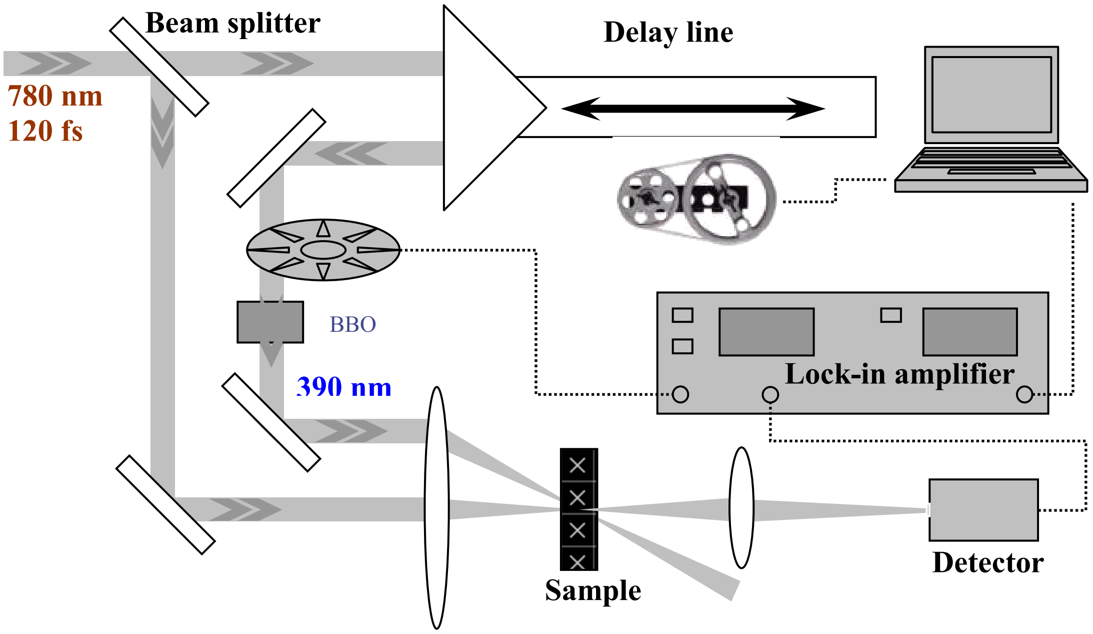

Figure 2.8. Schematic pump-probe setup. The detector after the sample measures the energy difference of the probe beam in the presence (T) and absence (T_0) of the pump pulse.

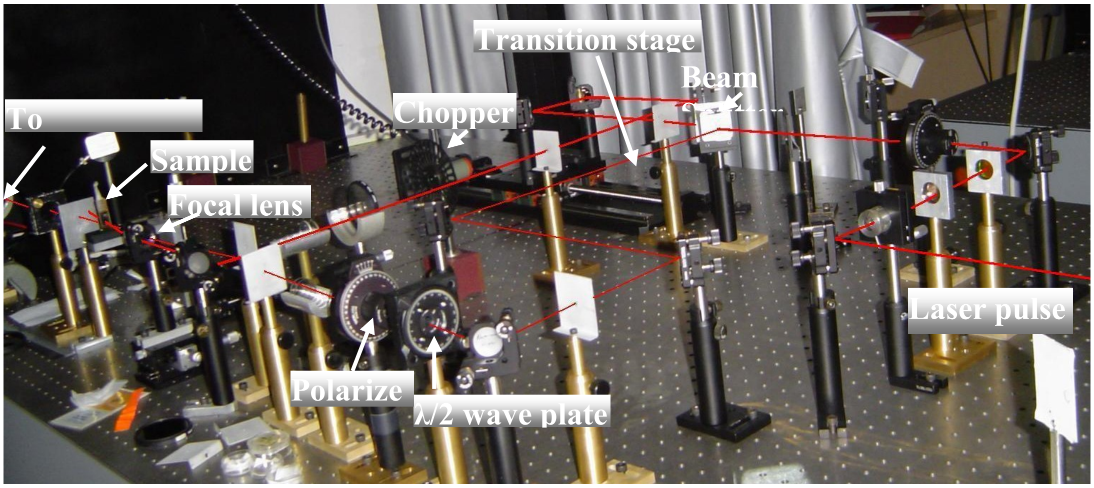

Figure 2.9. The graph of the frequency-degenerate pump-probe set-up; the detector connected to lock-in amplifier measures the transmitted light energy difference between the presence (T) and absence (T_0) of the pump pulse.

Normally, the pump-probe signal is quite complicate. It is easy to fit the experimental data and obtain the dynamic lifetimes, but not easy to quantitatively describe the amplitude. The signal is strongly related with the investigated system, the pump wavelength, pump intensity and probe wavelength and intensity. Generally, if the probe intensity is weak enough when compared with pump beam (≤ 1/10), the obtained signal intensity after the two beam temporal overlap can be expressed as:

$$S \propto p_2 e^{-(\alpha_0 + N_{e-h} k)L} / p_2 e^{-\alpha_0 L} \approx -p_2 N_{e-h} L \cdot e^{-\alpha_0 L} \tag{2.27}$$

where p_2 is the probe beam energy, α_0 is the sample absorption coefficient of the probe beam without the pump beam, N_{e-h} is the density of electron-hole pairs generated by the pump beam. If the two-photon absorption dominates in the pump beam excitation process, then

$$\frac{dN_{e-h}}{dt} = \frac{\beta I_1^2}{2\hbar\omega} - \frac{N_{e-h}}{\tau_{eff}} \tag{2.28}$$

where τ_{eff} is the electron-hole recombination time. The pump-probe signal is square dependent on the pump intensity and linear dependent on the probe beam intensity. However, if the three-photon dominates in the pump beam exicitation process, then

$$\frac{dN_{e-h}}{dt} = \frac{\alpha_3 I_1^2}{3\hbar\omega} - \frac{N_{e-h}}{\tau_{eff}} \tag{2.29}$$

The pump-probe signal is cubic power dependent on the pump intensity and linear dependent on the probe beam intensity.

2.4 Upconversion photoluminescence (PL) technique

One of the important applications of the nonlinear optics is the upconversion PL which can be used in upconversion lasing, [28] upconversion bio-imaging, [29] and etc. Correspondingly, in the case of fluorescent materials, the nonlinear optical properties can be investigated through the multiphoton (N-ħω) excited PL. The value N can be easily determined from the dependence of PL intensity on pump power. Compared with a standard multiphoton absorption cross-section of well studied PL phosphor under the same experimental conditions, the multiphoton absorption cross-section of a new material also can be extracted from this experiment (if the fluorescence emission quantum efficiencies are known). The upconversion PL technique provides ultra high detection sensitivity. Therefore, multiphoton absorption cross-sections can be measured in dilute sample solutions (usually $\leq 10^{-4}$ M) and low peak pump intensities (if the PL efficiency is known).

A schematic experimental setup for this technique is shown in Figure 2. 10. A 0-degree setup, where the detection path is parallel to the excitation path, can also be used. The laser pulses were focused by a lens (L_1, f = 15 cm) into the solution sample in a 1-cm-thick quartz cell, with a focal spot size of ~ 20 μm inside the cell (for 800 nm, 5 mm incident beam diameter). The emission from the sample was collected at an angle of 90° by a pair of lenses, and directed to a spectrometer (Acton, Spectra Pro 2300i coupled CCD Princeton Instruments, Pixis 100B). A short-pass filter with a cut-off wavelength of ~50 nm shorter than the excitation wavelength was placed before the spectrometer to minimize the scattered excitation light.

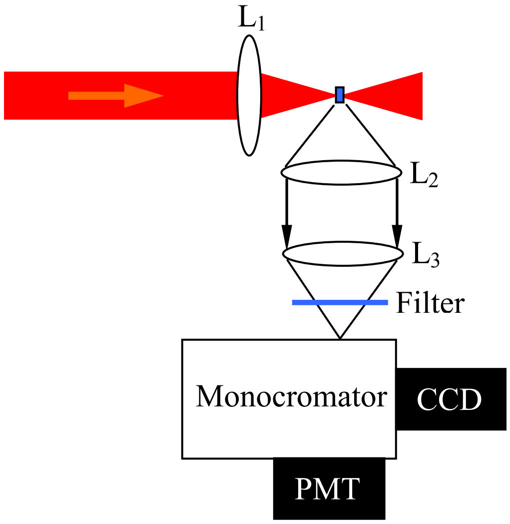

Figure 2.10. Schematic experimental setup for upconversion luminescence.

To quantitatively describe the multiphoton excited PL, here we show the consideration of two- and three-photon excitation as examples. Within the focused Gaussian laser beam the multiphoton excited PL can be described as:

$$\Delta F_2 = \phi\eta_2\sigma_2\rho I^2(\vec{r},t)dV \qquad (2.30)$$

$$\Delta F_3 = \phi\eta_3\sigma_3\rho I^3(\vec{r},t)dV \qquad (2.31)$$

where ϕ is the system PL collection efficiency; η_2 and η_3 are the two-photon and three-photon excited PL efficiency respectively; σ_2 and σ_3 are the two-photon and three-photon absorption cross-section respectively; ρ is the sample number concentration; $I(\vec{r})$ is the light intensity at position $\vec{r}$; dV is a small volume within which the light intensity can be considered as constant.

If the laser intensity decreasing within the sample is not dramatically, which means the sample concentration is low or the multiphoton absorption cross-section is quite small, the total collected photons can be obtained by integrating Eq. (2.22) and Eq. (2.23) over the whole focused Gaussian laser beam:

$$F_2 = \int_{-\infty}^{\infty}\int_{-\infty}^{\infty}\int_{0}^{\infty} \Delta F_2 \cdot 2\pi r dr \cdot dz \cdot dt = \frac{\pi^{5/2}}{4}\tau\phi\eta_2\sigma_2\rho I_{00}^2 w_0^2 z_0 \tag{2.32}$$

$$F_3 = \int_{-\infty}^{\infty}\int_{-\infty}^{\infty}\int_{0}^{\infty} \Delta F_3 \cdot 2\pi r dr \cdot dz \cdot dt = \frac{\pi^{5/2}}{12}\tau\phi\eta_3\sigma_3\rho I_{00}^3 w_0^2 z_0 \tag{2.33}$$

where τ is the half wide of the Gaussian laser pulse at *1/e*; I_{00} is the peak power on the beam propagation axis; w_0 is the beam waist; z_0 is the diffraction length. At room temperature for QDs or molecules, the multiphoton excited quantum efficiency is very near to the one photon excited quantum efficiency. [30] Then the only unknown parameter is the multiphoton absorption cross-section.

2.5 Time-resolved PL technique

In this experiment, the setup is similar to the above-mentioned upconversion PL setup. However, the excitation is usually UV pulsed-laser source. The collected PL was firstly dispersed by the monochromator and then monitored at different wavelength (± 2 nm) with the Photo multiplier tube (PMT) which was coupled to a 400-MHz oscillograph. Time resolution of the setup was ~10 ns.

References:

[2.1] D. Strickland and G. Mourou, "Compression of amplified chirped optical pulses," *Opt. Commun*. **56**, 219 (1985).

[2.2] M. Born and E. Wolfe, Principles of Optics, 5th ed., Pergamon Press, New York, 1975.

[2.3] R. L. Sutherland, D. G. Mclean, and S. Kirkpatrick, Handbook of Nonlinear Optics, 2th ed., Marcel Dekker, Inc., New York (2003).

[2.4] M. J. Weber, D. Milam, and W. L. Smith, "Non-linear refractive-index of glasses and crystals," *Opt. Eng.* **17**, 463 (1978).

[2.5] M. J. Moran, C. Y. She, and R. L. Carman, "Interferometric measurements of nonlinear refractive-index coefficient relative to CS_2 in laser-system-related materials," *IEEE J. Quantum Electron.* **11**, 259 (1975).

[2.6] S. R. Friberg and P. W. Smith, "Nonlinear optical-glasses for ultrafast optical switches," *IEEE J. Quantum Electron*. **23**, 2089 (1987).

[2.7] R. Adair, L. L. Chase, and S. A. Payne, "Nonlinear refractive-index measurements of glasses using 3-wave frequency mixing," *J. Opt. Soc. Am. B* **4**, 875 (1987).

[2.8] A. Owyoung, "Ellipse rotation studies in laser host materials," *IEEE J. Quantum Electron.* **9**, 1064 (1973).

[2.9] W. E. Williams, M. J. Soileau, and E. W. Van Stryland, "Optical switching and n_2 measurements in CS_2," *Opt. Commun.* **50**, 256 (1984).

[2.10] M. Sheik-Bahae, A. A. Said, and E. W. van Stryland, "High-sensitivity, single-beam n_2 measurements," *Opt. Lett*. **14**, 955 (1989).

[2.11] M. Sheik-Bahae, A. A. Said, T. H. Wei, D. J. Hagan, and E. W. V. Styland, "Sensitive measurement of optical nonlinearities using a single beam," *IEEE J. Quantum Electron.* **26**, 760 (1990).

[2.12] T. Xia, D. J. Hagan, M. Sheik-Bahae, and E. W. Van Stryland, "Eclipsing Z-scan measurement of lambda/10(4) wave-front distortion," *Opt. Lett.* **19**, 317 (1994).

[2.13] M. Sheik-Bahae, J. Wang, R. Desalvo, D. J. Hagan, and E. W. Van Stryland, "Measurement of nondegenerate nonlinearities using a 2-color Z-scan," *Opt. Lett.* **17**, 258 (1992).

[2.14] F. Henari, J. Callaghan, H. Stiel, W. Blau, and D. J. Cardin, Chem. "Intensity-dependent absorption and resonant optical nonlinearity of C-60 and C-70 solutions," *Phys. Lett.* **199**, 144 (1992).

[2.15] W. Zhao and P. Palffy-Muhoray, "Z-scan measurement of Chi(3) using top-hat beams," *Appl. Phys. Lett.* **65**, 673 (1994).

[2.16] J. S. Meth, H. Vanherzeele, and Y. Wang, "Dispersion of the 3rd-order optical nonlinearity of C-60 - a 3rd-harmonic generation study," *Chem. Phys. Lett.* **197**, 26 (1992).

[2.17] F. Jonsson, Lecture Notes on Nonlinear Optics, KunGL, Tekniska Hogskolan (2003).

[2.18] Y. R. Shen, *The Principles of Nonlinear Optics*, Willy & Sons, New York (1984).

[2.19] P. N. Butcher and D. Cotter, *The Elements of Nonlinear Optics*, Cambridge University Press, (1990).

[2.20] K. Mansour, M. J. Soileau, and E. W. Van Stryland, "Nonlinear optical-properties of carbon-black suspensions (ink)," *J. Opt. Soc. Am. B* **9**, 1100 (1992).

[2.21] E. W. Van Stryland, Beam Shaping and Control with Nonlinear Optics, Kajzar and Reinisch, Ed., (Plenum Press, New York, 1998).

[2.22] M. Dinu, F. Quochi, and H. Garcia, "Third-order nonlinearities in silicon at telecom wavelengths," *Appl. Phys. Lett*. **82**, 2954 (2003).

[2.23] Y. Choi, J. H. Park, M. R. Kim, W. Je, and B. K. Rhee, "Direct observation of self-focusing near the diffraction limit in polycrystalline silicon film," *Appl. Phys. Lett.* **78**, 856 (2001).

[2.24] B. K. Rhee, J. S. Byun, and E. W. V. Stryland, "Z scan using circularly symmetric beams," *J. Opt. Soc. Am. B* **13**, 2720 (1996).

[2.25] J. Zhou, J. Peatross, M. M. Murnane, and H. C. Kapteyn, "Enhanced high-harmonic generation using 25 fs laser pulses," *Phys. Rev. Lett.* **76**, 752 (1996).

[2.26] L. E. Nelson, Ultrafast Phenomena IX, Springer Series in Chemical Physics, **62**, 18 (1996).

[2.27] J. P. Chambaret, et al., "Generation of 25-TW, 32 fs pulses at 10 Hz," *Opt. Lett.* **21**, 1921 (1996).

[2.28] G. S. He, P. P. Markowicz, T. C. Lin, and P. N. Prasad, "Observation of stimulated emission by direct three-photon excitation," *Nature* **415**, 767 (2002).

[2.29] B. R. Masters and T. C. Peter, "Handbook of biomedical nonlinear optical microscopy," OXFORD University Press (2008).

[2.30] G. S. He, K. T. Yong, Q. D. Zheng, Y. Sahoo, A. Baev, A. I. Ryasnyanskiy, and P. N. Prasad, "Multi-photon excitation properties of CdSe quantum dots solutions and optical limiting behavior in infrared range," *Opt. Express* **15**, 12818 (2007).

Chapter 3

Three-photon-excited, band-edge emission in water soluble, copper-doped ZnSe/ZnS QDs

3.1 Introduction

Two-photon-excited fluorescence imaging [3.1, 3.2] has been demonstrated to be a powerful technique for biological and medical applications. The success of such a multiphoton microscopy technique has prompted researchers to explore three-photon processes with hopes of improving spatial resolution, reducing undesirable linear absorption in living organisms, and enhancing signal-to-noise ratio by utilizing a longer excitation wavelength. In that regard, colloidal semiconductor QDs are promising since they have been reported to possess larger three-photon absorption (3PA) cross-sections compared to organic dyes [3.3-3.6]. While 3PA in semiconductor QDs has been investigated [3.3-3.6], research on their three-photon-excited luminescence is limited except for CdS QDs and CdSe QDs [3.3, 3.4]. CdS QDs and CdSe QDs show efficient three-photon-excited, band-edge emission, but the intrinsic toxicity of cadmium has cast a doubtful future in applications. Furthermore, the trap states in CdS QDs play an important role in the intensity dependence of luminescence at photon energies below the band edge, which was found to be non-cubic dependence [3.3]. The cubic dependence on the excitation intensity is crucial in achieving higher spatial resolution in imaging. These two issues may be overcome by using zinc chalcogenide doped with transition metal ions

[3.7, 3.8]. Here, we report on the synthesis, characterization, Z-scan, and photoluminescence (PL) measurements of aqueous solutions of core/shell structured ZnSe/ZnS QDs with or without copper doping. We demonstrate that the Cu-doped ZnSe/ZnS QDs exhibit high efficiency for below-band-edge PL and nearly cubic dependence on the excitation intensity of femtosecond laser pulses at 1000 nm, which is close to a semi-transparent window for many bio-imaging applications.

3.2 Synthesis and linear optical characterization

The synthesis of ZnSe/ZnS QDs was based on the reaction of zinc acetate with sodium hydroselenide in dimethylsulfoxide (DMSO) as solvent. Sodium hydroselenide was prepared by mixing sodium borohydride and selenium powder in methanol under nitrogen. When the selenium powder was completely reduced by $NaBH_4$, 10 ml of freshly prepared NaHSe solution (0.4 M in methanol) was added into another solution containing 50 ml of 0.2 M of zinc acetate (and 0.002 M copper acetate for 1% Cu doping) with vigorous stirring. Then NaHSe precursor, 6 ml of 1 M of Na_2S solution was injected under vigorous stirring. The resulting mixture was precipitated with 10 ml of 1 M of mercaptopropionic acid (MPA) (with pH adjustment to 11 with NaOH). After the centrifuge and washing, the precipitation was re-suspended in water, and then heated to 95ºC for 2 h to grow the QDs to a final size of ~ 4 nm.

The as-prepared QDs were first characterized with high resolution transmission electron microscope (TEM, JEOL-JEM 2010F) operating at 200 kV to inspect the morphologies and size distributions. The ZnSe/ZnS and Zn(Cu)Se/ZnS QDs were dissolved in water and a drop of the solution was placed on a copper grid with carbon film. It was dried in desiccators before transferring into the TEM sample chamber. The TEM results are shown in Figure 3.1(a) and Figure 3.2(a) for ZnSe/ZnS QDs and copper-doped ZnSe/ZnS respectively. They clearly show that these QDs are well crystallized. The average size is determined to be 4.4 (± 0.5) nm and 4.1 (± 0.5) nm for ZnSe/ZnS QDs and copper-doped ZnSe/ZnS respectively. The size dispersion is ~20 %.

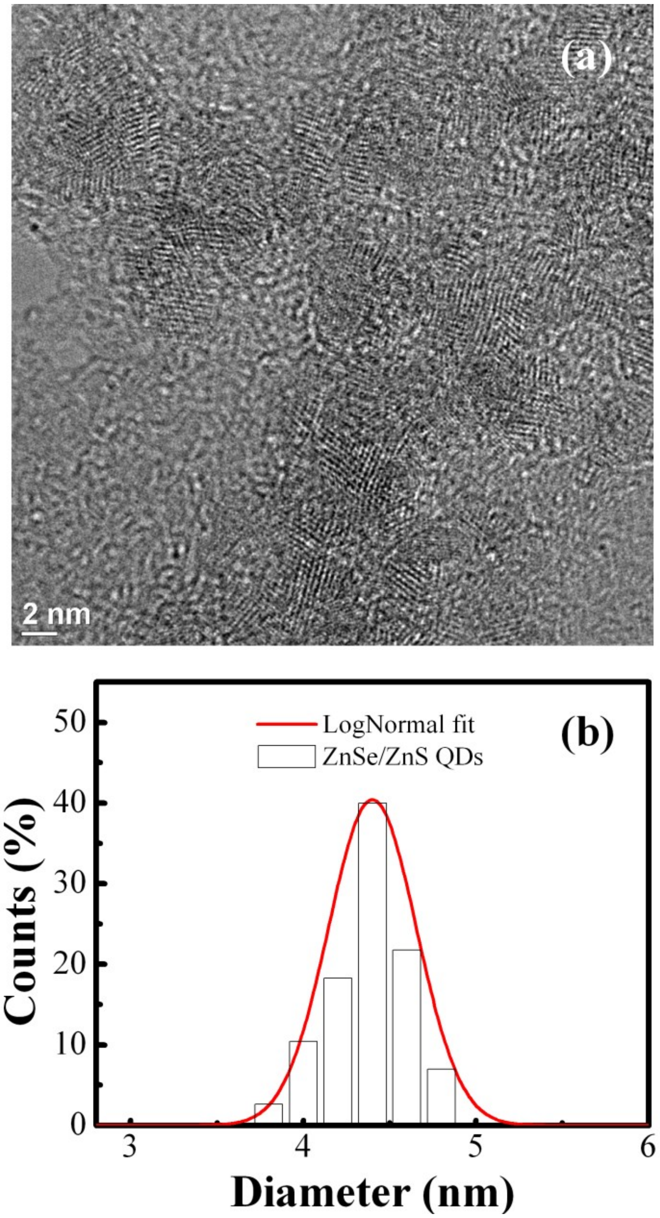

Figure 3.1. (a) TEM images of ZnSe/ZnS QDs. (b) Size dispersions of the ZnSe/ZnS QDs. The red solid line is a lognormal fit.

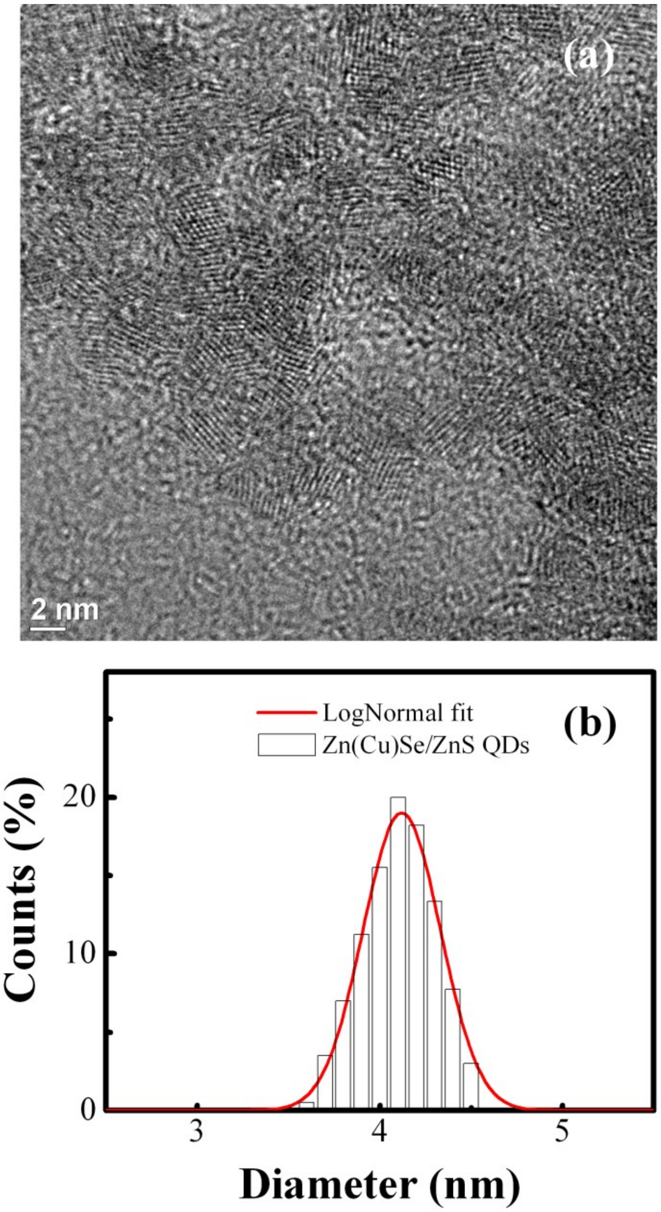

Figure 3.2. (a) TEM images of the copper-doped ZnSe/ZnS QDs. (b) Size dispersions of the copper-doped ZnSe/ZnS QDs. The red solid line is a lognormal fit.

To determine the crystal structures of these QDs, X-ray diffraction diffractograms (XRD) were recorded on a Siemens D5005 x-ray powder diffractometer with Cu *Kα* radiations (40 kV, 40 mA). The QDs powder was mounted on a sample holder and scanned with a step width of 0.01º in the range from 15º to 65º.

Typical XRD patterns of the un-doped and Cu-doped ZnSe/ZnS QDs are shown in Figure 3.3. The XRD of these QDs reveals diffraction peaks corresponding to the cubic (zinc blend) crystal structural form. However, upon copper doping, the diffraction peaks are slightly shifted towards larger angles and close to CuSe diffraction peaks. This result clearly shows the copper ions have been successfully doped into the lattice. Compared to the XRD of bulk ZnSe or CuSe, the present diffraction lines are generally broader. The finite size of the crystallites, strain, and instrumental effects contribute to the broadening. If assuming the particles are spherical in shape, the size of the QDs can be estimated according to the Debye-Scherrer formula [3.9].

$$d = \frac{4}{3} \times \frac{0.9 \times \lambda}{\Delta \times \cos(\theta)} \tag{3.1}$$

where λ is wavelength of X-rays; Δ is FWHM of diffraction peak; θ is angle corresponding to the peak. In this equation, the stress-related and instrument-related broadening is neglected. In order to obtain the diameters of QDs, the XRD 110 peak profiles are fitted with Lorentzian function. The calculation shows that the ZnSe/ZnS QDs has a diameter of 3.8 nm and copper-doped ZnSe/ZnS has a diameter of 4.0 nm. This estimation values are close to the TEM results.

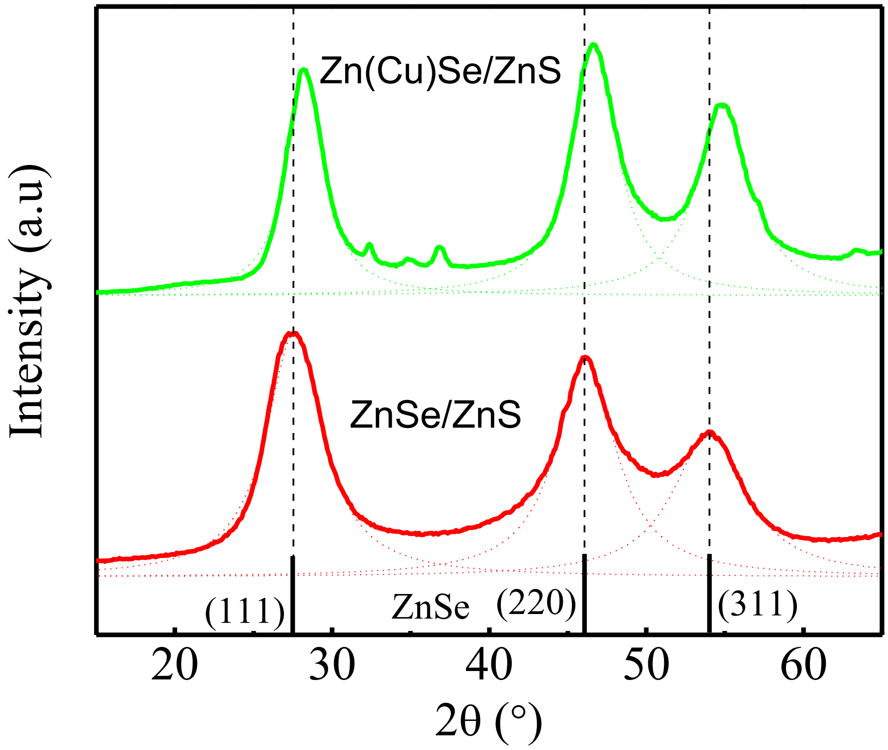

Figure 3.3. XRD patterns of un-doped (**red** line) and Cu-doped (**green** line) ZnSe/ZnS QDs. The dotted lines are the fits with Lorentzian curves.

The linear optical absorption spectra of the as prepared MPA capped QDs in water solution were characterized at room temperature with an UV-visible-infrared spectrophotometer (UV-1601, Shimadzu) from 300 nm to 800 nm. All the spectra were corrected with water in the same quartz cell. The obtained results are shown in Figure 3.4. For comparison, the spectrum of ZnSe/ZnS QDs was normalized to copper-doped ZnSe/ZnS QDs. The absorption onsets are localized at 410 nm and 400 nm for un-doped and Cu-doped ZnSe/ZnS QDs, respectively. Comparing with the absorption edge of bulk ZnSe (~ 440 nm), the absorption edges for the un-doped and Cu-doped ZnSe/ZnS QDs show a blue shift of 30 and 40 nm, corresponding to 0.20 and 0.28 eV, respectively. Hence, the quantum confinement effect is clearly shown here. The broadening of optical transitions observed in the absorption spectra is primarily due to inhomogeneity arising from size dispersion. According to Victor I. Klimov's theory [3.10], the linear absorption spectrum of QDs can be fitted with several Gaussian bands.

$$\alpha_0(\hbar w) = \sum_{i=1}^{n} \frac{a_i}{\sqrt{2\pi}\Gamma_i} \exp[-\frac{(\hbar w - \hbar w_i)^2}{2\Gamma_i^2}] \tag{3.2}$$

where a_i is the area of the $\hbar w_i$ transition, and $\Gamma_i = \frac{2\Delta_R}{R}(\hbar w_i - E_g) = 2\delta_R \Delta_i$ is the inhomogeneous broadening of the transition with energy $\hbar w_i$. Δ_R is the standard deviation of a Gaussian size distribution. In our case 3 such bands were chosen to fit the linear absorption spectra from 300nm to 500nm. The fitted results are shown as the solid black line in Figure 3.4. The lowest excitonic transition, $1S(e)$-$1S_{3/2}(h)$, in the un-doped ZnSe/ZnS QDs peaked at 390 nm, from which the average core diameter was computed to be ~ 4.6 nm, according to density functional theory under the corrected local density approximation [3.11]. It was in agreement with our measurement (4.4 ± 0.5 nm) by transmission electron microscopy (TEM). The $1S(e)$-$1S_{3/2}(h)$ transition in the 1% Cu-doped ZnSe core peaked at 365 nm, and the core diameter was estimated to be 4.1 nm, which agreed well with the TEM finding (4.1 ± 0.5 nm). From the curve fitting, the size distributions of un-doped and Cu-doped ZnSe/ZnS were found to be 12 % and 9 %, respectively. The fitted results are listed in Table 3.1. To check photo-stability of the two samples, we measured the absorption spectra before and after the laser irradiation and no difference was observed.

Table 3.1. The Gaussian fitted lowest band, second band, third band and size distribution of un-doped and Cu-doped ZnSe/ZnS QDs.

	Lowest band (ev)	Second band (ev)	Third band (ev)	Δ_R/R
ZnSe/ZnS	3.2	3.6	4.3	12.2%
Zn(Cu)Se/ZnS	3.4	3.7	4.2	9%

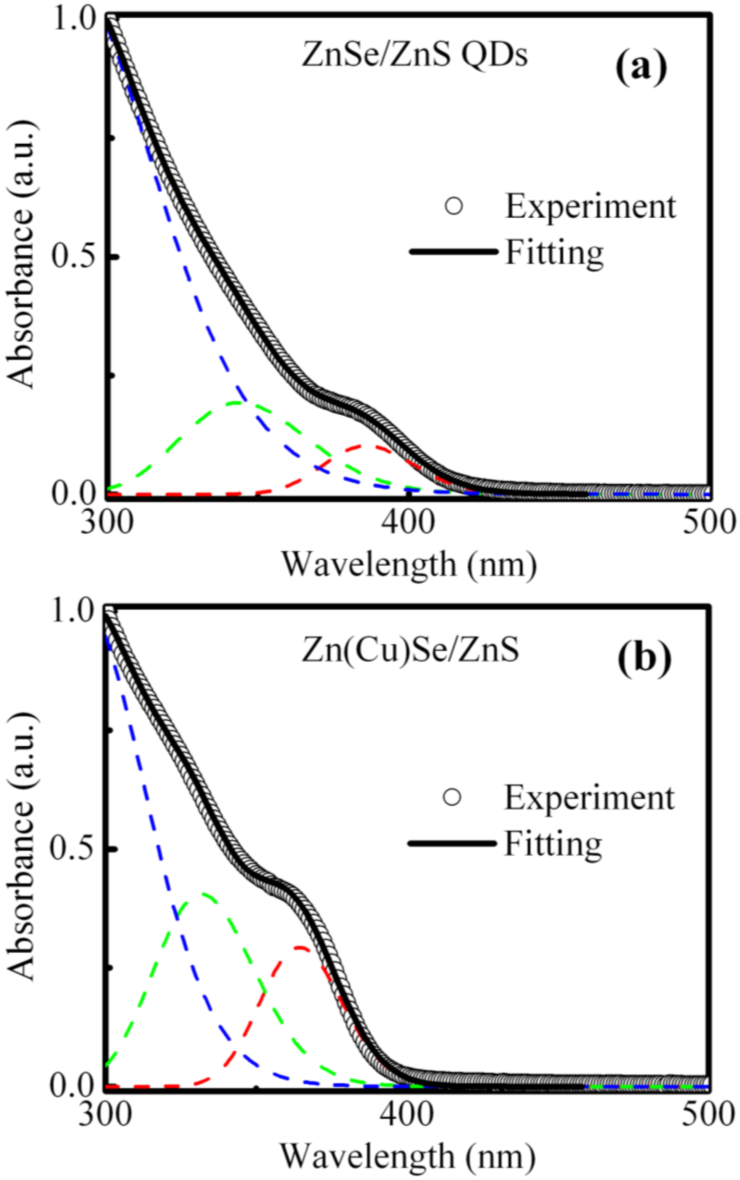

Figure 3.4. Optical absorption spectra of un-doped (a) and Cu-doped (b) ZnSe/ZnS QDs fitted to three Gaussian bands according to Equation (2).

The two samples were also characterized at room temperature by PL and photoluminescence excitation (PLE) spectroscopic techniques under one-photon excitation (see Figure 3.5). The spectra of ZnSe/ZnS QDs were normalized to those of Zn(Cu)Se/ZnS QDs for comparison. The PLE spectra showed that copper doping broadens the near-band-edge and higher-energy-level transitions compared with the undoped QDs, which was consistent with the findings on Cu-doped ZnS QDs [3.12].

From the PL spectra for the two types of QDs, one can conclude that band-to-band PL signals were completely quenched by defect states and/or copper-related states, respectively, in agreement with the observations by Pradhan *et al.* [3.8, 3.13]. The peak of the copper-related PL in the Zn(Cu)Se/ZnS QDs was red-shifted, compared with the PL signal of ZnSe/ZnS QDs which peaked at 498 nm originating mainly from the defect states. These spectroscopic results could be understood by photodynamics (see Figure. 3.6). Shortly after electrons were excited from the valence band to the conduction band in pure ZnSe, they relaxed to the defect states, from which they recombined with holes in the valence band, emitting photons in the green spectral region. However, if copper ions were present in ZnSe, radiative recombination between electrons in the defect states and holes in *d*-orbital of copper-ions would become dominant, with a 25-nm red-shift compared to pure ZnSe QDs. More significantly, we have found that the quantum efficiency of the copper-related PL was greatly enhanced by ~ 20 fold, in agreement with the findings by Pradhan *et al.* [3.8, 3.13].

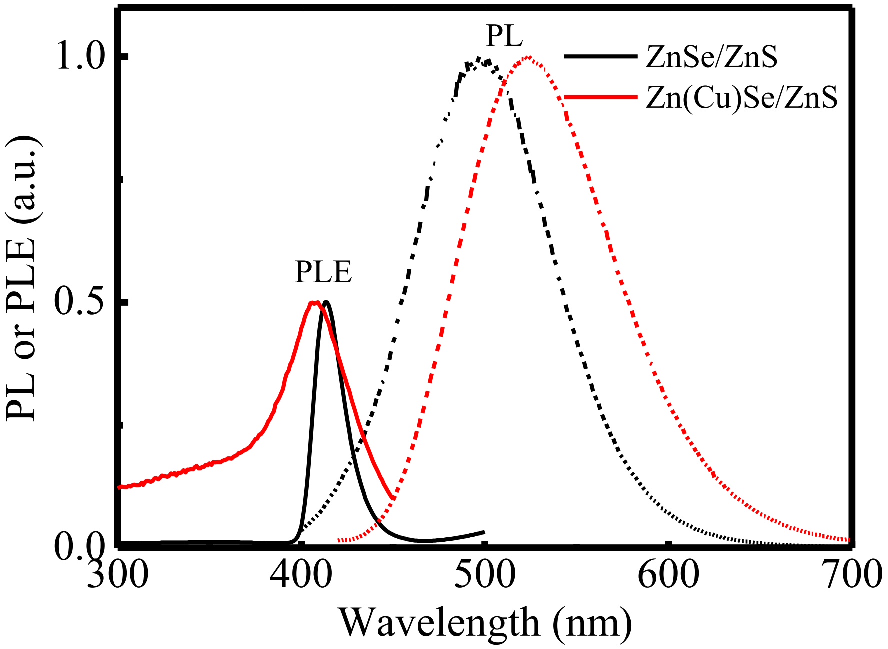

Figure 3.5. One-photon excited PL spectra (dotted lines) and PLE spectra (solid lines) of ZnSe/ZnS QDs (black) and Zn(Cu)Se/ZnS QDs (red) in aqueous solution. The PL spectra were measured with an excitation wavelength of 360 nm, and the PLE spectra were obtained with an emission wavelength of 540 nm.

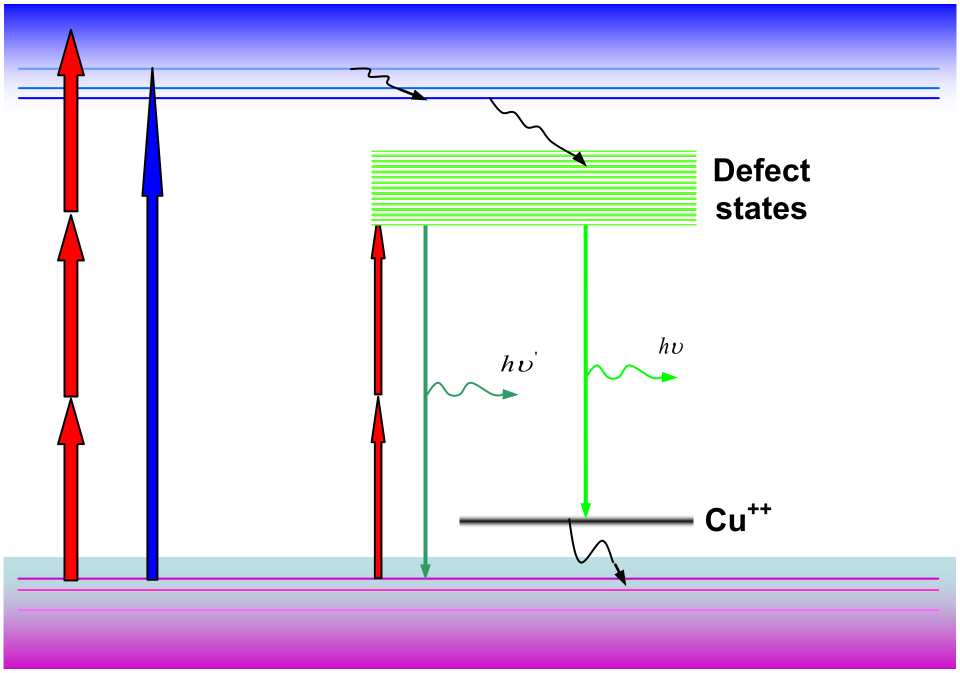

Figure 3.6. Schematic diagram for photodynamics under one-, two-, and three-photon excitation.

3.3 Three-photon absorption and three-photon excited PL

Similar to one-photon excitation, the above photodynamics could also be realized with three-photon processes. In order to determine the 3PA cross-sections, open-aperture Z-scans were employed. The experimental set-up was similar to the standard one [3.14]. The 1000-nm laser pulses were provided by a Coherent Legend (seeded by Mira) pumped TOPAS-C operating at 1 kHz repetition rate, which minimized or eliminated any possible thermal effects. The full-width-at-half-maximum of the laser pulses was 200 fs. The laser pulses were divided into two parts by a beam splitter. The reflected part was taken as the reference. The transmitted part was focused into the sample with a 20 cm focus lens. The sample was moved along the beam propagation axis in vicinity to the focal point with a motor controlled translation stage. As the sample was moved, the reflected and transmitted laser powers were monitored with Laserprobe RKP-465 photodiode. The QD solutions were contained in 1 mm-thick quartz cells for the Z-scans, which were depicted in Figure. 3.6. Following the Z-scan theory for 3PA [3.15], the normalized open-aperture Z-scan transmittance can be express as:

$$T(z) = \frac{1}{\sqrt{\pi}\, p_0} \int_{-\infty}^{\infty} In[\sqrt{1 + p_0^2 \cdot \exp(-2x^2)} + p_0 \exp(-x^2)]dx \tag{3.3}$$

where $p_0 = (2\alpha_3 I_0^2 L_{eff}^{'})^{1/2}$; $L_{eff}^{'} = \frac{(1 - e^{-2\alpha_0 L})}{2\alpha_0}$; $I_0 = I_{00} /(1 + z^2 / z_0^2)$ is the excitation laser intensity at position z; I_{00} is the on axis peak intensity at the focal point; $z_0 = \frac{\pi\omega_0^2}{\lambda}$ is the Rayleigh length; L is the sample length; α_0 is the linear absorption coefficient. If $p_0 < 1$, Eq. (3.3) can be expanded in a Taylor series as:

$$T_{OA} = \sum_{m=1}^{\infty} (-1)^{m-1} \frac{p_0^{2m-2}}{(2m-1)!(2m-1)^{1/2}} \tag{3.4}$$

If the high order terms are ignored:

$$T_{OA} = 1 - \alpha_3 I_0^2 L_{eff}^{'} / 3^{3/2} \tag{3.5}$$

Therefore, we plotted the absorbance (1–T_{OA}) (where T_{OA} is the open-aperture transmittance) as a function of the maximum laser intensity on the Z-axis. The slopes of ~ 2 were indicative of the presence of 3PA. To calibrate our set-up, we also conducted open-aperture Z-scans on ZnSe bulk crystal (Semiconductor Wafer, Inc. 0.9 mm-thick), from which we determined that the 3PA coefficient γ to be 0.044 cm^3/GW^2, which was in the same order of magnitude as the theoretical predication by Brandi *et al*. [3.16] (0.018 cm^3 /GW^2).

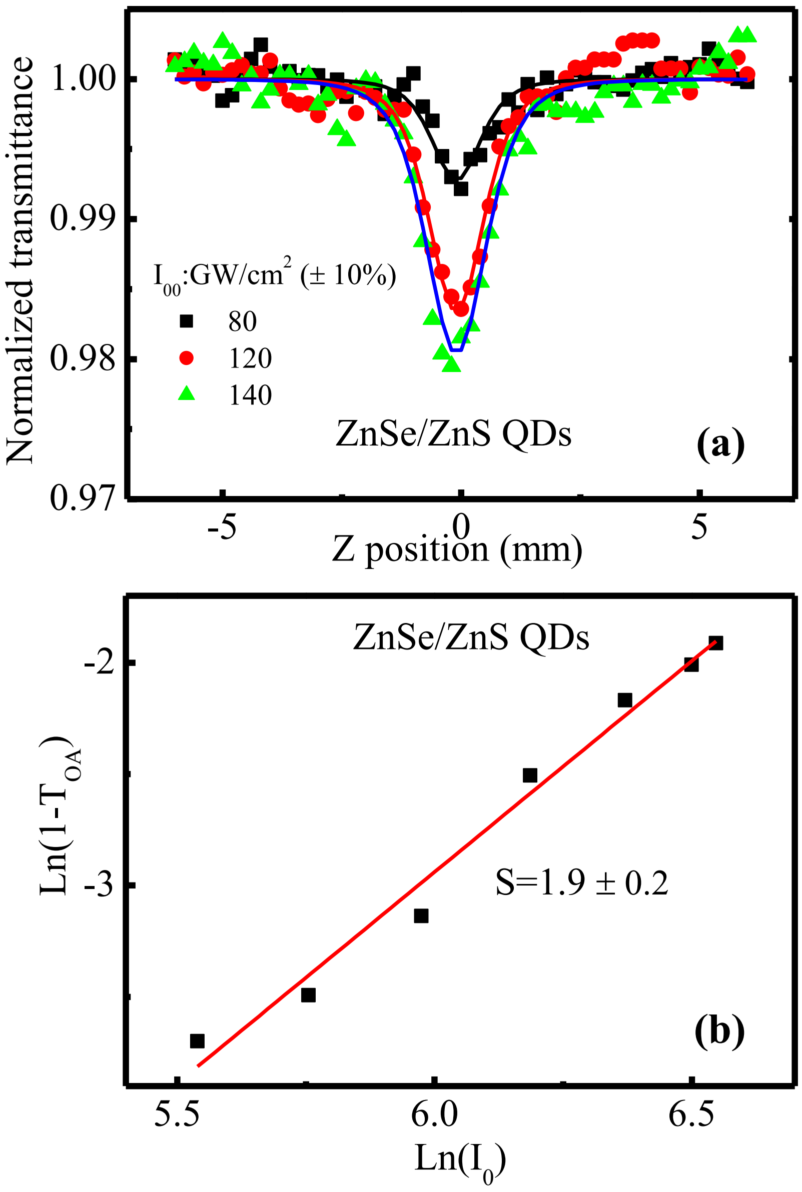

Figure 3.7. (a) Open-aperture Z-scans with 200-fs, 1000-nm laser pulses at different excitation irradiances (I_{00}) for the aqueous solutions of ZnSe/ZnS QDs. The symbols denote the experiment data, while the solid lines are the theoretical curves. (b) The plots of Ln(1$-T_{OA}$) vs. Ln(I_0), and the solid lines represent the linear fits.

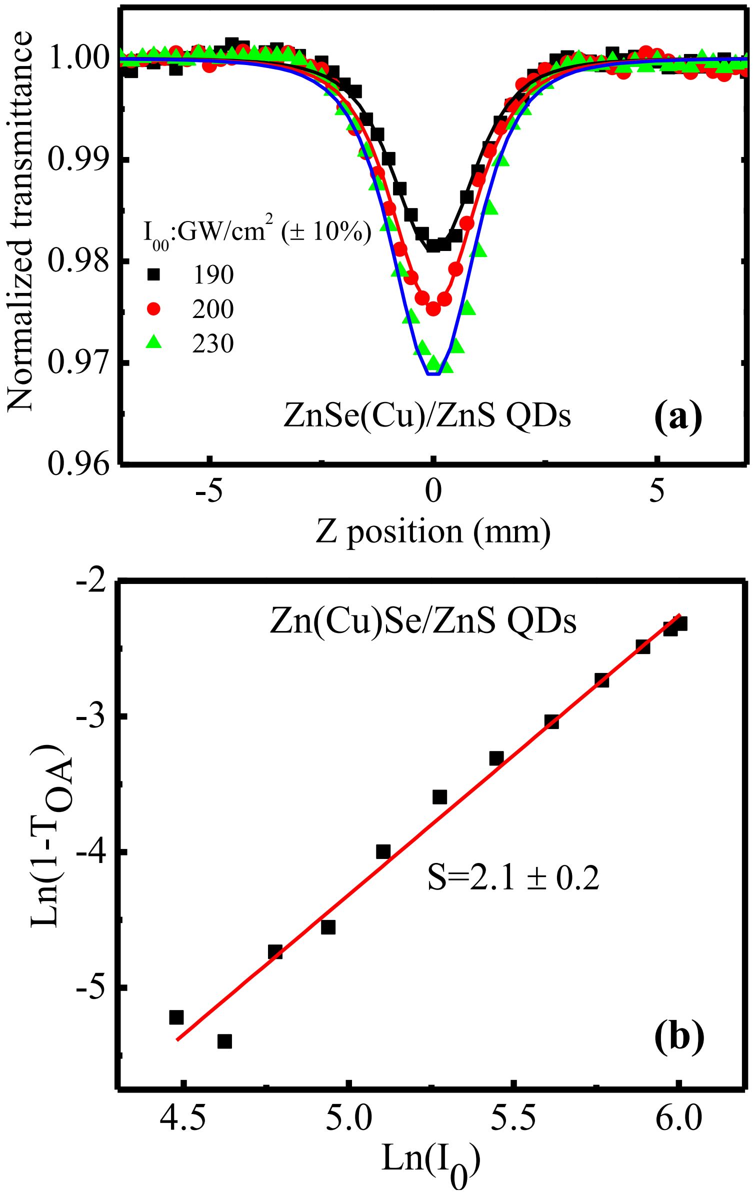

Figure 3.8. (a) Open-aperture Z-scans with 200-fs, 1000-nm laser pulses at different excitation irradiances (I_{00}) for the aqueous solutions of Cu-doped ZnSe/ZnS QDs. The symbols denote the experiment data, while the solid lines are the theoretical curves. (b) The plots of Ln(1–T_{OA}) vs. Ln(I_0), and the solid lines represent the linear fits.

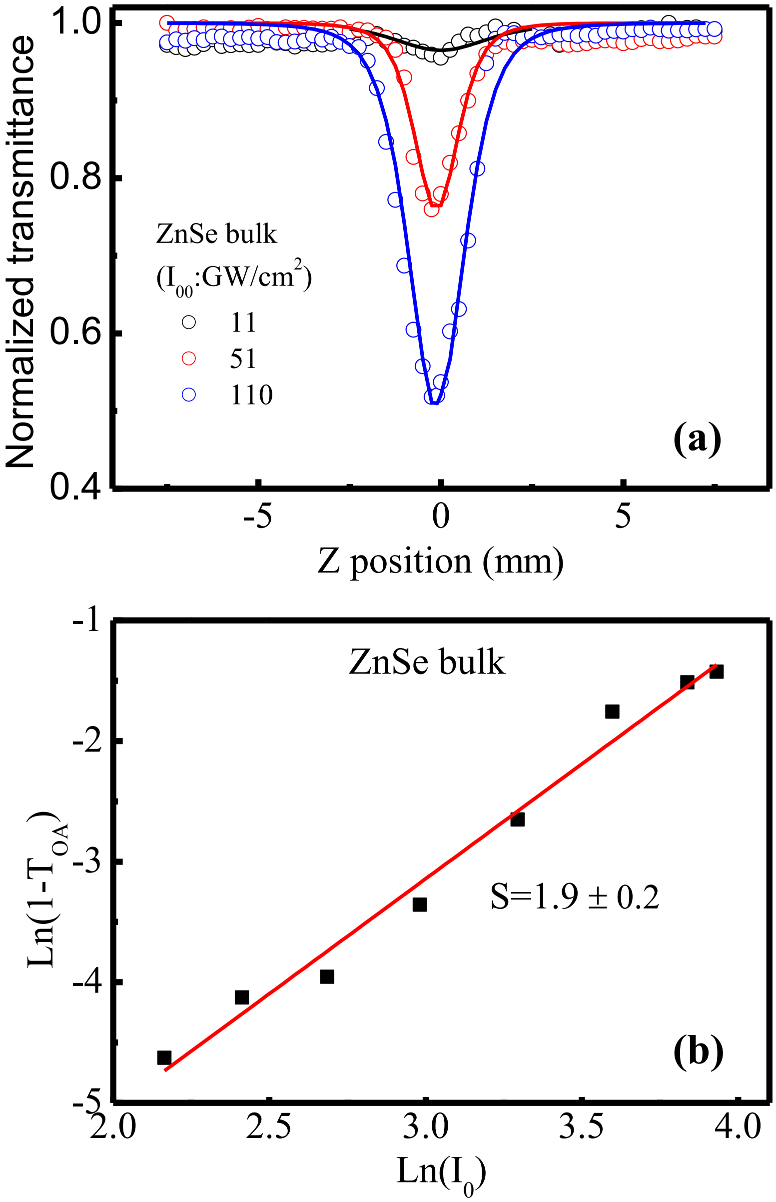

Figure 3.9. (a) Open-aperture Z-scans with 200-fs, 1000-nm laser pulses at different excitation irradiances (I_{00}) for ZnSe bulk crystal. The symbols denote the experiment data, while the solid lines are the theoretical curves. (b) The plots of Ln(1−T_{OA}) vs. Ln(I_0), and the solid lines represent the linear fits.

TABLE 3.2. QD density, diameter, bandgap energy and 3PA of bulk and QD semiconductors.

	Pulse duration (ps)	$N\times10^{17}$ (cm^{-3})	TEM Size (nm)	Band Gap (eV)	γ cm^{3}/GW^{2}	σ_3 (cm^{6}s^{2}/photon^{2})
ZnSe/ZnS QDs	0.2	2.1	4.4	3.03	0.00011	2.0×10^{-77}
Zn(Cu)Se/ZnS QDs	0.2	2.6	4.1	3.14	0.00023	3.5×10^{-77}
Bulk ZnSe (Experiment)	0.2			2.7	0.044	0.78×10^{-79}
Bulk ZnSe (Theory) [3.16]				2.7	0.018	0.32×10^{-79}
ZnSe-I QDs [3.6]	35	4.2	4.5	3.02	0.33	1.2×10^{-75}
ZnSe/ZnS-I QDs [3.6]	35	4.2	4.5	3.02	0.37	1.4×10^{-75}
ZnSe-II QDs [3.6]	35	4.2	3.5	3.25	0.53	2.0×10^{-75}
ZnSe/ZnS-II QDs [3.6]	35	4.2	3.5	3.25	0.63	2.4×10^{-75}
ZnS QDs [3.5]	0.12	1.1	2.5	4.23	0.000045	2.7×10^{-78}
CdSe QDs [3.4]	0.16		2.0-3.9			$\sim10^{-78\,*}$
CdS QDs [3.3]	0.1					$\sim10^{-79}$

* *These values were converted by using* $\sigma_3 = (\hbar\omega)^2\gamma / N$.

The 3PA coefficients are 1.1 × 10^{-4} and 2.3 × 10^{-4} cm^3/GW^2, respectively, for the aqueous solutions of ZnSe/ZnS QDs and Zn(Cu)Se/ZnS QDs. The 3PA cross-sections were then derived as 2.0 × 10^{-77} and 3.5 × 10^{-77} cm^6 s^2 /$photon^2$ from $\sigma_3 = (\hbar\omega)^2 \gamma / N$, where N is the QD density. As shown in Table 1, such values were comparable with the reported values for CdS QDs [3.3], CdSe QDs [3.4] and ZnS QDs [3.5]; however, they were two orders of magnitude smaller than the findings by Lad *et al.* for ZnSe/ZnS QDs [3.6]. It should be pointed out that the measurements of Lad *et al.* were performed with 35-ps laser pulses at an intensity of 6 GW/cm^2. Under their experimental conditions, the electron-hole pairs per QD, $N_{e\text{-}h}/N$, for ZnSe-II QDs might be estimated by

$$\frac{N_{e-h}}{N} = \frac{\gamma}{N} \frac{I_0^3}{3\hbar\omega} \cdot \frac{\tau_G \cdot \sqrt{\pi}}{\sqrt{6}} = 10.5 \tag{3.6}$$

where τ_G is the pulse duration. It was much greater than unity and, hence, the three-photon-excited intraband absorption could become significant in their experiment [3.17]. Under our experimental condition, and using the 3PA coefficients listed in Table 3.2, the three-photon-excited electron-hole pairs per QD were computed to be less than unity. As such, three-photon-excited intraband absorption should be insignificant [3.17].

The three-photon-excited PL measurements were performed at room temperature with the same laser used in the Z-scans. To determine the PL efficiency precisely, a standard sample (Rhodamine 6G, 10^{-4}M in methanol) was measured with the same experimental set-up as described in the following. The incident pulses were focused by a 10× objective lens onto a 1 cm-thick quartz cell containing the QD or Rhodamine 6G solution, and the focal spot size was ~ 9 μm. The PL signal was collected by the same objective lens, refocused by another 10× objective lens, and then coupled into an optical fiber that was connected to a spectrometer (Avaspec-2048-SPU), with 1000-nm excitation wavelength filtered away.

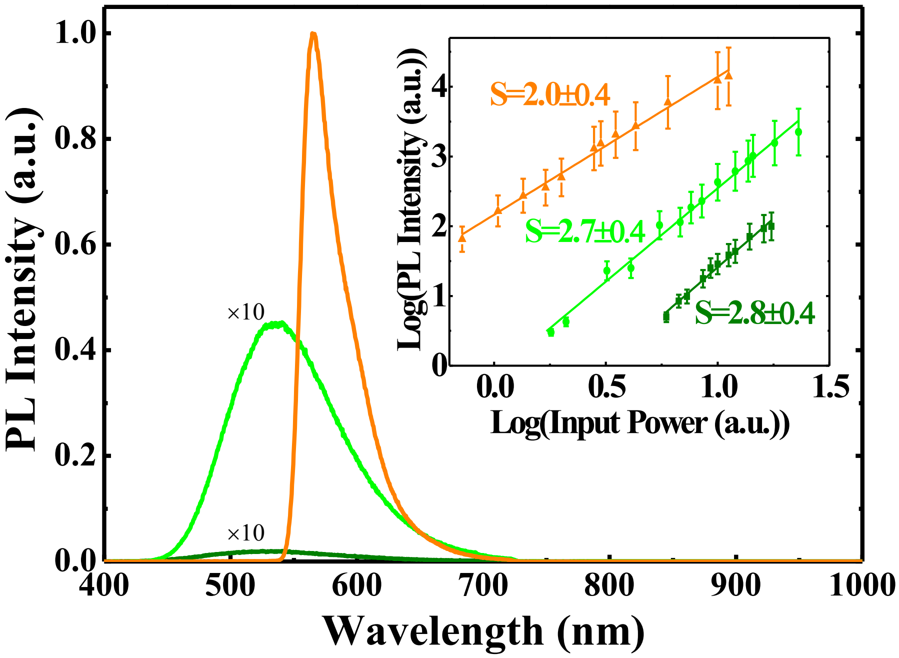

Figure 3.10. Three-photon-excited PL spectra of ZnSe/ZnS (—) and Zn(Cu)Se/ZnS (—) QDs in water are compared with that of Rhodamine 6G in methanol (—). The PL spectra are obtained with 1000-nm excitation wavelength at 77 GW/cm^2. The inset shows log-log plots for the PL signals as a function of the excitation intensity.

As shown by Figure 3.10, band-edge PL of the QDs is entirely quenched, consistent with the one-photon-excited PL discussed previously. It is interesting to note that there is a red-shift between the one- and three-photon excited PL signals (Figure 3.11), in agreement with several reports [3.18-3.20]. The red-shift was more pronounced for the Zn(Cu)Se/ZnS QDs than the undoped ZnSe/ZnS QDs. Due to the weak overlapping of the localized defect states electron wave with the valence band, such defect-state-related emission efficiency was usually very low. The strong green PL from copper-doped QDs was due to transitions from the defect states to the copper ions [3.7].

Inset of Figure 3.10 shows the power dependence of the PL signals on the excitation intensity. Rhodamine 6G clearly possessed a quadratic dependence, indicating that the PL was induced by two-photon absorption (2PA). It was consistent with the observation of Albota *et al.*, who reported the two-photon-excited PL from Rhodamin 6G with femtosecond laser pulses at 960 nm [3.21]. The slopes are 2.8 and ~2.7 for the ZnSe/ZnS QDs and the Zn(Cu)Se/ZnS QDs, respectively. These slopes were different from that measured for CdS QDs by Chon *et al*. [3.3], who observed that the slope was less than 2 for defect-state-related PL excited with laser wavelengths of 900–1000 nm. The slopes of 2.7–2.8 suggested that the two-photon transitions between the defect states and the valence band (or copper ions) played a less important role in ZnSe QDs than CdS QDs [3.3].

To extract the fluorescence quantum efficiency (η_3) of the QDs, one may compare their PL photon counts with Rhodamine 6G under the same excitation intensity. Two- and three-photon excited fluorescence counts (f_2 and f_3) are given by [3.22, 3.23]:

$$f_2 \sim \eta_2 \phi \sigma_2 \rho_1 \cdot ds \cdot dz \cdot I_r^2 \tag{3.7}$$

$$f_3 \sim \eta_3 \phi \sigma_3 \rho_2 \cdot ds \cdot dz \cdot I_r^3 \tag{3.8}$$

where φ is the fluorescence collection efficiency of the experimental set-up; σ_n is the n-photon absorption cross-section; ρ is the sample concentration; $ds \cdot dz$ is the small volume of the focused laser beam considered, and I_r is the nearly-constant laser intensity at this small volume. With the assumption that the temporal and spatial profiles of the laser pulse are Gaussian functions, one can integrate both Eq. (3.7) and Eq. (3.8) over the entire laser-focused volume and time, and obtain their ratio as follows:

$$\frac{F_3}{F_2} = \frac{\sqrt{2}}{3\sqrt{3}} \frac{\eta_3}{\eta_2} \frac{\sigma_3 I_0}{\sigma_2} \frac{\rho_2}{\rho_1} \tag{3.9}$$

For Rhodamine 6G, the quantum efficiency η_2 was known as 0.895 and the 2PA cross-section $\sigma_2 \sim 15\times10^{-48}$ cm^4 s/photon [3.21]. Substituting these two known values into Eq. (3.9), we computed the quantum efficiency to be 27% and 1.4%, for the Zn(Cu)Se/ZnS QDs and the ZnSe/ZnS QDs, respectively, and their 3PA action cross-sections ($\sigma_3\eta_3$) were 9.5×10^{-78} and 2.8×10^{-79} cm^6 s^2 photon^{-2}.

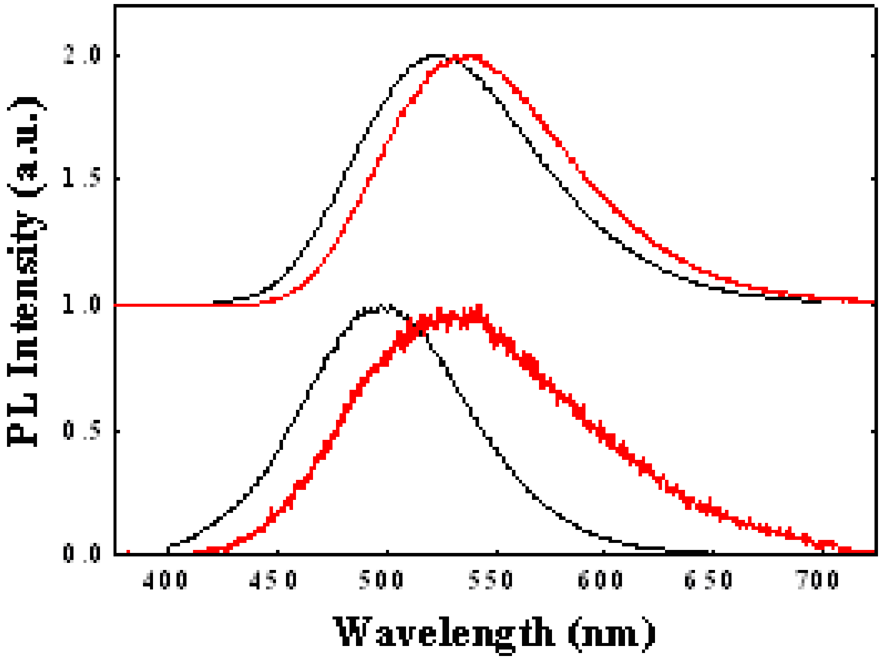

Figure 3.11. One-photon-excited (—) (excitation wavelength = 360 nm) and three-photon-excited (—) (excitation wavelength = 1000 nm) PL spectra of the Zn(Cu)Se/ZnS QDs (top) and ZnSe/ZnS QDs (bottom) in aqueous solution. For comparison purpose, all the spectra are normalized.

3.4 Conclusion

In conclusion, 3PA and three-photon-excited PL of ZnSe/ZnS and Zn(Cu)Se/ZnS QDs in aqueous solutions have been unambiguously determined by Z-scan and PL measurements with femtosecond laser pulses at 1000 nm, which is close to a semi-transparent window for many biological specimens. The 3PA cross-section is as high as 3.5×10^{-77} cm^6 s^2 $photon^{-2}$ for the 4.1-nm-sized, Zn(Cu)Se/ZnS QDs, while their below-band-edge PL has a nearly cubic dependence on excitation intensity, with a quantum efficiency enhanced by ~ 20 fold compared to the undoped ZnSe/ZnS QDs.

References:

[3.1] X. Michalet, F. F. Pinaud, L. A. Bentolila, J. M. Tsay, S. Doose, J. J. Li, G. Sundaresan, A. M. Wu, S. S. Gambhir, and S. Weiss, "Quantum dots for live cells, in vivo imaging, and diagnostics," *Science* **307**, 538 (2005) and references therein.

[3.2] D. R. Larson, W. R. Zipfel, R. M. Williams, S. W. Clark, M. P. Bruchez, F. W. Wise, and W. W. Webb, "Water-soluble quantum dots for multiphoton fluorescence imaging in vivo," *Science* **300**, 1434 (2003) and references therein.

[3.3] J. W. M. Chon, M. Gu, C. Bullen, and P. Mulvaney, "Three-photon excited band edge and trap emission of CdS semiconductor nanocrystals," *Appl. Phys. Lett.* **84**, 4472 (2004).

[3.4] G. S. He, K-T. Yong, Q. Zheng, Y. Sahoo, A. Baev, A. I. Ryasnyanskiy, and P. N. Prasad, "Multi-photon excitation properties of CdSe quantum dots solutions and optical limiting behavior in infrared range," *Opt. Express* **15**, 12818 (2007).

[3.5] J. He, W. Ji, J. Mi, Y. G. Zheng, and J. Y. Ying, "Three-photon absorption in water-soluble ZnS nanocrystals," *Appl. Phys. Lett*. **88**, 181114 (2006).

[3.6] A. D. Lad, P. P. Kiran, G. R. Kumar, and S. Mahamuni, "Three-photon absorption in ZnSe and ZnSe/ZnS quantum dots," *Appl. Phys. Lett.* **90,** 133113 (2007).

[3.7] J. F. Suyver, T. V. D. Beek, S. F. Wuister, J. J. Kelly, and A. Meijerink, "Luminescence of nanocrystalline ZnSe:Cu," *Appl. Phys. Lett*. **79**, 4222 (2001).

[3.8] N. Pradhan, D. Goorskey, J. Thessing, and X. G. Peng, "An alternative of CdSe nanocrystal emitters: pure and tunable impurity emissions in ZnSe nanocrystals," *J. Am. Chem Soc.* **127**, 17586 (2005).

[3.9] B. D. Cullity, Elements of X-ray Diffraction (Addison-Wesley, New York, 1977).

[3.10] V. I. Klimov, "Optical nonlinearities and ultrafast carrier dynamics in semiconductor nanocrystals," *J. Phys. Chem. B* **104**, 6112 (2000).

[3.11] J. B. Li and L. W. Wang, "Band-structure-corrected local density approximation study of semiconductor quantum dots and wires," *Phys. Rev. B* **72**, 125325 (2005).

[3.12] A. A. Khosravi, M. Kundu, L. Jatwa, S. K. Deshpande, U. A. Bhagwat, M. Sastry, and S. K. Kulkarni, "Green luminescence from copper doped zinc sulphide quantum particles," *Appl. Phys. Lett*. **67**, 2702 (1995).

[3.13] N. Pradhan, D. M. Battaglia, Y. Liu, and X. G. Peng, "Efficient, stable, small, and water-soluble doped ZnSe nanocrystal emitters as non-cadmium biomedical labels," *Nano Lett.* **7**, 312 (2007).

[3.14] M. Sheik-Bahae, A. A. Said, T. H. Wei, D. J. Hagan, and E. W. V. Styland, "Sensitive measurement of optical nonlinearities using a single beam," *IEEE J. Quantum Electron.* **26**, 760 (1990).

[3.15] J. He, Y. L. Qu, H. P. Li, J. Mi, and W. Ji, "Three-photon absorption in ZnO and ZnS crystals," *Opt. Express* **13**, 9235 (2005).

[3.16] H. S. Brandi and C. B. D. Araujo, "Multiphoton absorption coefficients in solids: a universal curve," *J. Phys. C* **16**, 5929 (1983).

[3.17] Y. L. Qu, W. Ji, Y. G. Zheng, and J. Y. Ying, "Auger recombination and intraband absorption of two-photon-excited carriers in colloidal CdSe quantum dots," *Appl. Phys. Lett*. **90**, 133112 (2007).

[3.18] W. Z. Wu, Z. R. Zheng, and W. L. Liu, "Upconversion luminescence of CdTe nanocrystals by use of near-infrared femtosecond laser excitation," *Opt. Lett*. **32**, 1174 (2007).

[3.19] T. Franzl, J. Müller, T. A. Klar, A. L. Rogach, J. Feldmann, D. V. Talapin, and H. Weller, "CdSe:Te nanocrystals: band-edge versus Te-related emission," *J. Phys. Chem. C* **111**, 2974 (2007).

[3.20] D. J. Norris and M. G. Bawendi, "Measurement and assignment of the size-dependent optical spectrum in CdSe quantum dots," *Phys. Rev. B* **53**, 16338 (1996).

[3.21] M. A. Albota, C. Xu, and W. W. Webb, "Two-photon fluorescence excitation cross sections of biomolecular probes from 690 to 960 nm," *Appl. Opt*. **37**, 7352 (1998).

[3.22] C. Xu and W. W. Webb, "Measurement of two-photon excitation cross sections of molecular fluorophores with data from 690 to 1050 nm," *J. Opt. Soc. Am. B* **13**, 481 (1996).

[3.23] S. Maiti, J. B. Shear, R. M. Williams, W. R. Zipfel, and W. W. Webb, "Measuring serotonin distribution in live cells with three-photon excitation," *Science* **275**, 530 (1997).

Chapter 4

Two- and three-photon absorption of semiconductor QDs in vicinity of half bandgap

4.1 Introduction

Different mechanisms can produce nonlinear optical effects in a material, in particular, changes in its absorption coefficient. Among the mechanisms responsible for these changes, multiphoton absorption has attracted a great deal of attention because it has potential applications in multiphoton biomedical imaging, optical limiting, etc. [4.1, 4.2]. The multiphoton absorption is a process in which several photons are absorbed simultaneously to excite an electron from a lower state to an upper state in the material. In bulk semiconductors, two-photon absorption (2PA) or three-photon absorption (3PA) would occur in a typical spectral region. In particular, 2PA dominates in the region where photon energies ($\hbar\omega$) are below the band-gap energy (E_g) but greater than $E_g/2$, whereas 3PA manifests itself primarily in the region of $E_g/3 < \hbar\omega \leq E_g/2$. As a result, 2PA or 3PA in bulk crystals can be studied separately in experiments.

This is not the case for an ensemble of semiconductor QDs, for example, a large number of semiconductor QDs is dispersed in a matrix such as glass, film and liquid. Because of inhomogeneous dot sizes, the lowest exciton, $1S_{1/2}(e)\rightarrow 1S_{3/2}(h)$, spreads over a spectral range centered at E_0 with a bandwidth depending on the size dispersion. As photon energies are in the vicinity of $E_0/2$ of QDs, both 2PA and 3PA may both contribute significantly to the observation, giving rise to challenges in precisely determining the respective 2PA and 3PA coefficients. Herein we demonstrate a methodology for the unambiguous determination of 2PA and 3PA of semiconductor QDs in a matrix, in particular, colloidal ZnSe QDs at photon energies in the vicinity of $E_0 / 2$. Recently, colloidal ZnSe QDs have received increasing attention because of their less toxicity in comparison with Cd series of QDs and higher quantum yield of dopant-related PL [4.3-4.5].

4.2 Experiments and discussion

In Chapter 2, the open-aperture Z-scan experiment in which 2PA dominated or 3PA dominated has been discussed. If in a nonlinear system where both 2PA and 3PA contribute equal significantly to measurements such as Z-scans, the wave irradiance equation is described by [4.6]:

$$dI / dz' = -\alpha I - \beta I^2 - \gamma I^3 \tag{4.1}$$

where I is the irradiance; z' is the propagation length; α, β and γ are the small-signal absorption coefficient, 2PA coefficient and 3PA coefficient, respectively. The analytical solution to Eq. (1) for open-aperture Z-scans has been obtained previously [4.7], and is given by:

$$T(z) = \frac{\ln(1+q)}{q} \frac{\ln[(1+p^2)^{1/2} + p]}{p} f(q,p), \tag{4.2}$$

where $f(q,p) = \dfrac{\sum_{n=0}^{5} a_n p^n + q\sum_{n=0}^{5} b_n p^n}{1 + q\sum_{n=0}^{5} c_n p^n}$, $q = q_0/(1+z^2/z_0^2)$, $p = p_0/(1+z^2/z_0^2)$,

$q_0 = \beta I_{00} L_{eff}$, I_{00} is the on-axis maximum intensity at the focus; $L_{eff} = [1-\exp(-\alpha L)]/\alpha$, L is the sample thickness; $p_0 = (2\gamma I_{00}^2 L_{eff}^{'})^{1/2}$, $L_{eff}^{'} = [1-\exp(-2\alpha L)]/2\alpha$, $z_0 = \pi w_0^2/\lambda$, λ is the laser wavelength; w_0 is the beam waist at the focus, and a_n, b_n and c_n are constants whose values have been determined for Gaussian laser pulses[4.7].

Table 4.1. Coefficients a_n, b_n, and c_n when $0 \le p_0 \le \pi$ and $0 \le q_0 \le \pi$ [4.7].

n	a_n	b_n	c_n
0	1.0000	0.4364	0.3036
1	−0.0067	0.0002	0.0268
2	0.1002	0.4143	0.1961
3	−0.0550	−0.3080	−0.1946
4	0.0136	0.0882	0.0636
5	−0.0013	−0.0091	−0.0071

Although there are two unknown parameters (β and γ), they can be determined unambiguously in the following way. At relatively lower irradiances, one can obtain the 2PA coefficient by ignoring 3PA. The 3PA coefficient can then be extracted by fitting Eq. (2) to the measurements at higher irradiances. This analytical method will be applied to distinguish 3PA from 2PA in colloidal ZnSe QDs, described below, at photon energies of

$\hbar\omega \geq E_0 / 2$ where 2PA plays a dominant role. In the case of $\hbar\omega \leq E_0 / 2$, multiphoton-excited photoluminescence (PL) measurements have to be employed in conjunction with open-aperture Z-scans for the unambiguous determination of 2PA and 3PA coefficients.

We demonstrate the above-mentioned method for 2PA and 3PA measurements on high-quality ZnSe/ZnS core-shell colloidal QDs. To enhance the PL quantum yield as well as to manipulate the multiphoton absorption probability, some of the QDs are doped with copper and manganese ions. The synthesis of ZnSe/ZnS QDs and Cu-doped ZnSe/ZnS QDs has been described in Chapter 3. The synthesis of Mn-doped ZnSe/ZnS QDs is briefly described in the following. 10 ml of freshly prepared NaHSe solution (0.02 M) was added into another solution containing 50 ml of 0.01 M $ZnCl_2/MnCl_2$ and GSH at a pH of 11.5 with vigorous stirring. After the injection of NaHSe precursor, 0.3 ml solution of 1 M Na_2S was injected under vigorous solution. The amounts of Zn, Mn, Se, S and GSH introduced were 0.5, 0.005, 0.2, 0.3 and 0.6 mmol, respectively, in a total volume of 50 ml. The resulting mixture was heated to 95ºC, and the growth of GSH-capped QDs began immediately. The final diameter was 4.1 nm on average. In the *d*-QDs, 1% Zn ions in the core were substituted by Mn ions.

The transition-metal-doped QDs are coated with an organic layer of mercaptopropionic acid (MPA), while the un-doped QDs are capped with glutathione (GSH). The synthesis details of these QDs can be found elsewhere [4.5, 4.8, 4.9]. In the doped QDs, 1 mol% of Zn atoms in the core are substituted by Cu^{2+} or Mn^{2+} ions. The transmission electron microscopy (TEM) images in Figure 3.1, Figure 3.2 and Figure 4.1 confirm that the overall particle size including the core, shell and organic coating is ~ 4 nm, and the size dispersion is less than 20%.

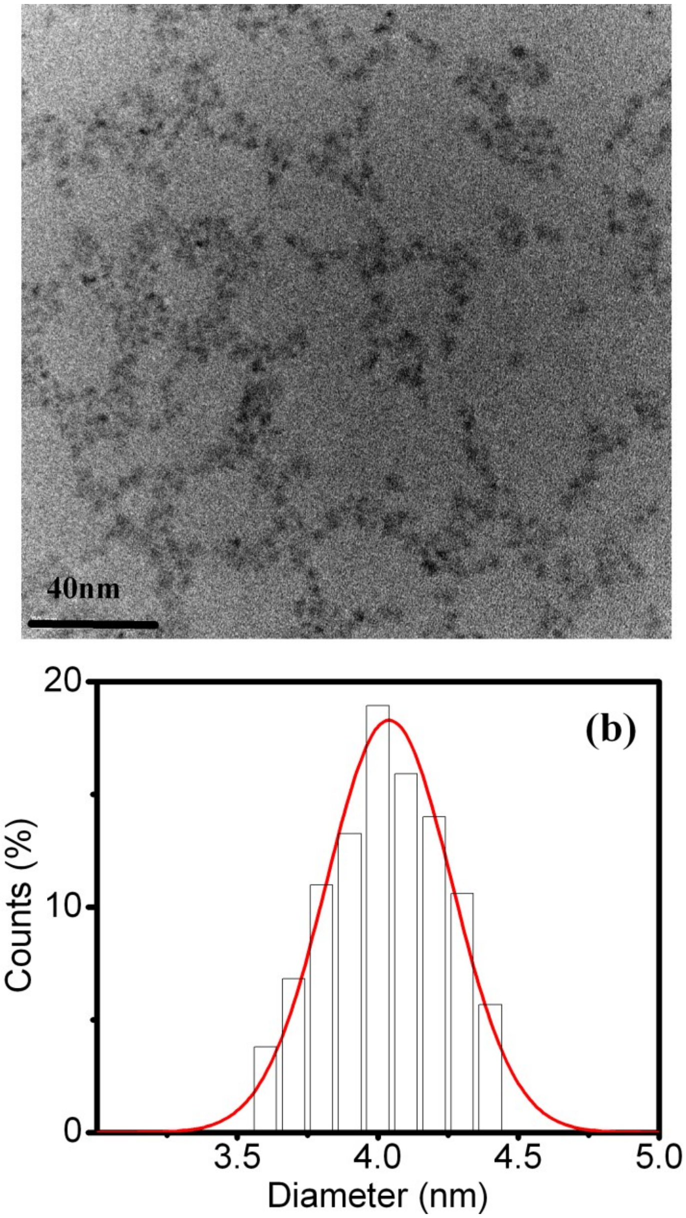

Figure 4.1. (a) TEM images of the Mn-doped ZnSe/ZnS QDs. (b) The size dispersion of the Mn-doped ZnSe/ZnS QDs. The red solid line is a lognormal fit.

As shown in Figure 4.2, the X-ray diffraction (XRD) pattern reveals that these QDs maintain a zinc blend crystal structure. Their UV-visible absorption spectra in Figure 3.4 and Figure 4.3 can be fitted with a series of inhomogeneous broadened Gaussian bands. The three lowest excitons' peak positions are tabulated in Table 4.2. They are 3.2 eV, 3.4 eV and 3.4 eV for pure, Cu-doped and Mn-doped ZnSe/ZnS QDs, respectively. The size dispersions are estimated to be around ~10% for all the samples. Note that the doped QDs presented here are different in structure from heavily Mn-doped ZnSe QDs reported by Gan *et al.* [4.3], which had a MnSe core, an outer ZnSe layer and a $Zn_{1-x}Mn_xSe$ diffusion layer in between.

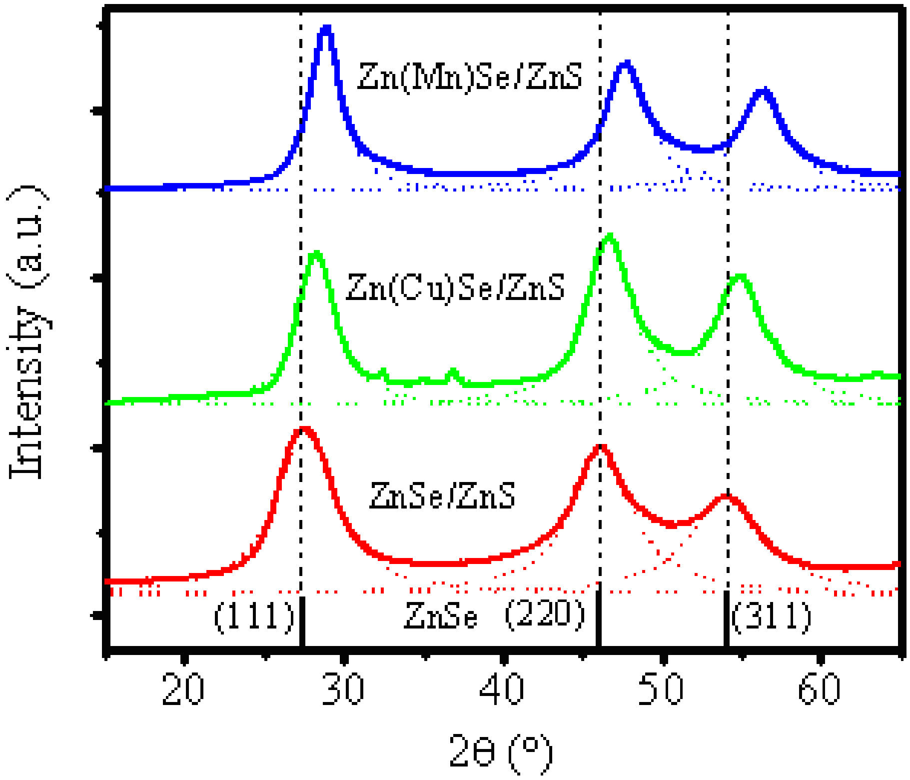

Figure 4.2. XRD patterns of un-doped (**red** line), Cu-doped (**green** line) and Mn-doped (**blue** line) ZnSe/ZnS QDs. The dotted lines are the fits with Lorentzian curves.

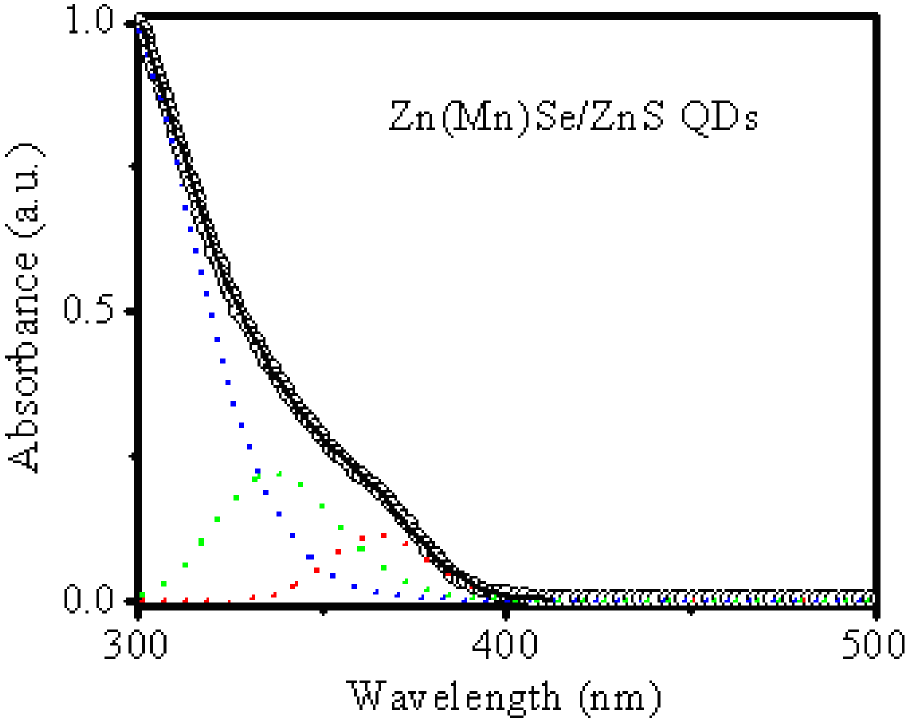

Figure 4.3. Optical absorption spectra of Mn-doped ZnSe/ZnS QDs fitted to three Gaussian bands.

Table 4.2. The Gaussian fitted lowest band, second band, third band and size distribution of un-doped and Cu-doped and Mn-doped ZnSe/ZnS QDs.

	Lowest band (ev)	Second band (ev)	Third band (ev)	Δ_R/R
ZnSe/ZnS	3.2	3.6	4.3	12.2%
Zn(Cu)Se/ZnS	3.4	3.7	4.2	9%
Zn(Mn)Se/ZnS	3.4	3.7	4.2	9%

As shown in Figure 4.4, the band-edge emission of the ZnSe core is completely quenched, regardless of single- or multiphoton excitation. The trapping-state-related emission in the un-doped QDs is centered at 498 nm, while the emission from Cu^{2+} and Mn^{2+} ions in the doped QDs is peaked at 520 and 590 nm, respectively. The broad PL peak at 520 nm for the Cu-doped QDs has been attributed to the recombination between an excited electron and the hole from the *d*-orbital of a Cu^{2+} ion [4.10]. The broad emission at 590 nm from the Mn-doped QDs has been assigned to the $^4T_1 \rightarrow {}^6A_1$ transitions of Mn^{2+} ions [4.11]. The quantum yields (η_{QD}) are determined to be ~1.4%, 22%, and 27%, respectively, for the un-doped, Mn-doped, and Cu-doped QDs.

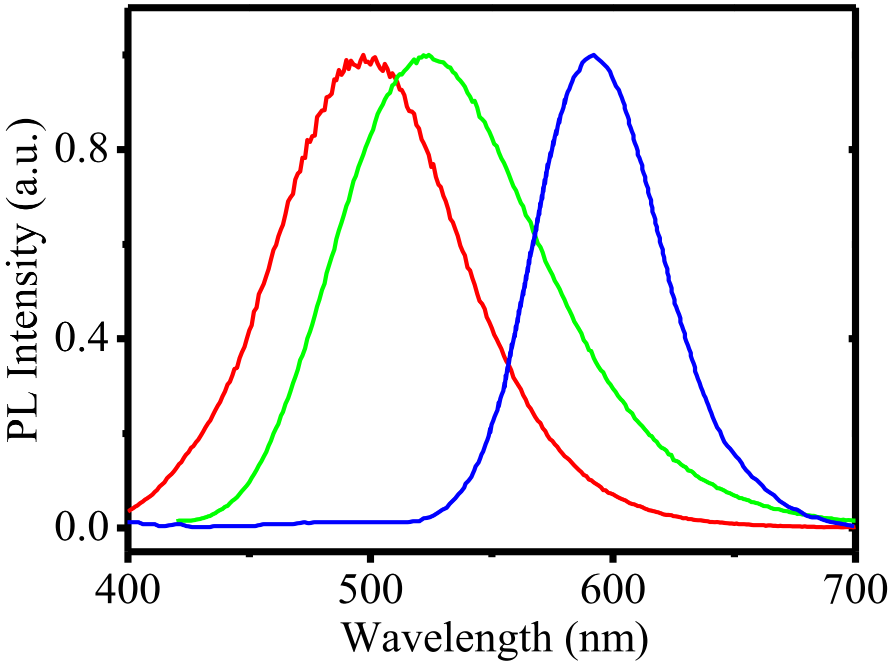

Figure 4.4. PL spectra excited at 360 nm (solid lines) for un-doped (**red**), Cu-doped (**green**), and Mn-doped (**blue**) ZnSe/ZnS QDs. All spectra are normalized for comparison.

The above-mentioned QDs have been dispersed in water and contained in 1 mm-thick quartz cells for open-aperture Z-scans with femtosecond laser pulses. The details of the open-aperture Z-scans have been described in Chapter 2 and 3 [4.5]. It should be emphasized that all the Z-scans were conducted with laser irradiances below the damage thresholds; this was assured by the same absorption and/or PL spectra measured before and after the femtosecond laser radiation. Here we clarify that the capping agent (GSH or MPA) dispersed in water was Z-scanned under the same set-up with laser intensities up to 400 GW/cm^2. As shown in Figure 4.5 below, GSH or MPA in water solution show transparent and colorless, indicating no absorption in the visible range. In the Z-scans, the same concentration of MPA (10mg/ml), or GSH (25mg/mL) as those in the QD solutions were used.

Figure 4.5. Photo images of 10 mg/mL MPA and 25 mg/mL GSH in water solution.

Figures 4.6 (a) and (b) below show the Z-scans of MPA and GSH solution conducted with 800-nm, 410 GW/cm^2 laser pulses, which demonstrate that their nonlinear absorption contributions are negligible, within the experimental errors.

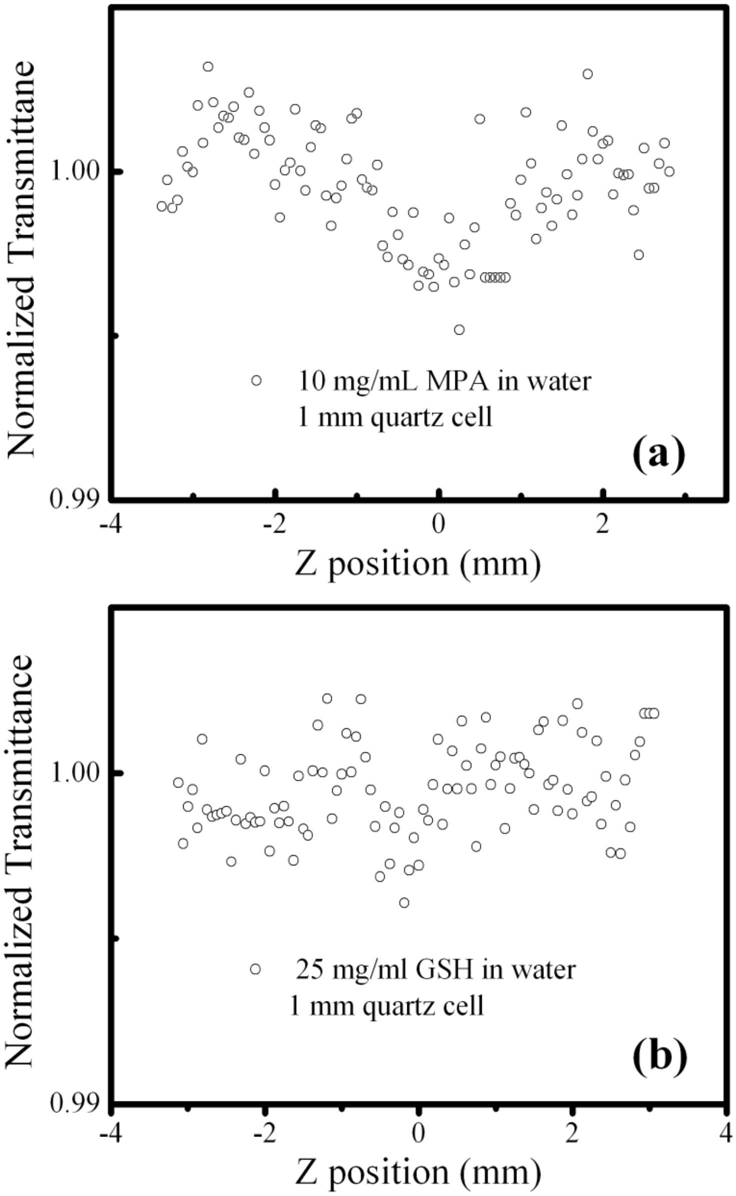

Figure 4.6. Open-aperture Z-scan of (a) MPA and (b) GSH in water solution under the excitation of 410 GW/cm^2 at 800 nm.

Typical Z-scans with 700 nm (1.77 eV ≥ $E_0/2$ ~ 1.7 eV) laser pulses excitation are illustrated in Figure 4.7(a), 4.8(a) and 4.9(a) for un-doped, Cu-doped and Mn-doped ZnSe/ZnS QDs, respectively. If we assume that the 3PA coefficient is zero, the effective 2PA coefficients extracted from fitting Eq. (4.2) to the Z-scans at 700 nm are linearly dependent on the irradiance (see Figure 4.7(b), 4.8(b) and 4.9(b)). It clearly demonstrates that other nonlinear processes can not be ignored, although the photon energy involved here is in the region of $\hbar\omega \geq E_0/2$. This linear dependence can not be explained by 2PA-induced intraband absorption because the 2PA-excited electron-hole pairs are less than unity per QD under our experimental condition [4.12]. From Eq.(4.1), the effective 2PA coefficient is derived to be $\beta^{eff} = \beta + \gamma I$, which is indicative of the linear dependence on the irradiance. The β value can be determined unambiguously from the intercept of the linear line on the vertical axis in Figure 4.7(b), 4.8(b) and 4.9(b). The 2PA cross-section, σ_2, can then be obtained from $\sigma_2 = \beta\hbar\omega / N_{QD}$, where N_{QD} is the concentration of QDs. With the determined 2PA coefficient, the 3PA coefficient is extracted from fitting Eq.(4.2) to the Z-scan. Correspondingly, the 3PA cross-section (σ_3) is calculated by $\sigma_3 = (\hbar\omega)^2 \gamma / N_{QD}$.

In 2PA and 3PA coupled system, the lower of pump power, the larger contribution of 2PA. Therefore, the effective 2PA coefficient is closer to the intrinsic 2PA coefficient when the pump power is decreased. The 2PA coefficient can be determined from the intercept of the linear effective 2PA line on the vertical axis (extremely low pump power). However, the effective 2PA fittings were not good because the 3PA contribution was neglected (see Figs. 4.7 – 4.9). The discrepancy between the fitting curves and experimental data is increased with pump power. If the 3PA coefficients are extracted from the slope of the linear effective 2PA coefficient lines, they are 3×10^{-5}, 5×10^{-5} and 9×10^{-5} cm^3/GW^2, respectively, for the un-doped, Cu-doped and Mn-doped QDs. These data are slightly lower than that obtained from the theoretical fittings based on 2PA and 3PA coupled theory (5×10^{-5}, 12×10^{-5} and 13×10^{-5} cm^3/GW^2). However, the discrepancy is within the experimental uncertainties.

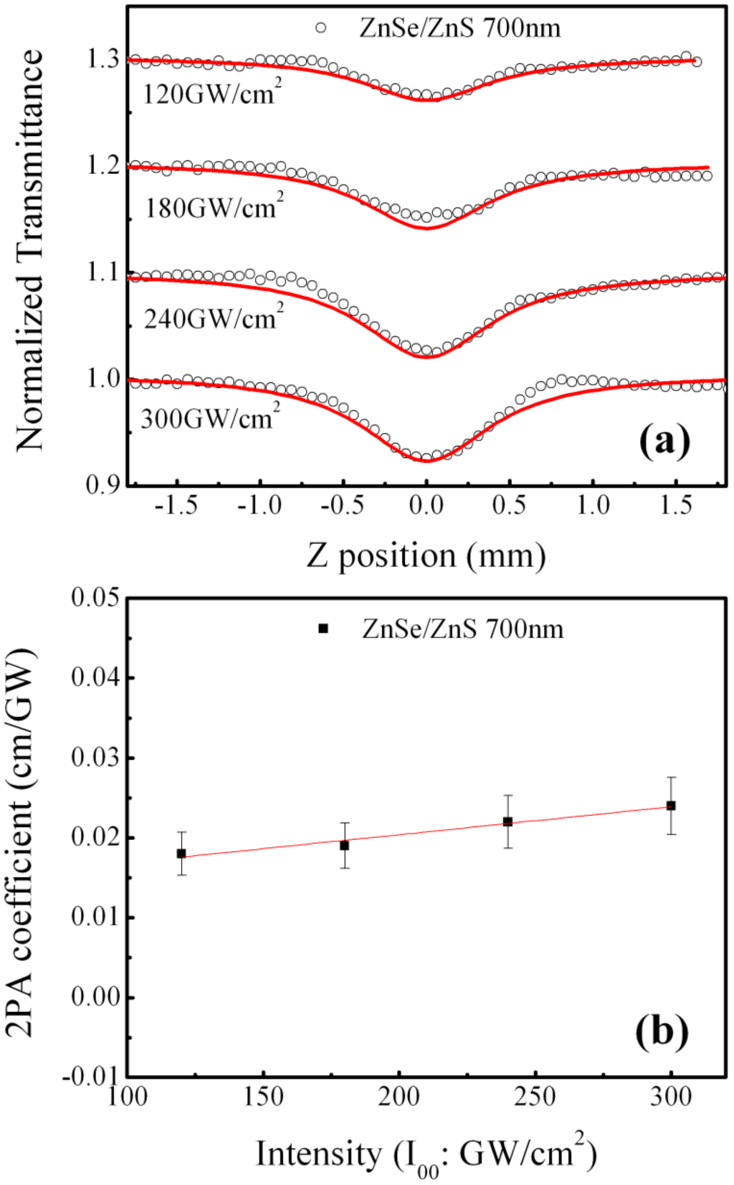

Figure 4.7. (a) Open-aperture Z-scans on ZnSe/ZnS QDs measured at 700 nm. (b) Effective 2PA coefficient.

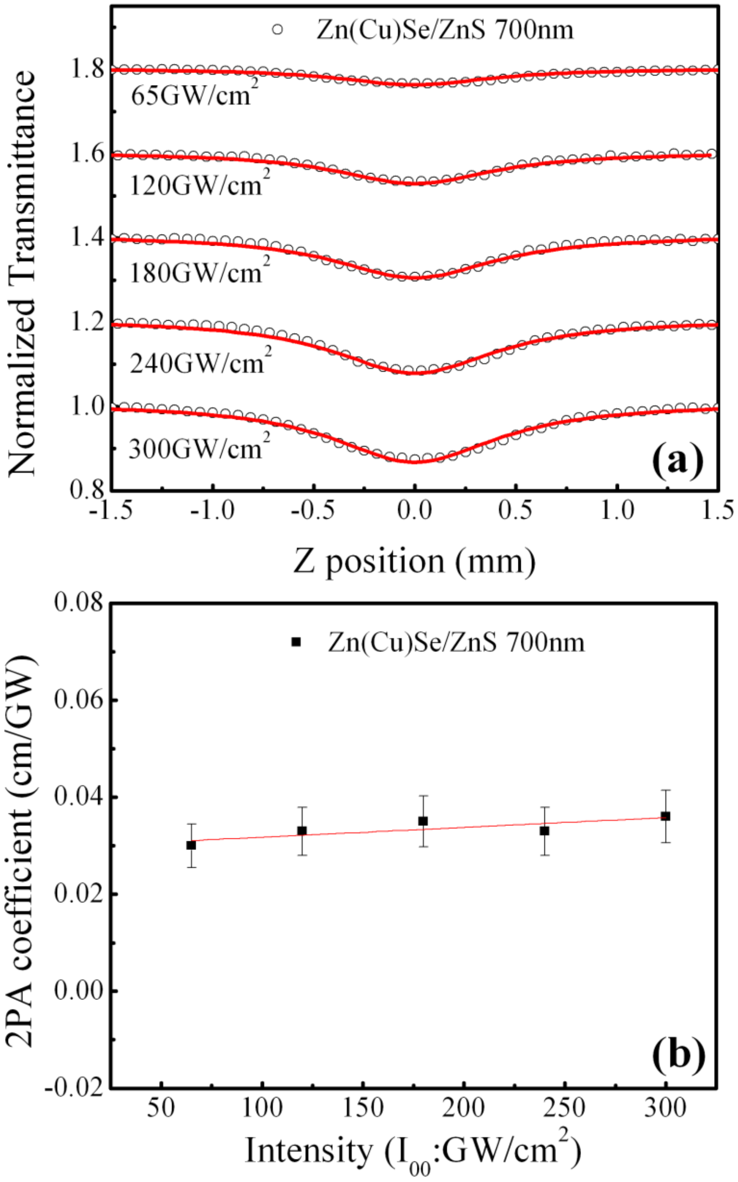

Figure 4.8. (a) Open-aperture Z-scans on Cu-doped ZnSe/ZnS QDs measured at 700 nm. (b) Effective 2PA coefficient.

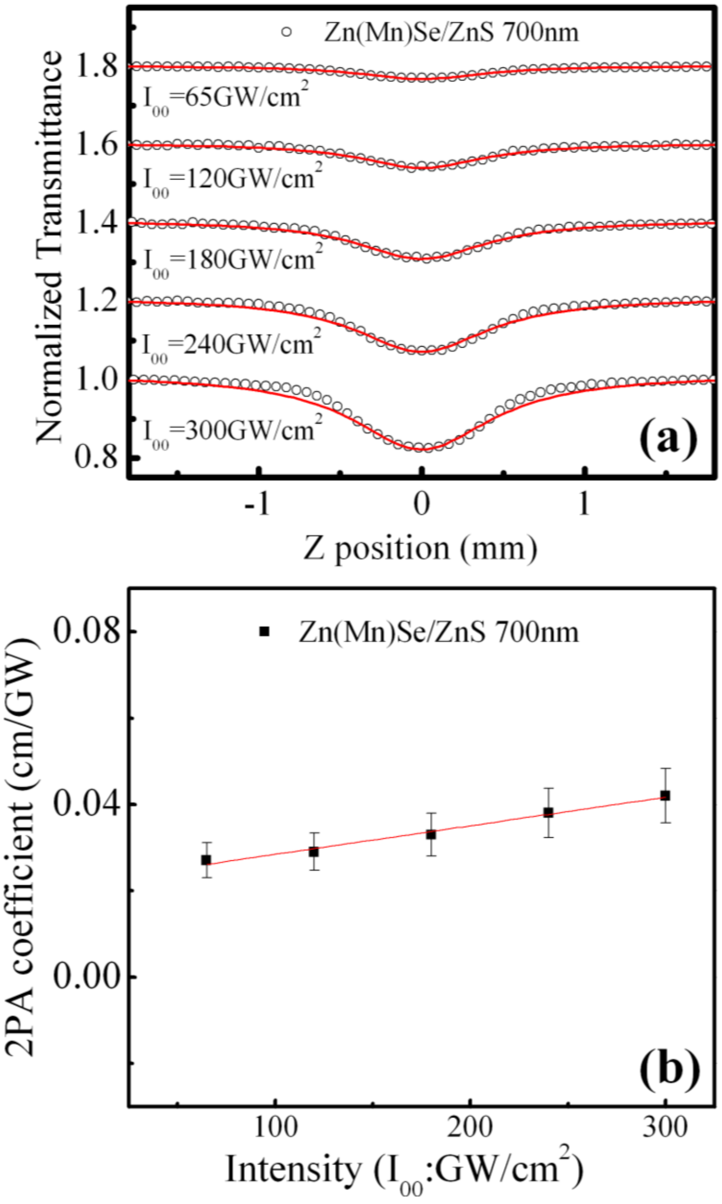

Figure 4.9. (a) Open-aperture Z-scans on Mn-doped ZnSe/ZnS QDs measured at 700 nm. (b) Effective 2PA coefficient.

As the laser wavelength is tuned to 800 nm (1.55 eV ≤ $E_0/2$ ~ 1.7 eV), it is expected that 3PA should play a dominant role in the Z-scans because the photon energy is less than $E_0/2$. If β is set as zero, the best fits between Eq. (4.2) and the Z-scans generate the effective 3PA coefficients. Figure 4.10(b), 4.11(b) and 4.12(b) show that the effective 3PA coefficients are independent of the laser irradiance within the experimental uncertainty, implying the insignificance of 2PA. It should be pointed out that this finding is obtained in the high-irradiance regime (100 GW/cm^2 or higher). However, it can not rule out the 2PA contribution to multiphoton-excited PL measurements at lower laser irradiances, as shown below.

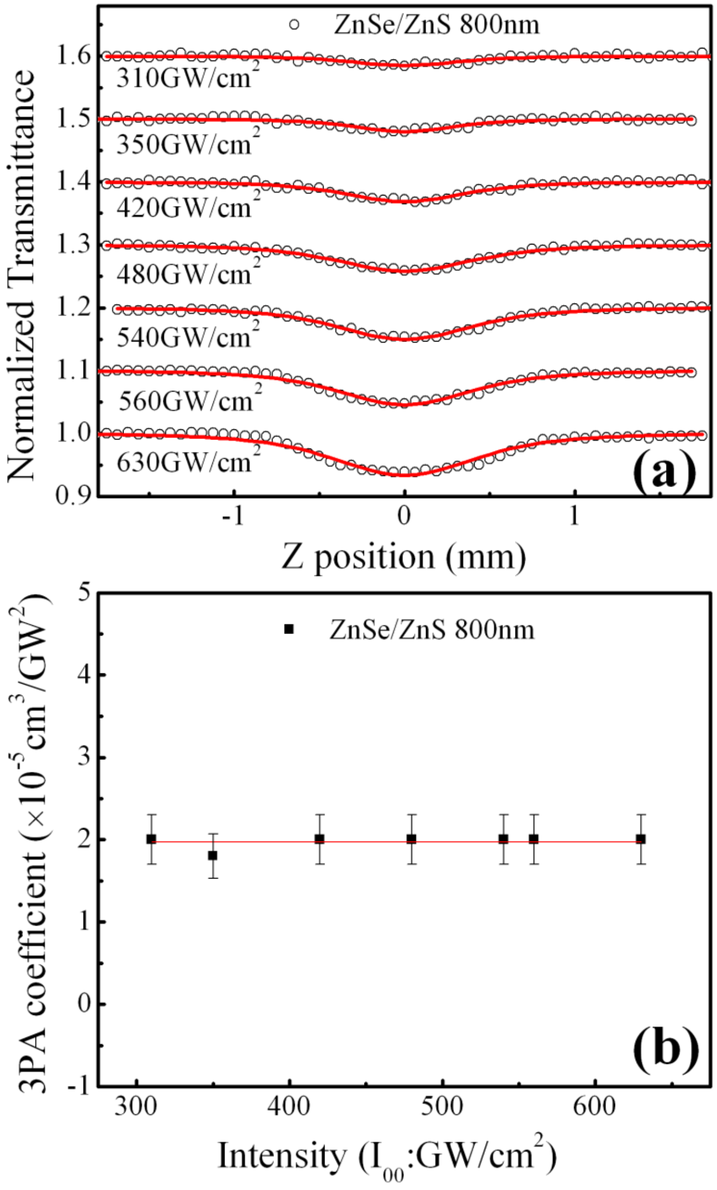

Figure 4.10. (a) Open-aperture Z-scans on ZnSe/ZnS QDs measured at 800 nm. (b) Effective 3PA coefficient.

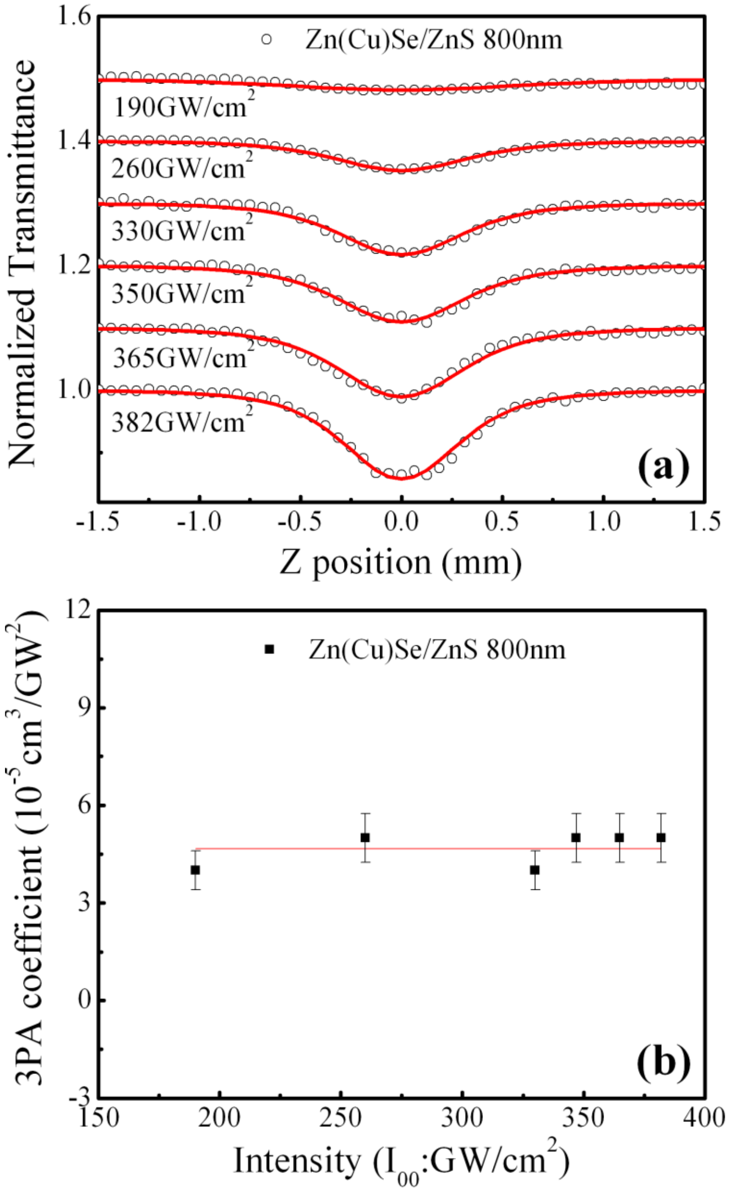

Figure 4.11. (a) Open-aperture Z-scans on Cu-doped ZnSe/ZnS QDs measured at 800 nm. (b) Effective 3PA coefficient.

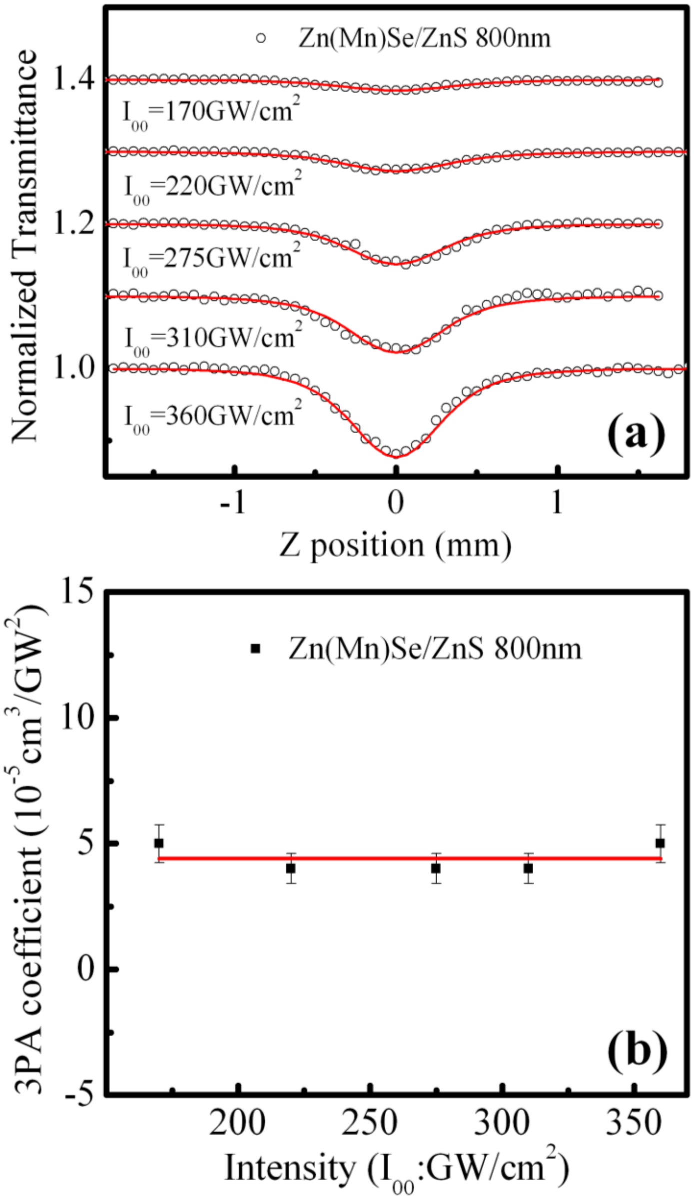

Figure 4.12. (a) Open-aperture Z-scans on Mn-doped ZnSe/ZnS QDs measured at 800 nm. (b) Effective 3PA coefficient.

In our multiphoton-excited PL measurement, the excitation source was a femtosecond Ti:Sapphire oscillator (Spectra Physics, Tsunami, pulse duration = 40 fs, repetition rate = 76 MHz and center wavelength = 800 nm). The laser pulses were focused by a lens (f = 15 cm) on the QD solution in a 1-cm-thick quartz cell, with a focal spot size of ~ 20 μm inside the cell. The emission from the QDs was collected at an angle of 90° by a pair of lenses and optical fibers, and directed to a spectrometer (Acton, Spectra Pro 2300i coupled CCD Princeton Instruments, Pixis 100B). A short-pass filter with a cut-off wavelength of 730 nm was placed before the spectrometer to minimize the scattered excitation light.

Figure 4.13(b) depicts the quadratic power dependence for all the PL signals. The quadratic power dependence might have resulted from 2PA or Auger recombination. Under relatively low excitation irradiances of 2 GW/cm^2 or less, the average electron-hole pairs generated by 2PA are calculated to be much less than unity per QD. As such, Auger recombination is insignificant. To precisely determine the 2PA cross-section, a standard sample (Rhodamine 6G, 10^{-4} M in methanol) has been measured under the same experimental conditions. For Rhodamine 6G (R6G), the PL quantum yield, η_{R6G} and the 2PA cross-section, σ_2^{R6G} are known to be 0.95 and 2×10^{-48} cm^4 s/photon at 800 nm, respectively [4.13]. With these two known values, the 2PA cross-section of the QDs is determined by utilizing the ratio of PL signal from the QDs to R6G, $\sigma_2^{QD} N_{QD} \eta_{QD} / (\sigma_2^{R6G} N_{R6G} \eta_{R6G})$, where N_{R6G} is the concentrations of R6G.

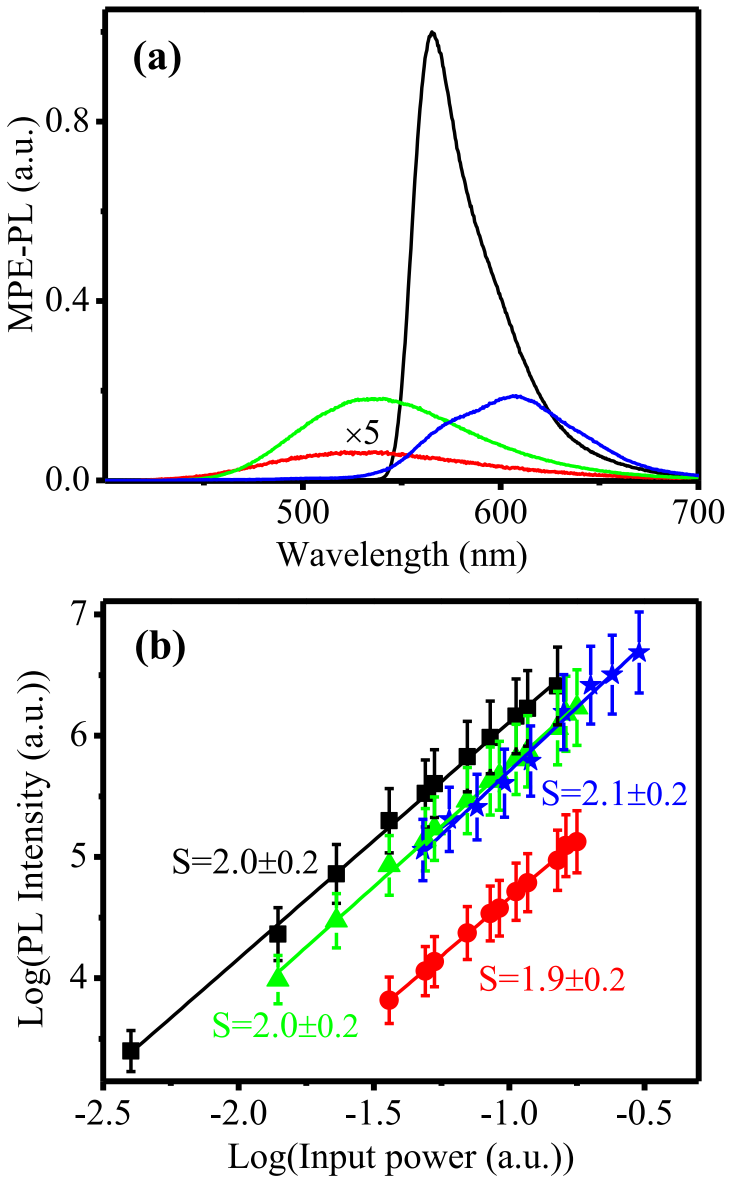

Figure 4.13. (a) PL spectra measured with 40-fs, 800-nm laser pulses for un-doped (**red**), Cu-doped (**green**), and Mn-doped (**blue**) ZnSe/ZnS QDs. Rhodamine 6G (10^{-4} M in methanol, **black**) is used as a reference. (b) The measured PL signals as a function of excitation power and the best-fit straight lines.

The 2PA coefficients are inferred from $\beta = \sigma_2 N_{QD} / \hbar\omega$. With the known 2PA coefficient, the intrinsic 3PA coefficient is unambiguously determined by fitting Eq. (4.2) to the Z-scans at 800 nm. The intrinsic 3PA coefficients are the same as the effective 3PA coefficients within the experimental error. The red line in Figure 4.14(a) shows that the magnitude of 2PA is less than 0.5% in the normalized transmittance, and hence, it explains why 2PA is insignificant in the Z-scans. It should be pointed out that the contribution from 2PA or 3PA is dependent on the excitation irradiance. At relatively lower irradiances (< 2 GW/cm^2), the ratio of 3PA- to 2PA-excited PL is $\sigma_3 I / \sigma_2 < 0.1$, which suggests that 3PA is negligible. Figure 4.14(b) illustrates the dominance of three-photon-excited PL over two-photon-excited PL in the red region where $\sigma_3 I / \sigma_2 > 5$. We have also conducted the Z-scan and PL measurement with an excitation wavelength of 1000 nm, which is far away from $E_0 / 2$ [4.5]. The Z-scans and PL spectra clearly verified that the 2PA signals were too small to be detectable, as anticipated. Recently, *Lad et al*. [4.4] measured the 2PA cross-sections to be on the order of 10^{-47} cm^4 s photon^{-1}, for ZnSe QDs or ZnSe/ZnS QDs in 4.3-nm size, without considering the contribution from 3PA. If we use $\sigma_2^{eff} = \sigma_2 + \sigma_3 I / (\hbar\omega)$ to calculate the effective 2PA cross-sections from our experiments for the un-doped QDs at 700 nm and ~100 GW/cm^2, we obtain $\sigma_2^{eff} \approx 1 \times 10^{-47}$ cm^4 s photon^{-1}, the same order of magnitude as theirs.

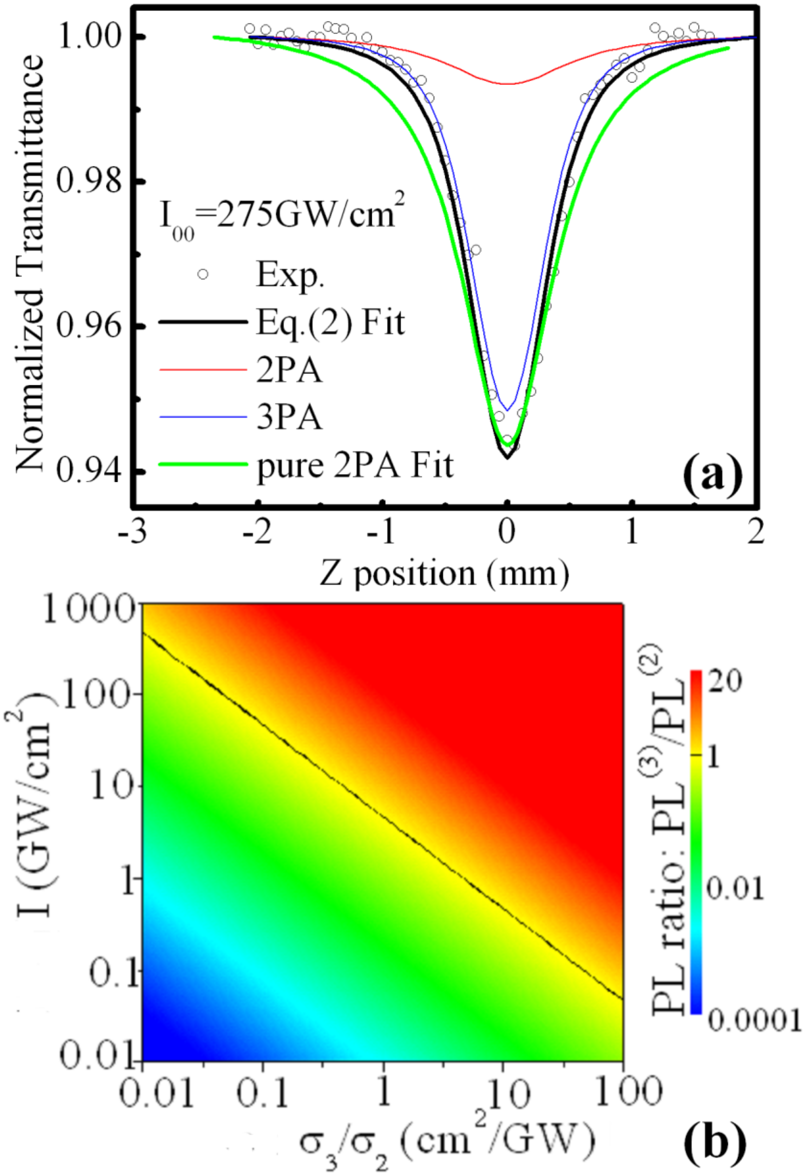

Figure 4.14. (a) Typical Z-scans on Mn-doped ZnSe/ZnS QDs at 800 nm, fitted with Eq. (2) for pure 2PA effect ($\gamma = 0$, **green**) and both effects ($\beta \neq 0$ and $\gamma \neq 0$, **black**). (**b**) Ratio of three-photon-excited to two-photon-excited PL plotted as a function of I and σ_3 / σ_2.

Table 4.3. Exciton positions, 2PA and 3PA cross-sections.

Samples		ZnSe/ZnS	Cu-doped ZnSe/ZnS	Mn-doped ZnSe/ZnS
Peak Position of $1S_{1/2}(e)\rightarrow 1S_{3/2}(h)$		3.2 eV	3.4 eV	3.4 eV
λ = 700 nm	σ_2 (cm^4 s photon^{-1})	2.7×10^{-48}	14×10^{-48}	9.3×10^{-48}
	σ_3 (cm^6 s^2 photon^{-2})	1.9×10^{-77}	3.7×10^{-77}	4.0×10^{-77}
λ = 800 nm	σ_2 (cm^4 s photon^{-1})	1.4×10^{-49}	7.2×10^{-49}	7.0×10^{-49}
	σ_3 (cm^6 s^2 photon^{-2})	3.1×10^{-78}	5.5×10^{-78}	4.9×10^{-78}

Experimental uncertainly: ±50%. Size dispersion of QDs: ≤ 20%.

Recent theoretical calculations for 2PA in CdSe QDs and CdTe QDs are in agreement with experiments [4.14, 4.15]. By applying the four-band model [4.14], we have calculated that the change in the 2PA of ZnSe QD is less than 20% if the dot size decreases from 4.4 to 4.1 nm, which is undetectable in view of our experimental uncertainty of 50%. As shown in Table 4.3, the 2PA cross-sections in the doped QDs are enhanced by ~5 times by comparing with the un-doped QDs. Such an enhancement partially originates from the introduction of metal-ion states in the doped QDs. Furthermore, the enhancement also partially results from enhanced trap states due to the distortion in ZnSe crystal structure by presence of impurities [4.10]. The four-band model predicts that there is a decrease of ~30% in the 3PA cross-section of ZnSe QDs as their sizes are reduced from 4.4 to 4.1 nm [4.16]. Such a size dependence is too small to be detectable. In comparison to the un-doped ZnSe QDs, the large 3PA cross-section in the transition-metal-doped ZnSe QDs is attributed to the degeneracy between two-photon transitions to the states of metal ions in the bandgap and three-photon transitions to the excitonic states [4.16].

4.3 Conclusion

In conclusion, we have demonstrated that the 2PA and 3PA coefficients of semiconductor QDs in a matrix can be unambiguously determined at photon energies in the vicinity of $E_0/2$. In the spectral region where the photon energy is greater than but near $E_0/2$, the 2PA coefficient is determined by open-aperture Z-scans at relatively lower irradiances, and the 3PA coefficient is then extracted from open-aperture Z-scans conducted at higher irradiances. At photon energies below but close to $E_0/2$, both open-aperture Z-scans and multiphoton-excited PL measurements have to be employed to distinguish between 2PA and 3PA.

References:

[4.1] X. Michalet, F. F. Pinaud, L. A. Bentolila, J. M. Tsay, S. Doose, J. J. Li, G. Sundaresan, A. M. Wu, S. S. Gambhir, and S. Weiss, “Quantum dots for live cells, in vivo imaging, and diagnostics,” *Science* **307**, 538 (2005) and references therein.

[4.2] G. S. He, K-T. Yong, Q. Zheng, Y. Sahoo, A. Baev, A. I. Ryasnyanskiy, and P. N. Prasad, “Multi-photon excitation properties of CdSe quantum dots solutions and optical limiting behavior in infrared range,” *Opt. Express* **15**, 12818 (2007) and references therein.

[4.3] C. Gan, M. Xiao, D. Battaglia, N. Pradhan, and X. Peng, “Size dependence of nonlinear optical absorption and refraction of Mn-doped ZnSe nanocrystals,” *Appl. Phys. Lett.* **91**, 201103 (2008).

[4.4] A. D. Lad, P. P. Kiran, D. More, G. R. Kumar, and S. Mahamuni, “Two-photon absorption in ZnSe and ZnSe/ZnS core/shell quantum structures,” *Appl. Phys. Lett*. **92**, 043126 (2008).

[4.5] G. Xing, W. Ji, Y. Zheng, and J. Y. Ying, “High efficiency and nearly cubic power dependence of below-band-edge photoluminescence in water-soluble, copper-doped ZnSe/ZnS quantum dots,” *Opt. Express* **16**, 5710 (2008).

[4.6] M. Sheik-Bahae, A. A. Said, T. H. Wei, D. J. Hagan, and E. W. van Styland, “Sensitive measurement of optical nonlinearities using a single beam,” *IEEE J. Quantum Electron.* **26**, 760 (1990).

[4.7] B. Gu, W. Ji, P. S. Patil, S. M. Dharmaprakash, and H. T. Wang, “Two-photon-induced excited-state absorption: theory and experiment,” *Appl. Phys. Lett*. **92**, 091118 (2008).

[4.8] Y. Zheng, Z. Yang, Y. Li, and J. Y. Ying, "From glutathione capping to a crosslinked, phytochelatin-like coating of quantum dots," *Adv. Mater.* **20**, 3410 (2008).

[4.9] Y. Zheng, Y. Li, J. Jiang, and J. Y. Ying, "Aqueous synthesis of glutathione-capped cadmium-free Mn-doped ZnS-ZnSe quantum dots," Private communication (2008).

[4.10] J. F. Suyver, T. V. Beek, S. F. Wuister, J. J. Kelly, and A. Meijerink, "Luminescence of nanocrystalline ZnSe : Cu," *Appl. Phys. Lett*. **79**, 4222 (2001).

[4.11] B. Oczkiewicz, A. Twardowski, and M. Demianiuk, "Intra-manganese absorption and luminescence in $Zn_{1-x}Mn_xSe$ semimagnetic semiconductor," *Solid State Commun.* **64**, 107 (1987).

[4.12] Y. L. Qu, W. Ji, Y. Zheng, and J. Y. Ying, "Auger recombination and intraband absorption of two-photon-excited carriers in colloidal CdSe quantum dots," *Appl. Phys. Lett.* **90**, 133112 (2007).

[4.13] M. A. Albota, C. Xu, and W. W. Webb, "Two-photon fluorescence excitation cross sections of biomolecular probes from 690 to 960 nm," *Appl. Opt.* **37**, 7352 (1998).

[4.14] L. A. Padiha, J. Fu, D. J. Hagan, E. W. V. Stryland, C. L. Cesar, L. C. Barbosa, and C. H. B. Cruz, "Two-photon absorption in CdTe quantum dots," *Opt. Express* **13**, 6460 (2005).

[4.15] L. A. Padiha, J. Fu, D. J. Hagan, E. W. V. Stryland, C. L. Cesar, L. C. Barbosa, C. H. B. Cruz, D. Buso, and A. Martucci, "Frequency degenerate and nondegenerate two-photon absorption spectra of semiconductor quantum dots," *Phys. Rev. B* **75**, 075325 (2007).

[4.16] X. B. Feng, G. C. Xing, and W. Ji, "Two-photon-enhanced three-photon absorption in transition-metal-doped semiconductor quantum dots," *J. Opt. A* **11**, 024004 (2009).

Chapter 5

Two-photon-enhanced three-photon absorption in transition-metal-doped semiconductor QDs

5.1 Introduction

Recently, semiconductor QDs, or nanocrystals (NCs), have received considerable attention due to their potential applications in optical switching for optical communications, three-dimensional optical data storage, optical limiting for protection of optics sensors from laser-induced damages, three-dimensional confocal imaging for biological specimens, and photodynamic therapy [5.1-5.6]. In these applications, semiconductor QDs play an essential role in laser excitation through multiphoton absorption, namely, two-photon absorption (2PA) or three-photon absorption (3PA). Compared to 2PA, longer excitation wavelengths may be utilized in 3PA-based applications to provide deeper penetration depths in absorptive media and higher spatial resolution [5.7, 5.8]. Therefore, the understanding of 3PA in semiconductor QDs is of key importance to 3PA-related technologies as well as academic interest.

There have been tremendous advances in experimental investigations into 3PA in colloidal semiconductor QDs. Since 2004, there have been many reports [5.6, 5.9-5.12] on the characterization of 3PA in wide-gap semiconductor QDs made of CdS, CdSe, ZnS and ZnSe, some of which are simply capped by an organic layer in order to be dissolvable and stable in liquid; and others are made into core-shell structures for the improvement of light emission properties. With femtosecond pulsed excitation, Chon and his co-workers [5.9] measured the three-photon-excited band-edge and trap-state emission of colloidal organic-capped CdS QDs, and concluded that the 3PA cross-sections be on the order of 10^{-79} cm^6 s^2 $photon^{-2}$, which is three to four orders of magnitude higher than previously reported common UV fluorescent dyes. The 3PA cross-section of glutathione (GSH)-capped ZnS QDs in water was determined to be ~2.7×10^{-78} cm^6 s^2 $photon^{-2}$ [5.10] using both Z-scan and transient transmission techniques with femtosecond laser pulses at 780 nm. The 3PA of organic-capped CdSe QDs in hexane solution of five different dot-sizes were systematically investigated with femtosecond laser pulses at 1300 nm [5.6]. Very recently, Lad *et al.* [5.11] and Xing *et al.* [5.12] reported their measurements of 3PA cross-sections for organic-capped ZnSe QDs and/or core-shell ZnSe/ZnS QDs in solution. Furthermore, the 3PA cross-section of colloidal copper-doped ZnSe/ZnS QDs was also observed to be $3.5\times10^{-77}$$cm^6$ s^2 $photon^{-2}$, which is the largest value reported till date for semiconductor QDs with femtosecond laser pulses.

Theoretical studies, however, has lagged behind with only two reports [5.13, 5.14] till date. We have developed a frequency-degenerate 3PA theoretical model [5.14], based on the strategy employed by Fedorov *et al*. [5.15] for treatment of 2PA in semiconductor QDs. It is found that our model is in good agreement with the measured 3PA cross-sections of un-doped ZnS and CdSe QDs, within one order of magnitude. The model predicts the increase in the 3PA cross-section with the size of QDs in the strong confinement regime (QD radius < or ≈ a_B, exciton Bohr radius). Such an insightful knowledge is of direct relevance to engineering and optimizing colloidal semiconductor QDs for 3PA-related technologies.

Here we present the observation of enhancement in the 3PA of doped QDs (*d*-QDs): two-photon enhanced three-photon absorption. Within the bandgap of wide-gap semiconductor QDs, there inevitably exist some energy levels relating to surface/interface/defect states, or impurity states can be intentionally or un-intentionally introduced, as shown in Figure 5.1. If *d*-QDs are chosen in such a way that the excitonic energy matches to the energy of three photons ($3\hbar\omega$) and the energy difference between the ground states and the impurity (or called as dopant if it is intentional) states is equal to the energy of two photons ($2\hbar\omega$), the 3PA should be enhanced by the 2PA. Similar enhancement has been observed on the four-photon absorption of polydiacetylene-PTS [5.16] due to the degeneracy of three-photon and four-photon transitions. Normally, the density of states of surface/interface/defect/impurity in semiconductor QDs is largely dependent on the synthesis processes. However, it is well established that intentional doping is an effective method in semiconductor electronics and optoelectronics to alter the electronic and optical properties. In addition, suitable dopants in semiconductors can also significantly enhance PL, which is highly desirable by bio-imaging applications.

In Section 2, we first present the derivation of the 3PA theory for direct wide-gap semiconductor QDs without considering of the existence of energy levels inside the bandgap. In Section 3, we report the experimental details on the synthesis of organic-capped core-shell ZnSe/ZnS QDs, which are un-doped or doped with Mn ions, and the femtosecond Z-scan experiment employed to measure the 3PA. By comparing the experimental findings with the 3PA model, we highlight the two-photon enhanced 3PA cross-sections in Section 4. Finally, the conclusions are presented in Section 5.

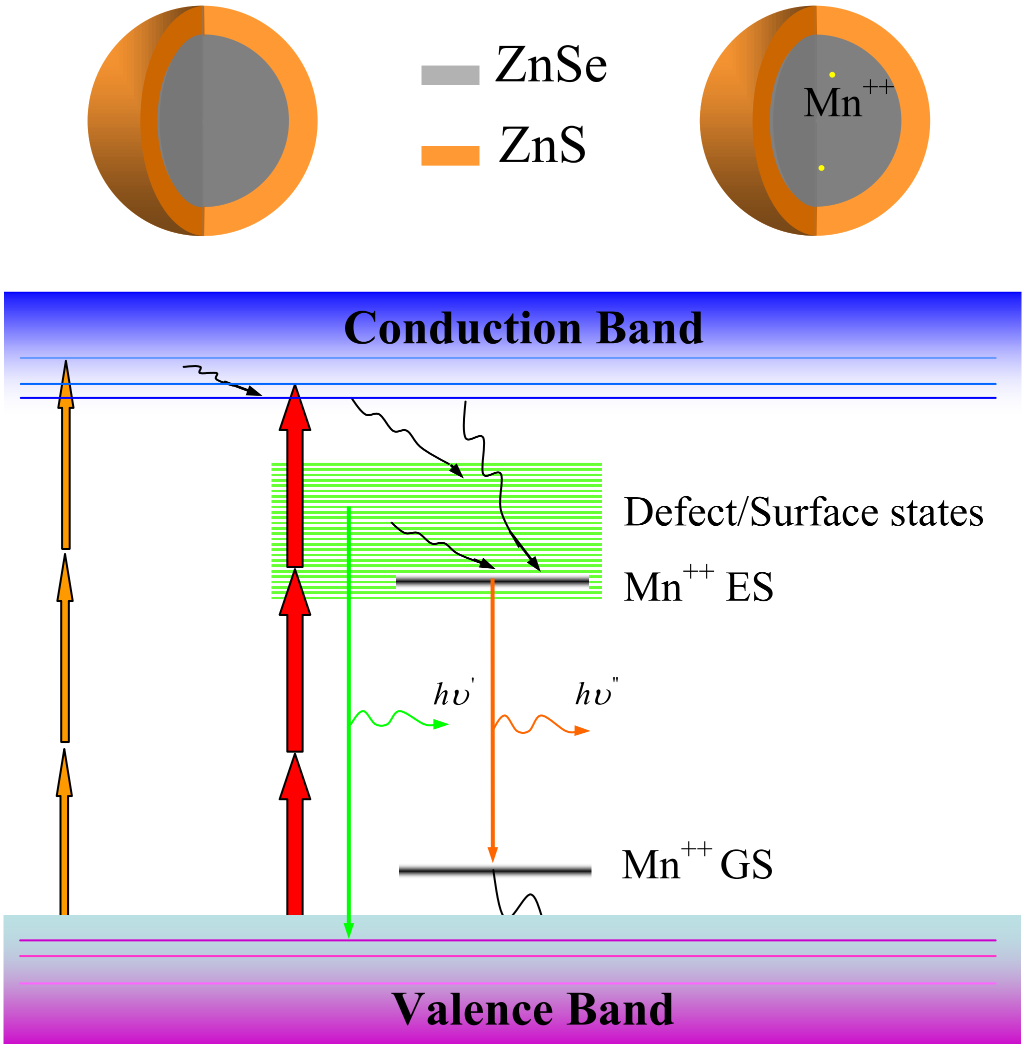

Figure 5.1. Schematic diagrams of ZnSe (gray)/ZnS (light orange) QDs and electronic structures. Valence Band (pink), Conduction Band (blue), Defect /Surface states (green) and Mn^{++} states (black).

5.2 Theory for 3PA in ZnSe QDs

Third-order time-dependent perturbation theory furnishes the following equation for the transition probability rate per unit volume of electrons in an initial state i being excited to a final state f by the simultaneous absorption of three photons, each of energy, $\hbar\omega$ [5.17]:

$$W^{(3)} = \frac{2\pi}{\hbar}\sum_{i,f}\left|M_{f,i}\right|^2 \delta(E_f - E_i - 3\hbar\omega) \tag{5.1}$$

$$M_{f,i} = \sum_{m,n}\frac{H^{\text{int}}_{f,m}H^{\text{int}}_{m,n}H^{\text{int}}_{n,i}}{(E_m - E_n - 2\hbar\omega - i\hbar\gamma_m)(E_n - E_i - \hbar\omega - i\hbar\gamma_n)} \tag{5.2}$$

where E_i, E_f and E_m (E_n) represent the energies of the initial, final and intermediate states of an electron, respectively. $H^{\text{int}} = (e/m_0c)\boldsymbol{A}\cdot\boldsymbol{p}$ describes the electron-photon interaction. $\boldsymbol{A} = A\boldsymbol{e}$ is the vector potential of the light wave with the amplitude A and the polarization vector $\boldsymbol{e}$, and $\boldsymbol{p}$ is the electron momentum operator, and γ is the inverse of the life-time in each excited state. The energy states can be calculated from the Schrödinger equation in the effective-mass approximation for the four-band model of a semiconductor QD with an isotropic and parabolic electronic spectrum, neglecting the coupling of three valence bands (heavy hole: *hh*, light hole: *lh*, spin-orbit-split hole: *so*) and the coupling between valence band and conduction band.

As for direct bandgap semiconductor QDs, four independent bands are taken into consideration, explicitly including the doubly degenerate conduction band and two-fold degenerate bands of *hh*, *lh*, and *so*; all the effective masses are constants, and there is no band mixing between the light and heavy holes in the valence bands [5.15]. It is also assumed that electrons and holes are located in a spherical potential well of radius

R with infinitely high barrier. Under the condition of strong confinement ($R <$ *or* $\approx a_B$), the Coulomb electron-hole correlation is negligible.

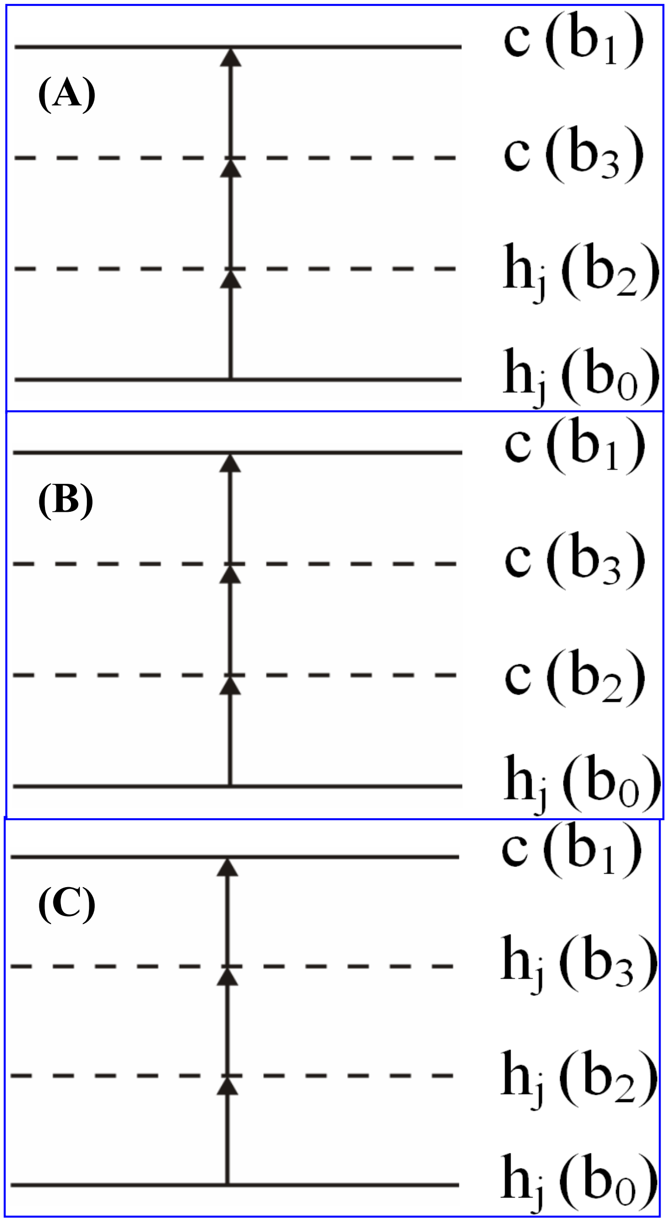

Figure 5.2. Three possible situations of 3PA transitions from the valence band to the conduction band.

Since frequency-degenerate 3PA is a process wherein three photons whose energies are the same are absorbed by the QD simultaneously through two virtual states to reach the excited state, each integrated 3PA process $h_j \rightarrow c$ contains two intraband transitions and one interband transition. Figure 5.2 illustrates three possible scenarios. Under the groundwork of interband and intraband transition matrix elements of the electron-photon interaction in QDs in Fedorov's 2PA theory [5.15], considering orientations and size distribution of QDs, the 3PA coefficient α_3 for an ensemble of QDs is related to the average three-photon generation rate $\overline{W}^{(3)}$ by

$$\alpha_3 = 6\hbar\omega \frac{N}{I^3} \int \overline{W}^{(3)} f(R) dR \tag{5.3}$$

where N is the QD concentration; I is the incident light intensity $I = \varepsilon_\omega^{1/2} \omega^2 A^2 (2\pi c)^{-1}$; ε_ω is the dielectric constant of semiconductor at the light frequency. In the experimental studies, the inhomogeneous size dispersion is characterized by a size-distribution function *f(R)*, the shape of which results from the conditions of sample preparation. Usually, the Gaussian function [5.18] and the Lifshits-Slezov distribution [5.19] are mostly used. For an arbitrary function $f(R)$, using the properties of the δ function, the 3PA coefficient can be expressed as the product of an envelope amplitude and an average form function:

$$\alpha_3 = B \sum_{j=1}^{3} \left\langle F_{c,h_j} \right\rangle \tag{5.4}$$

where the amplitude of the envelope and the average form function are given by the following two expressions, respectively:

$$B = \frac{6\pi\omega N}{\varepsilon_{\omega}^{3/2}} \left(\frac{8\pi e^2}{3\omega^2 c}\right)^3 (P\hbar)^2 \tag{5.5}$$

$$\left\langle F_{c,h_j} \right\rangle = \frac{1}{2\Delta_{h_j}} \sum_{\beta_1,\beta_2,\beta_0} (l_2\delta_{l_2,l_0+1} + l_0\delta_{l_2,l_0-1})(l_1\delta_{l_1,l_2+1} + l_2\delta_{l_1,l_2-1})$$

$$\times T^{c,h_j}_{\beta_1,\beta_2,\beta_0}(R^{(h_j)}_{\beta_1;\beta_0}) \frac{\xi^4_{\beta_2}\xi^2_{\beta_0}\xi^2_{\beta_1}}{(\xi^2_{\beta_2} - \xi^2_{\beta_0})^2(\xi^2_{\beta_1} - \xi^2_{\beta_2})^2} \frac{f(R^{(h_j)}_{\beta_1;\beta_0})}{(R^{(h_j)}_{\beta_1;\beta_0})^3} \tag{5.6}$$

The transition radius has been introduced in Eq. (5.6) and it is given as follows:

$$R^{(h_j)}_{\beta_1;\beta_0} = \left[\frac{\hbar^2}{2\Delta_{h_j}}\left(\frac{\xi^2_{\beta_1}}{m_c} + \frac{\xi^2_{\beta_0}}{m_{h_j}}\right)\right]^{1/2} \tag{5.7}$$

and $\Delta_{hj} = 3\hbar\omega\text{-}E_{hj}$, m_a is the effective mass in the a band; $\xi_\beta = \xi_{n,l}$ is the nth root of the lth order spherical Bessel function, $j_l(\xi_{n,l}) = 0$.

The corresponding selection rules for three-photon transition can be precisely obtained. Together with the one-photon-transition selection rule, it is easily found that the three-photon transition can occur from the valence band to the conduction band for which quantum number of the electron (l_1,m_1), hole (l_0,m_0), and the intermediate state (l_2,m_2) satisfy the relations of $l_2\text{-}l_0 = \pm1$, $l_2\text{-}l_1 = \pm1$, $m_2\text{-}m_0 = 0\pm1$, and $m_2\text{-}m_1 = 0\pm1$. In most experiments, 3PA is measured in terms of the 3PA cross-section, σ_3 which is defined as:

$$\sigma_3 = (\hbar\omega)^2 \alpha_3 / N \tag{5.8}$$

Following the analytical expressions derived above, we have calculated the frequency-degenerate 3PA cross-sections for ZnSe QDs, with the Gaussian size distribution [5.18]. Hereinafter calculations and discussions are carried out for ZnSe

QDs using the following parameters [5.20]: $E_g = 2.82\text{eV}$, $\Delta_{\text{so}} = 0.43\text{eV}$, $m_c = 0.14m_0$, $m_{hh} = 1.44m_0$, $m_{lh} = 0.149m_0$, and $m_{so} = 0.30m_0$.

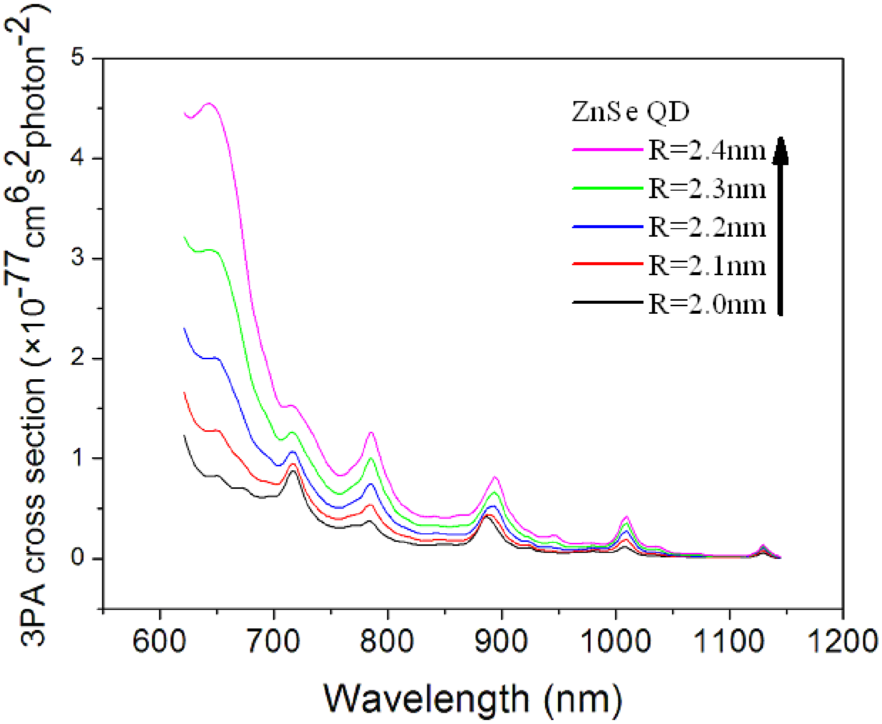

Figure 5.3. Calculated 3PA spectra of ZnSe QDs.

By applying our 3PA model to a system consisting of a large number of ZnSe QDs, their 3PA spectra are calculated in Figure 5.3 with the Gaussian size distribution (FWHM = 20%) and five different average radii. It is found that the 3PA cross-sections are in the range from 10^{-78} to 10^{-77} $\text{cm}^6\,\text{s}^2\,\text{photon}^{-2}$ in the spectral region of interest, with the precise values depending on both QDs' average size and incident light wavelength. For a given average radius in the range from 2.0 to 2.4 nm, the 3PA cross-section approaches zero as laser wavelength is increased to or beyond ~1200 nm, that is the triple of the center wavelength for the lowest exciton, $1S_{1/2}(e)\rightarrow 1S_{3/2}(h)$. At a fixed light wavelength, the 3PA cross-section increases with the increase of QD radius, similar to the 2PA case [5.21]. The positions of peaks in the 3PA spectra are determined by the energy denominators in term $T^{c,h_j}_{\beta_1,\beta_2,\beta_0}$ $(R^{(h_j)}_{\beta_1;\beta_0})$ in Eq. (5.6), which is indirectly dependent on the QD transition radius. The larger the QD size is, the denser the energy state becomes. As a consequence, it leads to more three-photon transitions being squeezed to a particular wavelength. In order to demonstrate this explanation, Figure 5.4 depicts the low-energy spectra of the form function F_{c,h_j}, for three average radii of ZnSe QDs. It is obvious that there is a low energy threshold which shifts to lower energies when increasing the average radius of QDs. In addition, the energy density of lines, or the number of lines per a given energy range, increases with the increase in the average radius of QDs.

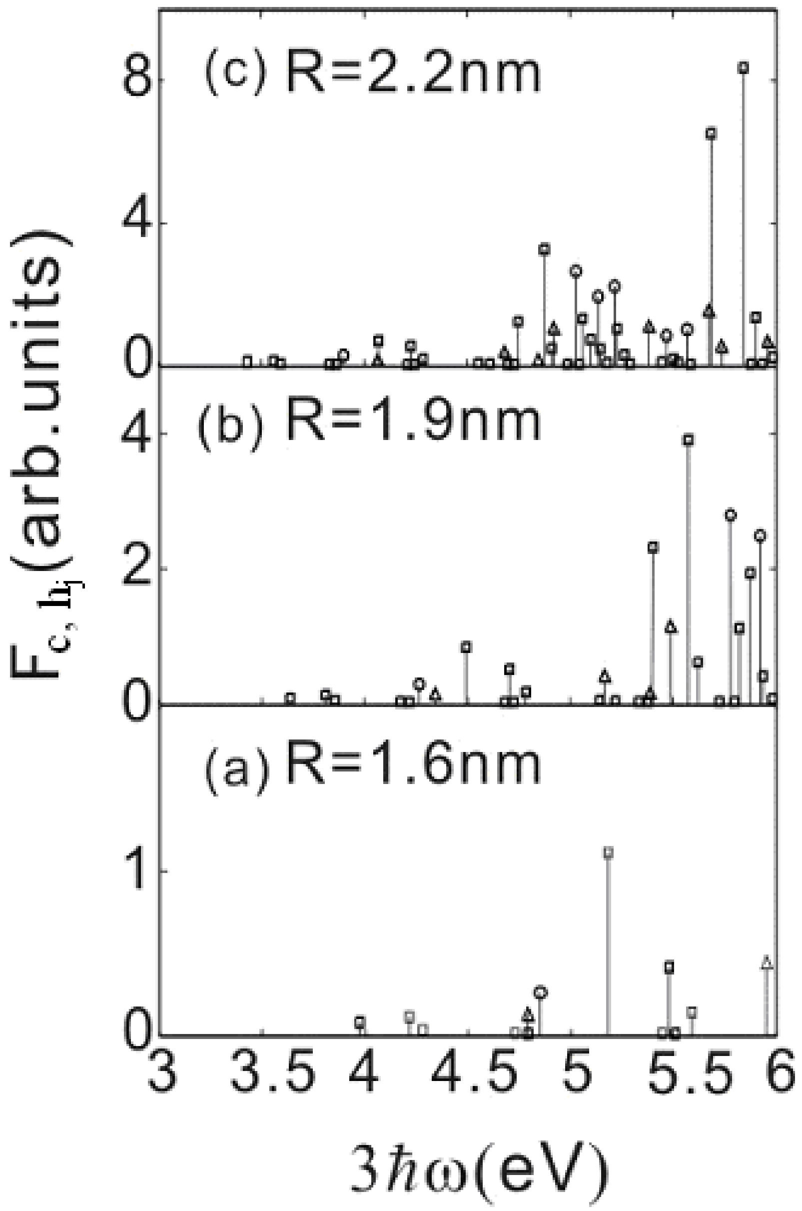

Figure 5.4. Calculated low-energy spectra of the form function F_{c,h_j} , for ZnSe QDs.

5.3 Experiments

The synthesis of ZnSe/ZnS QDs was based on the reaction of zinc acetate with sodium hydroselenide in dimethylsulfoxide (DMSO) as solvent. Sodium hydroselenide was prepared by mixing sodium borohydride and selenium powder in methanol under nitrogen. When the selenium powder was completely reduced by $NaBH_4$, 10 ml of freshly prepared NaHSe solution (0.4 M in methanol) was added into another solution containing 50 ml of 0.2 M of zinc acetate with vigorous stirring. Then the NaHSe precursor, 6 ml of 1 M of Na_2S solution was injected under vigorous stirring. The resulting mixture was precipitated with 10 ml of 1 M of mercaptopropionic acid (MPA), with pH adjustment to 11 with NaOH. After the centrifuge and washing, the precipitation was re-suspended in water, and then heated to 95ºC for 2 hours to grow MPA-capped ZnSe/ZnS QDs to a final diameter of ~ 4.4 nm.

The synthesis of Mn-doped ZnSe/ZnS QDs is briefly described in the following. 10 ml of freshly prepared NaHSe solution (0.02 M) was added into another solution containing 50 ml of 0.01 M $ZnCl_2$/$MnCl_2$ and GSH at a pH of 11.5 with vigorous stirring. After the injection of NaHSe precursor, 0.3 ml solution of 1 M Na_2S was injected under vigorous solution. The amounts of Zn, Mn, Se, S and GSH introduced were 0.5, 0.005, 0.2, 0.3 and 0.6 mmol, respectively, in a total volume of 50 ml. The resulting mixture was heated to 95ºC, and the growth of GSH-capped QDs began immediately. The final diameter was 4.1 nm on average. In the *d*-QDs, 1% Zn ions in the core were substituted by Mn ions.

The as-prepared QDs in aqueous solutions were examined by taking their spectra of one-photon absorption and PL excited with a wavelength of 360 nm. The crystalline structures and sizes were studied by both XRD measurements and transmission electron microscopy (TEM). In order to determine the 3PA cross-sections, open-aperture Z-scans were conducted. The Z-scan set-up was similar to the one used in Ref. [5.22]. The laser pulses of wavelengths ranging from 850 to 1064 nm were provided by a Coherent Legend (seeded by Mira) pumped TOPAS-C operating at 1 kHz repetition rate. The full width at half maximum (FWHM) of the laser pulse duration was 200 fs. After the spatial filter, the spatial profiles of the pulses were of near Gaussian distribution. The pulses were then divided into two parts: one part was used as the reference, and the other part was focused with a focus lens ($f = 10$ cm) in the Z-scans. The beam radius at the focus was measured to be 12±2 um. The incident and transmitted laser pulses were monitored with two energy detectors (Laser Probe RKP 465). The QD solutions were contained in 1-mm-thick quartz cells and Z-scanned along the focused laser beam in the Z-axis. All the Z-scans were carried out at room temperature. The maximum laser irradiance was controlled at 250 GW/cm^2, below which no laser-induced damage or degradation on the QD solution was observed. Furthermore, the Z-scans on pure water under the same experimental conditions confirmed that water made no contribution to the Z-scan signals obtained from the QD solutions.

5.4 Results and discussion

As shown in Figure 5.5, the one-photon absorption spectra can be fit with a series of Gaussian functions (black lines). The lowest exciton, $1S_{1/2}(e)\rightarrow 1S_{3/2}(h)$, is peaked at 365 nm and 388 nm, respectively, for the *d*-QDs and un-doped QDs. Thus, 3PA is expected to manifest itself in the spectral range from 750 to 1200 nm. The band-edge light emission is quenched, consistent with the previous reports [5.23, 5.24]. There is a broadband of PL centered at 590 nm and 498 nm, respectively, for the *d*-QDs and the un-doped QDs. The PL quantum yield of the *d*-QDs is found to be 11 times as strong as that of the un-doped QDs. The origins of the PL bands are attributed to transitions involved in the interface/surface/defect states of un-doped QDs, as shown by the green downward arrow in Figure 5.1, or are predominated by transitions involved in Mn^{++}-related states of the *d*-QDs, as displayed by the red downward arrow in Figure 5.1. The crystalline structures and sizes have been determined accurately by the XRD and TEM studies which have been shown in Chapter 3 and 4. The average diameters are 4.1 nm and 4.4 nm, respectively, for the *d*-QDs and un-doped QDs with size dispersion of 20% or less.

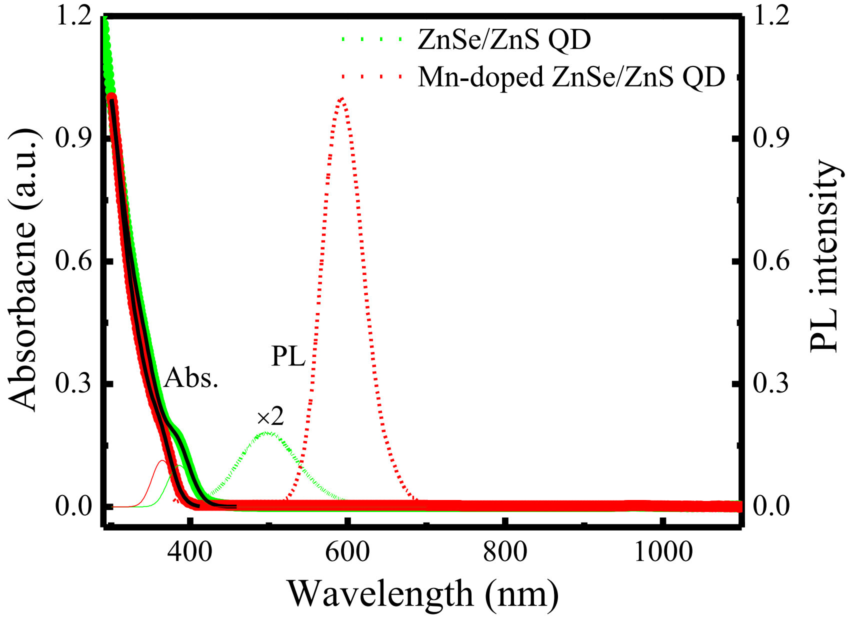

Figure 5.5. Measured spectra of one-photon absorption (thick solid lines) and photoluminescence (PL) excited 360 nm (dotted lines). The thin solid lines show the Gaussian fits to the lowest exciton. The black lines are the fits with a series of Gaussian functions.

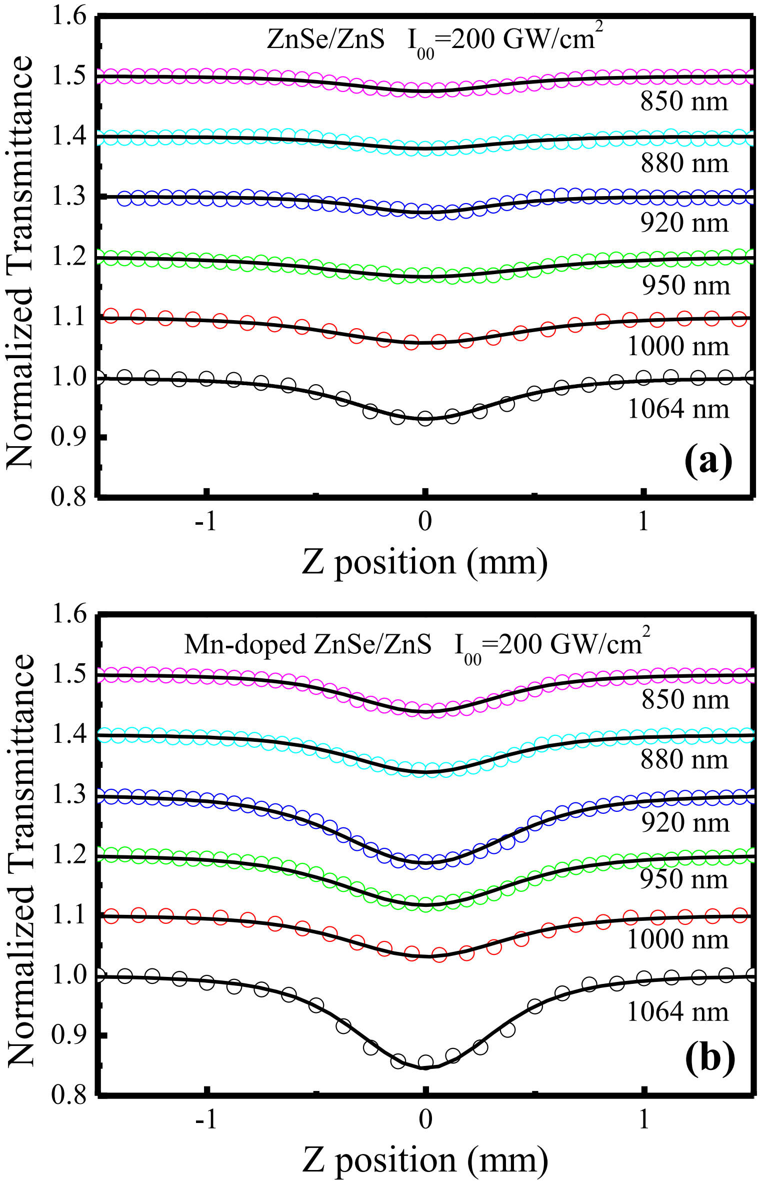

Figure 5.6. Open-aperture Z-scans with 200-fs laser pulses. The top five Z-scans are shifted vertically for clear presentation.

Typical open-aperture Z-scans are depicted in Figure 5.6. Evidently, the Z-scan signals increase with the laser wavelength. To extract the 3PA coefficient, the measured Z-scans are fit with the theory of Z-scan signal induced by 3PA [5.25], as shown by the solid lines in Figure 5.6. Then, the 3PA cross-sections are inferred by Eq. (5.8). These values are summarized in Table 5.1. Within the experimental errors, the agreement can be reached between the experiments and the theory at shorter wavelengths (< 920 nm). This observation is also consistent with our previous report for colloidal ZnS QDs [5.14].

Table 5.1. Measured and calculated 3PA cross-sections.

Quantum dots (QDs)	Diameter (nm)	Wavelength λ (nm)	σ_3 (cm^6 s^2 photon^{-2})	
			Experiment	Theory
Mn-doped ZnSe/ZnS QDs	4.1	850	4.6×10^{-78}	4.5×10^{-78}
Mn-doped ZnSe/ZnS QDs	4.1	880	3.3×10^{-78}	6.9×10^{-78}
Mn-doped ZnSe/ZnS QDs	4.1	920	8.1×10^{-78}	2.4×10^{-78}
Mn-doped ZnSe/ZnS QDs	4.1	950	7.4×10^{-78}	1.3×10^{-78}
Mn-doped ZnSe/ZnS QDs	4.1	1000	3.7×10^{-77}	2.2×10^{-78}
Mn-doped ZnSe/ZnS QDs	4.1	1064	8.5×10^{-77}	0.3×10^{-78}
ZnSe/ZnS QDs	4.4	850	2.4×10^{-78}	2.5×10^{-78}
ZnSe/ZnS QDs	4.4	880	2.4×10^{-78}	3.9×10^{-78}
ZnSe/ZnS QDs	4.4	920	1.3×10^{-78}	1.7×10^{-78}
ZnSe/ZnS QDs	4.4	950	5.0×10^{-78}	1.0×10^{-78}
ZnSe/ZnS QDs	4.4	1000	2.0×10^{-77}	1.8×10^{-78}
ZnSe/ZnS QDs	4.4	1064	3.6×10^{-77}	0.25×10^{-78}

Experimental errors are ±50%

It is interesting to note that there are large discrepancies at longer wavelengths. At 1000 nm, the theoretical predictions are 2.2×10^{-78} and 1.8×10^{-78} cm^6 s^2 $photon^{-2}$, respectively, for the *d*-QDs and un-doped QDs. The experiments, however, show 6-fold and 2.5-fold increase correspondingly. At 1064 nm, the 100-fold increase can be found in the *d*-QDs. Such a large enhancement should be anticipated because the theoretical model in Section 2 is derived under the four-band approximation, neglecting the existence of energy levels inside the bandgap. The in-gap energy levels are a result of interface-surface, defects or impurities that are unintentionally or intentionally present in QDs. Their density of states is increased considerably if a significant amount of dopants is introduced on purpose. These dopant-related states play an important role in the enhancement. The enhancement is on resonance if the energy differences between the hole states in the valence band and the dopant states are equal to $2\hbar\omega$, with the excitonic energy matching to $3\hbar\omega$. Therefore, the measured 3PA cross-section in the *d*-QDs is increased greatly as the energy of two photons approaches to the resonance. By conception, this type of enhancement is similar to the three-photon-enhanced four-photon absorption observed in polydiacetylene-PTS [5.16].

At wavelengths of 920 nm and 950 nm, the enhancement also manifests itself in the *d*-QDs, though these photon energies are off-resonant with the dopant states in terms of two-photon transitions. In this case, the states of interface/surface/defect play a supplementary role in the enhancement, though their contributions to the PL signal are quenched as the excited electrons preferably relax to the dopant state in the *d*-QDs. In fact, the enhancement is in good agreement with the summation of the PL signals from the *d*-QDs and the un-doped QDs, see the black dashed line, which reflect the total density of states inside the bandgap of the *d*-QDs.

It has been reported [5.23, 5.24] that transition-metal doping can enhance the PL quantum yield of *d*-QDs. In our case, we have found an increase of 11-fold in the PL quantum yield if ZnSe/ZnS QDs are doped with 1% Mn ions. More importantly, the findings presented here points out that the doping also results in the enhanced 3PA. Such double enhancements are highly desirable in the design and optimization of fluorescent QDs for applications of three-photon-excited fluorescence.

5.5 Conclusion

In conclusion, two-photon-enhanced three-photon absorption in organic-capped, core-shell, transition-metal-doped ZnSe/ZnS QDs has been revealed by comparing the theoretically calculated 3PA cross-sections with the experimentally measured ones in the near infrared spectral region. Due to the degeneracy between two-photon transitions mainly to the states of dopants and three-photon transition to the excitionic state, the 3PA cross-section is enhanced by two orders of magnitude at 1064 nm. Taking into account the enhancement in PL, such double enhancements make ZnSe/ZnS QDs doped with transition-metal ions a promising candidate for applications based on three-photon-excited fluorescence.

References:

[5.1] X. Michalet, F. F. Pinaud, L. A. Bentolila, J. M. Tsay, S. Doose, J. J. Li, G. Sundaresan, A. M. Wu, S. S. Gambhir, and S. Weiss, "Quantum dots for live cells, in vivo imaging, and diagnostics," *Science* **307**, 538 (2005).

[5.2] J. R. Petta, A. C. Johnson, J. M. Taylor, E. A. Laird, A. Yacoby, M. D. Lukin, C. M. Marcus, M. P. Hanson, and A. C. Gossard, "Coherent manipulation of coupled electron spins in semiconductor quantum dots," *Science* **309,** 2180 (2005).

[5.3] D. R. Larson, W. R. Zipfel, R. M. Williams, S. W. Clark, M. P. Bruchez, F. W. Wise, and W. W. Webb, "Water-soluble quantum dots for multiphoton fluorescence imaging in vivo," *Science* **300,** 1434 (2003).

[5.4] J. Staromlynska, T. J. McKay, and P. Wilson, "Broadband optical limiting based on excited state absorption in Pt: ethynyl," *J. Appl. Phys*. **88,** 1726 (2000).

[5.5] B. Dubertret, P. Skourides, D. J. Norris, V. Noireaux, A. H. Brivanlou, and A. Libchaber, "In vivo imaging of quantum dots encapsulated in phospholipid micelles," *Science* **298,** 1759 (2002).

[5.6] G. S. He, K-T. Yong, Q. Zheng, Y. Sahoo, A. Baev, A. I. Ryasnyanskiy, and P. N. Prasad, "Multi-photon excitation properties of CdSe quantum dots solutions and optical limiting behavior in infrared range," *Opt. Express* **15**, 12818 (2007).

[5.7] F. E. Hernandez, K. D. Belfield, and I. Cohanoschi, "Three-photon absorption enhancement in a symmetrical charge transfer fluorene derivative," *Chem. Phys. Lett.* **391**, 22 (2004).

[5.8] F. E. Hernandez, K. D. Belfield, I. Cohanoschi, M. Balu, and K. J. Schafer, "Three- and four-photon absorption of a multiphoton absorbing fluorescent probe," *Appl. Opt.* **43**, 5394 (2004).

[5.9] J. W. M. Chon, M. Gu, C. Bullen, and P. Mulvaney, "Three-photon excited band edge and trap emission of CdS semiconductor nanocrystals," *Appl. Phys. Lett*. **84**, 4472 (2004).

[5.10] J. He, W. Ji, J. Mi, Y. G. Zheng, and J. Y. Ying, "Three-photon absorption in water-soluble ZnS nanocrystals," *Appl. Phys. Lett*. **88**, 181114 (2006).

[5.11] A. D. Lad, P. P. Kiran, G. R. Kumar, and S. Mahamuni, "Three-photon absorption in ZnSe and ZnSe/ZnS quantum dots," *Appl. Phys. Lett*. **90,** 133113 (2007).

[5.12] G. C. Xing, W. Ji, Y. Zheng, and J. Y. Ying, "High efficiency and nearly cubic power dependence of below-band-edge photoluminescence in water-soluble, copper-doped ZnSe/ZnS quantum dots," *Opt. Express* **16**, 5710 (2008).

[5.13] X. B. Feng, G. C. Xiong, X. Zhang, and H. L. Jiang, "Size-dependent interband three-photon absorption properties of spherical CdTe quantum dots," *J. Phys.: Condens. Matter* **20,** 025219 (2008).

[5.14] X. B. Feng, Y. L. Ang, J. He, W. J. Beh Cyrus, H. R. Xu, S. C. Wee, and W. Ji, "Three-photon absorption in semiconductor quantum dots: experiment," *Optics Express* **16,** 6999 (2008).

[5.15] A. V. Fedorov, A. V. Baranov, and K. Inoue, "Two-photon transitions in systems with semiconductor quantum dots," *Phys. Rev. B.* **54,** 8627(1996).

[5.16] F. Yoshino, S. Polyakov, M. Liu, and G. Stegeman, "Observation of three-photon enhanced four-photon absorption," *Phys. Rev. Lett.* **91,** 063902 (2003).

[5.17] V. Nathan, A. H. Guenther, and S. S. Mitra, “Review of multiphoton absorption in crystalline solids,” *J. Opt. Soc. Am. B.* **2,** 294 (1985).

[5.18] W. Y. Wu, J. N. Schulman, T. Y. Hsu, and U. Efron, “Effect of size nonuniformity on the absorption-spectrum of a semiconductor quantum dot system,” *Appl. Phys. Lett.* **51,** 710 (1987).

[5.19] I. M. Lifshits and V. V. Slezov, “Kinetics of diffusion decomposition of supersaturated solid solutions,” *Zhurn. Eksp. i Tekch. Fiz.* **35**, 479 (1958).

[5.20] P. Lawaetz, “Valence-band parameters in cubic semiconductors,” *Phys. Rev. B* **4,** 3460 (1971).

[5.21] L. A. Padiha, J. Fu, D. J. Hagan, E. W. V. Stryland, C. L. Cesar, L. C. Barbosa, C. H. B. Cruz, D. Buso, and A. Martucci, “Frequency degenerate and nondegenerate two-photon absorption spectra of semiconductor quantum dots,” *Phys. Rev. B* **75**, 075325 (2007).

[5.22] M. Sheik-Bahae, A.A. Said, T.H. Wei, D.J. Hagan, and E.W. van Styland, “Sensitive measurement of optical nonlinearities using a single beam,” *IEEE J. Quantum Electron*. **26**, 760 (1990).

[5.23] N. Pradhan, D. Goorskey, J. Thessing, and X. G. Peng, “An alternative of CdSe nanocrystal emitters: pure and tunable impurity emissions in ZnSe nanocrystals,” *J. Am. Chem Soc.* **127,** 17586 (2005).

[5.24] N. Pradhan, D. M. Battaglia, Y. Liu, and X. G. Peng, “Efficient, stable, small, and water-soluble doped ZnSe nanocrystal emitters as non-cadmium biomedical labels,” *Nano Lett.* **7,** 312 (2007).

[5.25] J. He, Y. L. Qu, H. P. Li, J. Mi, and W. Ji, "Three-photon absorption in ZnO and ZnS crystals," *Opt. Express* **13,** 923 (2005).

Chapter 6

Enhanced upconversion photoluminescence by two-photon excited transition to defect states in Cu-doped semiconductor QDs

6.1 Introduction

Transition-metal-doped semiconductor QDs are attracting broad interests for their improved optoelectronic properties compared to their non-doped counterparts [6.1-6.7]. For example, by incorporating different dopants to semiconductor QDs, one can reduce their lasing threshold [6.1, 6.2], suppress undesirable reactions on their surface [6.3], increase their conductivity over ten orders of magnitude, [6.4] enhance their quantum yield [6.5, 6.6] and impart magneto-optical properties to them [6.7]. Among various doped semiconductor QDs, Mn^{2+} doped ZnS and ZnSe QDs are mostly investigated for their high quantum yield and outstanding dilute magnetic properties. However, since the radiative transition from $^4T_1$ to the ground state in Mn^{2+} ions is spin forbidden, their photoluminescence (PL) lifetimes are in the millisecond time range and central emission wavelengths are almost fixed [6.8, 6.9], which hinder their ultrafast and multicolor applications. In comparison, the PL of Cu^{2+} doped ZnS and ZnSe QDs arises from the copper related trapped electrons recombining with Cu^{2+} ions, therefore, the PL lifetime is in microsecond time range and emission wavelength is tunable by tailoring the size [6.3, 6.10]. For the PL properties of Cu-doped ZnS and ZnSe QDs, the research was usually focused on exciting electrons from valance band (VB) to conduction band (CB) in the host through one-photon absorption. However, the study of upconversion PL has been rarely reported. In particular, the relationship between Cu doping and two-photon absorption (2PA) as well as two-photon-induced carrier dynamic has never been investigated. In this Chapter, we systematically investigated both 2PA and two-photon excited PL dynamics of Cu-doped ZnSe/ZnS QDs with femtosecond laser pulses. The contribution of defect states to these two processes was clearly revealed. The results should provide the essential knowledge for the application of copper-doped semiconductor QDs as upconversion lasers, multiphoton imaging materials and optical data storages.

6.2 Samples

The ZnSe/ZnS and Cu-doped ZnSe/ZnS core-shell colloidal QDs of different size were prepared based on the reaction of zinc acetate with sodium hydroselenide in dimethylsulfoxide (DMSO) as solvent [6.11, 6.12]. In the resulted doped QDs, 1% of the Zn^{2+} ions in the core were substituted by Cu^{2+} ions, the ZnS shell was 1~2 atomic layers, and then the QDs was coated with an organic layer to be dissolvable in water. The overall diameters were estimated from high-resolution transmission electron microscopy (HRTEM) to be 4.4 nm, 4.1 nm and 3.2 nm, respectively for ZnSe/ZnS (A), Zn(Cu)Se/ZnS (B) and Zn(Cu)Se/ZnS (C) QDs, and the size dispersion was ~20% for all the samples. The weight concentrations were kept the same for all three samples (50 ± 2 mg/mL). The corresponding particle number concentrations were calculated to 2.1, 2.6 and 5.5 $\times 10^{17}$/mL. The X-ray diffraction (XRD) pattern of the vacuum-dried powder confirmed these QDs remained a zinc blend crystal structure. The TEM and XRD results of 3.2-nm-sized Cu-doped ZnSe/ZnS QDs are shown in Figure 6.1(a) and (b). The other results have been shown previously.

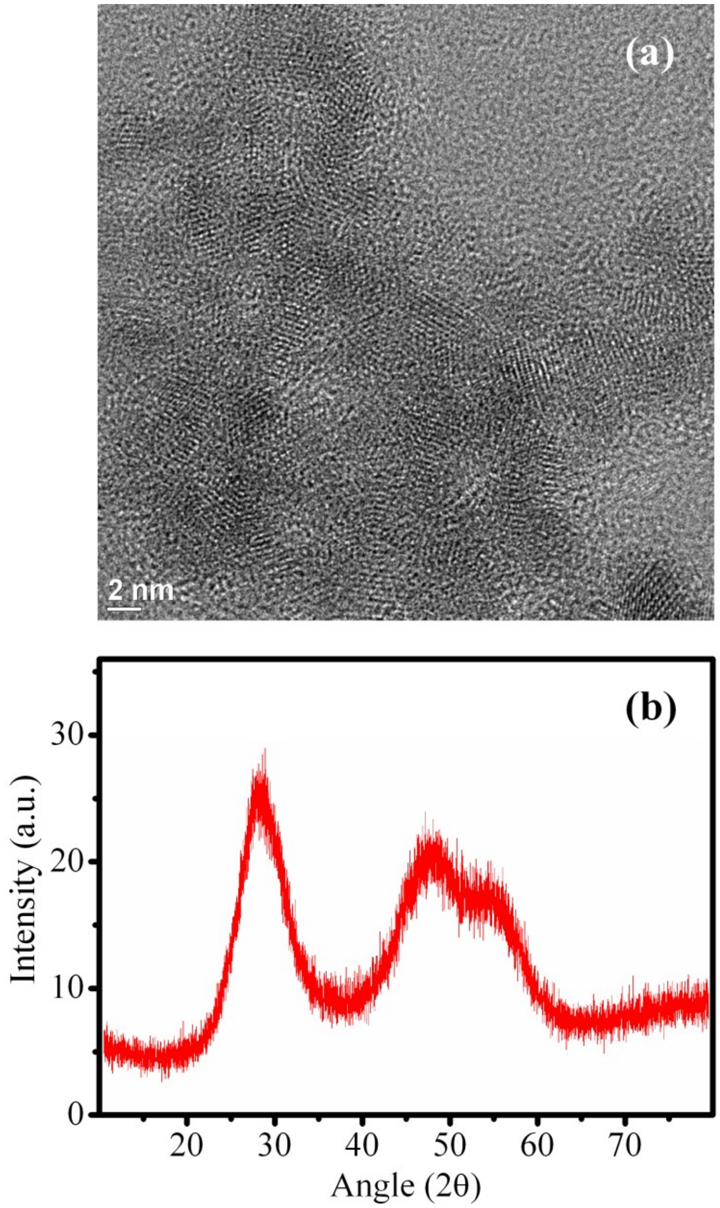

Figure 6.1. (a) TEM images and (b) XRD pattern of the Cu-doped ZnSe/ZnS QDs-C.

6.3 Linear absorption and one-photon-excited PL spectra

The linear absorption spectra of these QDs in water solution are shown in Figure 6.2. Through Gaussian curves fitting, the lowest excitonic transitions $1S(e)\text{-}1S_{3/2}(h)$ were determined to be around 3.2 eV, 3.4 eV and 3.96 eV for QDs-A, -B and -C respectively. If compared with ZnSe bulk crystal (E_g = 2.7 eV, a_B = 4.5 nm), the strong quantum confinement effect is clearly revealed. Figure 6.2 also shows the one-photon (300 nm) excited steady state PL spectra of these three samples. In this experiment, a xenon lamp was used as the excitation source. The obtained spectra show that the band-edge emission of the ZnSe core was almost completely quenched and the defect-state-related emission in the undoped QDs was centered at 498 nm; while in the Cu-doped QDs, the electronic emissive transition from the defect-states to the d-orbital of the Cu^{2+} ions is size tunable. The PL peak is obviously shifted from 520 nm to 470 nm as the size decreases from 4.1 nm to 3.2 nm. This kind of Cu^{2+} ions related emission is far away from the excitonic absorption (large Stokes shift), which would greatly suppress self-quenching in these QD assembles.

Though the PL spectra of the Cu-doped ZnSe/ZnS QDs-B and-C are partially overlapped with the defect state emission spectrum of un-doped ZnSe/ZnS QDs-A, the dominance of the Cu related emission in Cu-doped QDs can be clearly revealed from the time resolved PL spectra which will be shown later. This Cu related emission is also different from isolated Cu atoms or ions emission, which is shown in Figure 6.3. This result further confirms the successful incorporation of Cu ions into the ZnSe crystal lattice.

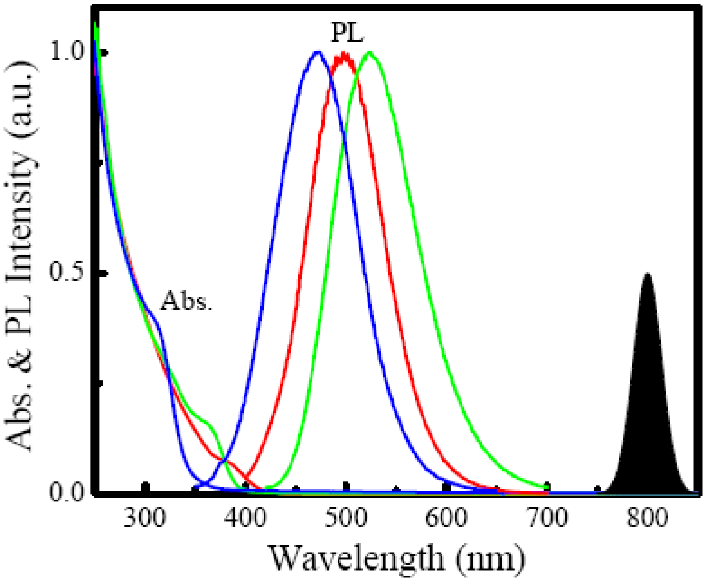

Figure 6.2. UV-visible absorption spectra and PL spectra excited at 300 nm for 4.4-nm-sized ZnSe/ZnS (red, A), 4.1-nm-sized Zn(Cu)Se/ZnS (green, B), and 3.2-nm-sized Zn(Cu)Se/ZnS (blue, C). Black area shows the laser spectrum for upconversion excitation source. All the spectra are normalized to their peaks for comparison.

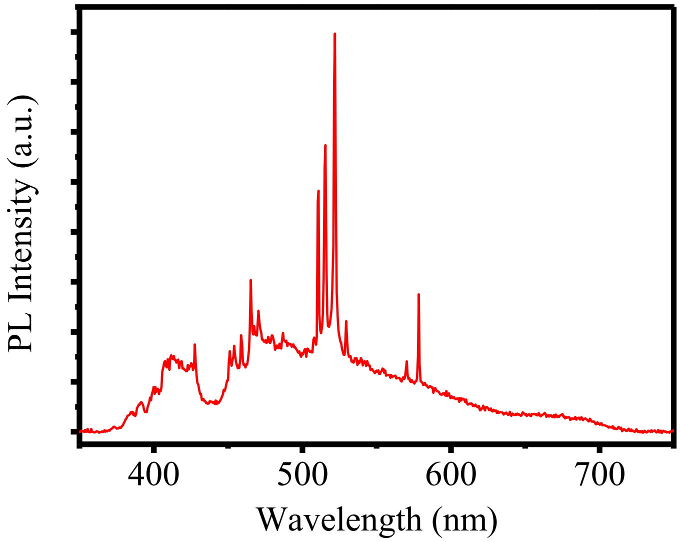

Figure 6.3. Emission spectrum of Cu under high-intensity, 200 fs and 800 nm laser pulse excitation.

At 400 nm, the quantum yields of these QDs samples were determined by comparing the PL with a standard reference sample (Rodamine6G in Methanol). With the same light pump intensity and same experimental setup (samples were contained in 1mm quartz cell), the collected PL intensity was proportional to the quantum yield of sample and photons absorbed. Then the quantum yield can be calculated as:

$$\eta_s = \eta_r \frac{PL_s}{PL_r} \cdot \frac{(1-T_r)}{(1-T_s)} \tag{6.1}$$

where η_s, PL_s and T_s are quantum yield, the integrated PL intensity and light transmittance at the excitation wavelength of the sample. η_r, PL_r and T_r are quantum yield, the integrated PL intensity and light transmittance at the excitation wavelength of the reference sample. The obtained results were listed in Table 6.1.

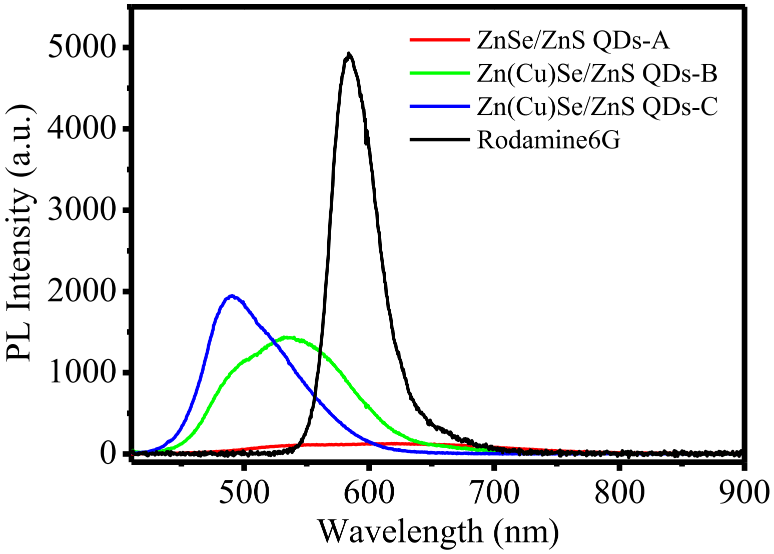

Figure 6.4. (a) 400-nm laser pulses excited PL spectra for QDs-A, -B, -C and Rodamine 6G in methanol with corresponding transmittances of 3.7%, 56.9%, 82.6% and 83%.

6.4 Two-photon-excited PL

To explore the upconversion PL properties of these QDs, they were excited with ultrashort femtosecond (fs) laser pulses. The excitation source was a Ti:Sapphire oscillator (Spectra Physics, Tsunami, pulse duration = 40 fs, repetition rate = 76 MHz and center wavelength = 800 nm). The laser pulses were focused by a lens (*f* = 15 cm) onto the QD solution in a 1-cm-thick quartz cell, with a focal spot size of ~ 20 μm. The emission from the QDs was collected at an angle of 90° by a pair of lenses and optical fibers, and directed to a spectrometer (Acton, Spectra Pro 2300i coupled CCD Princeton Instruments, Pixis 100B). A short-pass filter with a cut-off wavelength of 730 nm was placed before the spectrometer to minimize the scattered excitation light. The capping agent (GSH) in water was also measured under the same condition, which confirmed that its PL contribution was negligible.

The pump intensity dependent PL spectra for QDs-A, -B and -C are shown in Figure 6.5(a), 6.6(a) and 6.7(a) respectively. Figure 6.5(b), 6.6(b) and 6.7(b) depict the quadratic power dependence for corresponding PL signals. Under relatively low light excitation ($< 2\,\mathrm{GW/cm^2}$), the quadratic power dependence manifests the dominance of 2PA in this process. In un-doped QD-A (E_g = 3.2 eV) and Cu-doped QDs-B (E_g = 3.4 eV), two 1.55 eV photons energy can reach part of the QDs' bandgap due to the ~20% size distribution. However, In Cu-doped QDs-C (E_g = 3.96 eV), two 1.55 eV photons energy is far below the bandgap. Therefore the obtained upconversion emission in QDs-C was mainly originated from defect states when excited with two 1.55 eV photons, which was also confirmed by the upconversion time-resolved PL experiment at the same excitation wavelength.

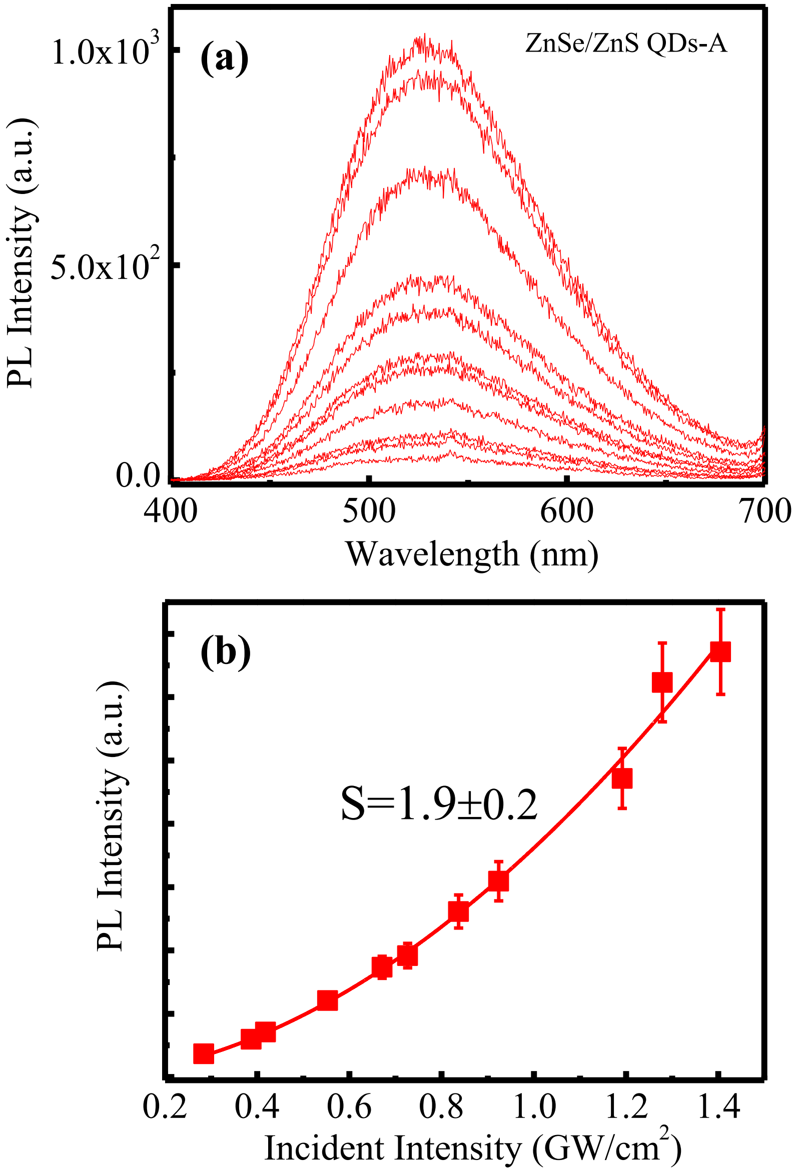

Figure 6.5. (a) 40-fs, 800-nm laser pulse excited PL spectra for 4.4-nm-sized ZnSe/ZnS QDs-A, Integration time is 5s. (b) The PL signals measured as a function of excitation intensity and the best fit with $y = a \cdot x^S$.

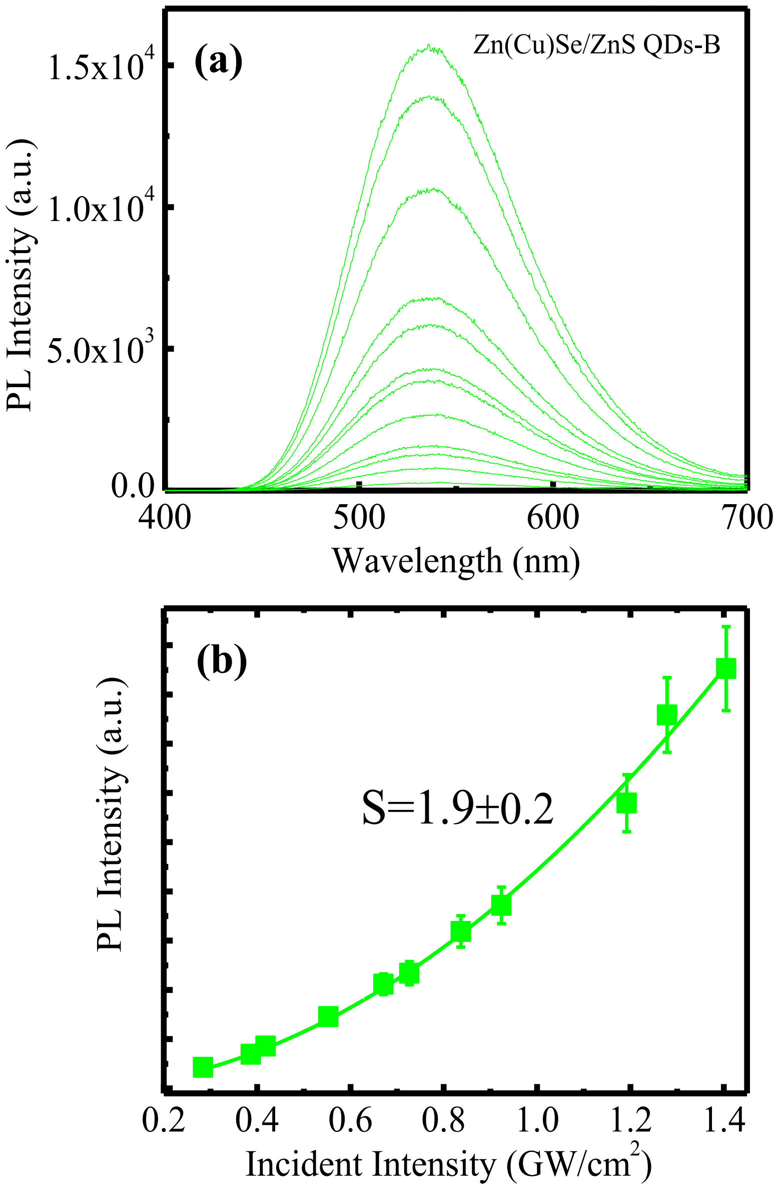

Figure 6.6. (a) 40-fs, 800-nm laser pulse excited photoluminescence spectra for 4.1-nm-sized Cu-doped ZnSe/ZnS QDs-B, Integration time is 1s. (b) The PL signals measured as a function of excitation intensity and the best fit with $y = a \cdot x^S$.

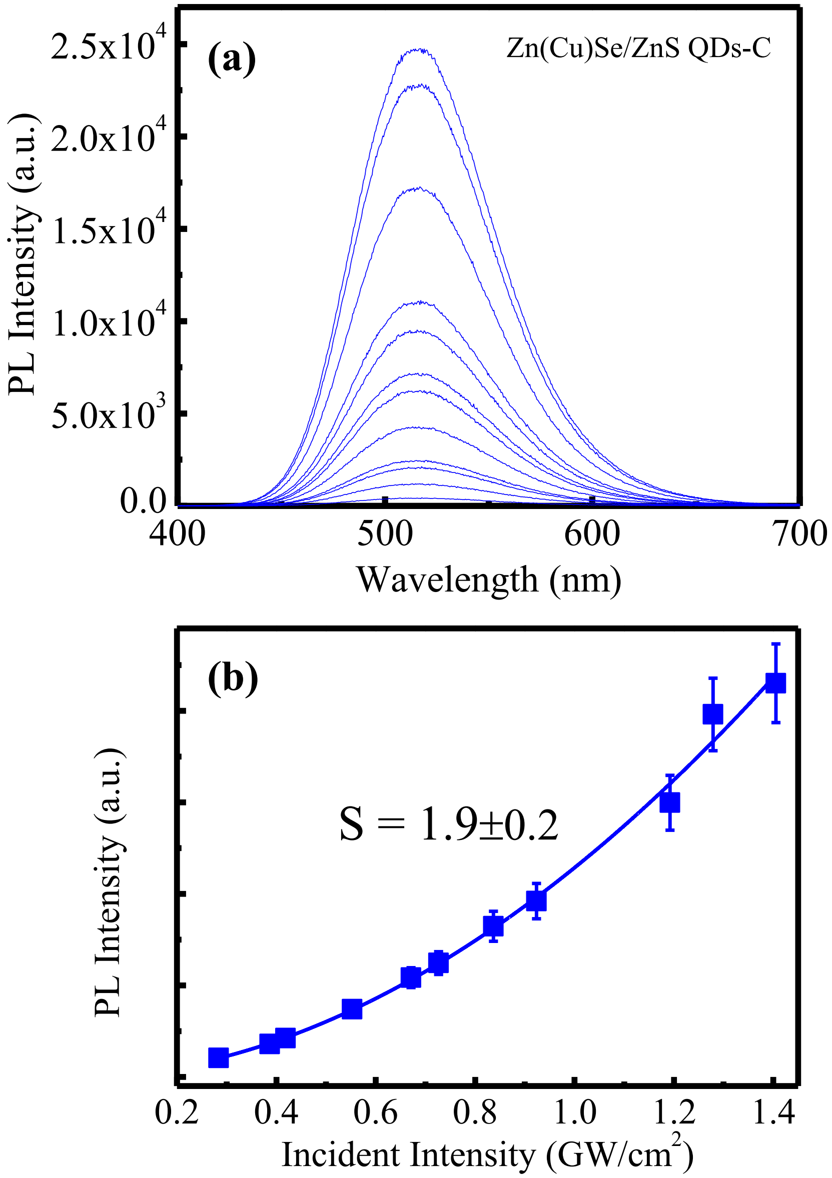

Figure 6.7. (a) 40-fs, 800-nm laser pulse excited photoluminescence spectra for 3.2-nm-sized Cu-doped ZnSe/ZnS QDs-C, Integration time is 1s. (b) The PL signals measured as a function of excitation intensity and the best fit with $y = a \cdot x^S$.

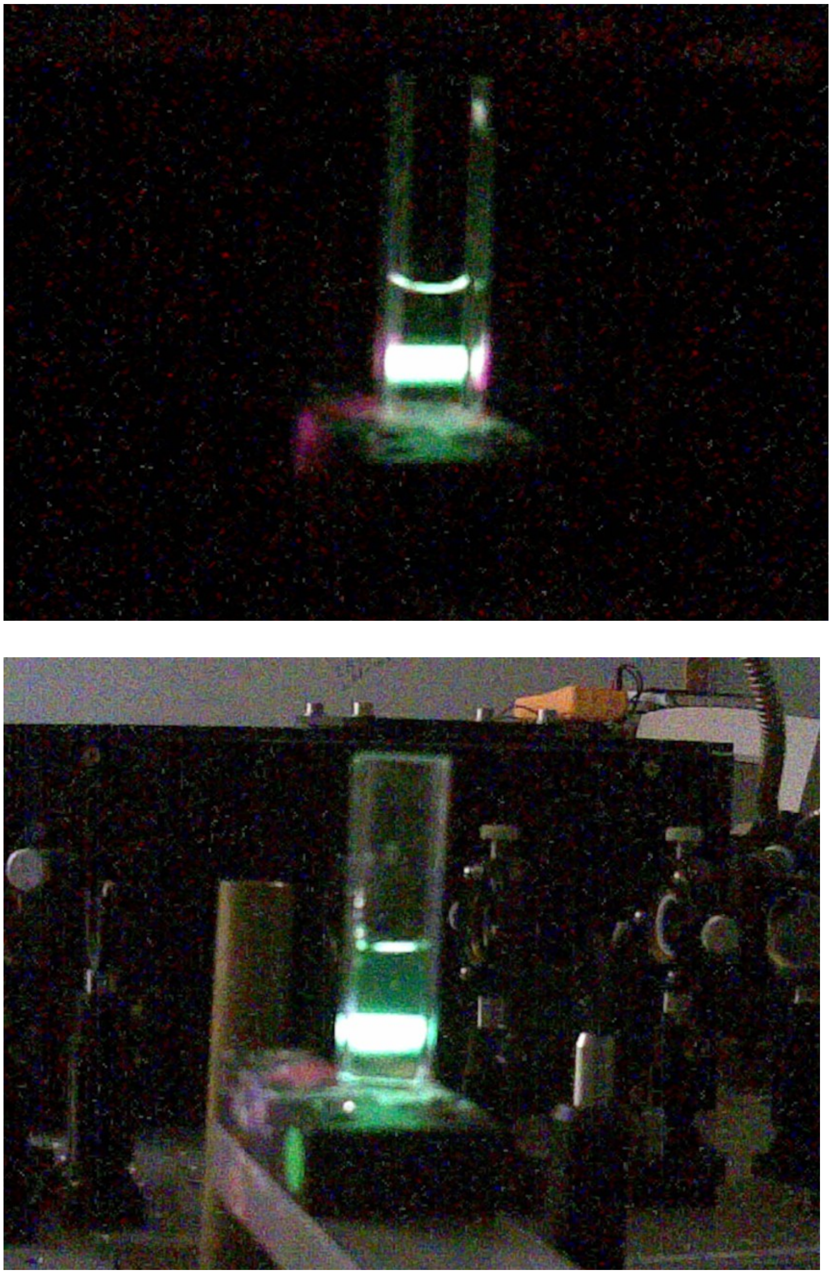

Figure 6.8. Pictures of the Cu-doped ZnSe/ZnS QDs-C excited with 800-nm, 1KHz-repetition-rate unfocused femtosecond laser pulses (a) without and (b) with room-light illumination.

6.5 Enhancement of PL by doping

As shown in Figure 6.8, the upconverted PL of Cu-doped ZnSe/ZnS QDs-C under 40-fs, 800-nm laser pulse excitation was much stronger than the room light. Under femtosecond laser pulse pumping, the multiphoton-photon-absorption-generated e-h pairs per QD per pulse are:

$$\frac{dN_c}{dt}=\frac{\sigma_n I^n}{n(\hbar\omega)^n}-\frac{N_c}{\tau_c} \tag{6.2}$$

where σ_n is the n-photon absorption cross-section; I is the pump light intensity; $\hbar\omega$ is the pump photon energy; τ_c is the free carrier relaxation time (usually is less than 1 ms but much longer than 40 fs). Therefore, within one pulse the last term can be neglected:

$$\frac{dN_c}{dt}=\frac{\sigma_n I^n}{n(\hbar\omega)^n} \tag{6.3}$$

The brightness of QDs solution is proportional to ηN_c, where η is the quantum yield of the QDs. There is no relationship between the brightness and lifetime of a sample. Therefore, the two-photon excited PL intensity is related to both two-photon action cross-section and QD concentration ($I_{PL} \propto \sigma_2\eta \cdot N$, σ_2 is the 2PA cross-section, and N is the QD number concentration). The quantum yields of one-photon-excited PL from QDs-A, -B and -C were determined to be 1.4%, 27% and 62% respectively. According to He. et al. [6.13], the quantum yields are almost identical under one-photon and two-photon excitations. As such, the 2PA cross-section is a sole unknown quantity. To precisely determine the 2PA cross-section, a standard sample (Rhodamine 6G, 10^{-4} M in methanol) was measured under the same experimental conditions. For Rhodamine 6G (R6G), the PL quantum yield, η_{R6G} and the 2PA cross-section, σ_2^{R6G} are known to be 0.95 and 2×10^{-48}

cm^4 s/photon at 800 nm, respectively [6.14]. The 2PA cross-sections of the QDs were determined by the utility ratio of PL signal from the QDs to R6G, $\sigma_2^{QD} N_{QD} \eta_{QD} / (\sigma_2^{R6G} N_{R6G} \eta_{R6G})$, where N_{R6G} is the concentration of R6G. The obtained 2PA cross-sections (σ_2) of these QDs were tabulated in Table. 6.1. The results clearly show that the 2PA cross-section of ZnSe/ZnS QDs is increased ~5 times by copper doping. This kind of enhancement is believed to originate from the Cu^{2+} enhanced defect states 2PA [6.15]. From Table 6.1 one also can see that as the size is reduced from 4.1 nm to 3.2 nm, the 2PA cross-section is reduced from 7.2 to 1.5 ($\times 10^{-49}$ cm^4s/photon) for the Cu-doped ZnSe/ZnS QDs. It means the 2PA cross-section decreases with decreasing QDs size.

Previously, some experimental observations showed that the 2PA cross-section of semiconductor QDs increased while decreasing the QDs size, which was attributed to an increase in exciton oscillator strength [6.16, 6.17]. However, these experimental observations were conducted at selected wavelengths and with a few QD sizes. Recently, more systematically experimental investigations clearly showed the general trend that the bigger the QD size was, the larger the 2PA cross-section became. Though the 2PA cross-section spectra have some featured resonance peaks with the sizes, these resonance peaks usually submerge to the overall trends with large QD size distribution [6.18-6.21]. This finding was also supported by theoretical calculations based on four-band-model and $k \cdot p$ method. The main reason is that the QD density of states is increased with QD's size [6.20, 6.21]. Our result is consistent with these findings.

The comparison between pure ZnSe/ZnS QDs-A and Cu doped ZnSe/ZnS QDs-B indicates that the 2PA cross-section is greater in the doped QDs in spite of the fact the size of the doped QDs (4.1 nm) is less than the undoped QDs (4.4 nm). This fact implies that the increase in the 2PA cross-section caused by doping is greater than the decrease induced by decreasing QD's size.

6.6 Time-resolved two-photon excited PL

The upconversion time-resolved PL setup is similar to the upconversion PL setup. Here the 800-nm, 200-fs excitation light pulses were provided by a Coherent Legend (seeded by Mira) operating at 1-kHz repetition rate. The collect PL was first dispersed by a monochromator and then monitored at different wavelength (± 5 nm) with a PMT coupled 400MHz oscillograph. Time resolution of the setup was ~15 nanoseconds (ns). The obtained 500-nm PL transient profiles of QDs-A, -B and -C are shown in Figure 6.9.

The PL transient profile can be analyzed with a multi-exponential equation:

$$I_{PL}(t) = \sum_{i=1}^{m} A_i \cdot \exp(-t/\tau_i) \tag{6.4}$$

where A_i is the amplitude and τ_i is the lifetime. Through best fitting, the obtained lifetimes for different process are listed in Table 6.1. Interestingly, as the majority of electrons were directly excited to the defect states through 2PA in Cu-doped QDs-C, the PL dynamics followed single exponential decay. This is consistent with its ultrahigh quantum yield. However, as the electrons were excited to the bandedge excitonic states in non-doped QDs-A and Cu-doped QDs-B, both the PL dynamics followed bi-exponential decay. In our experiments, the average number of electron-hole generated is less than one per QDs by utilizing low pump intensity. Therefore, the multi-exciton interaction processes are not important here. Note that an ultrafast dynamic process (less than 1 ns) should not be seen in the time-resolved PL spectra, due to our detection response time (~15 ns). These ultrafast processes include the relaxation of hot electrons from higher states to the bottom state within the conduction band or from the conduction band to the defect or surface-ralated states.

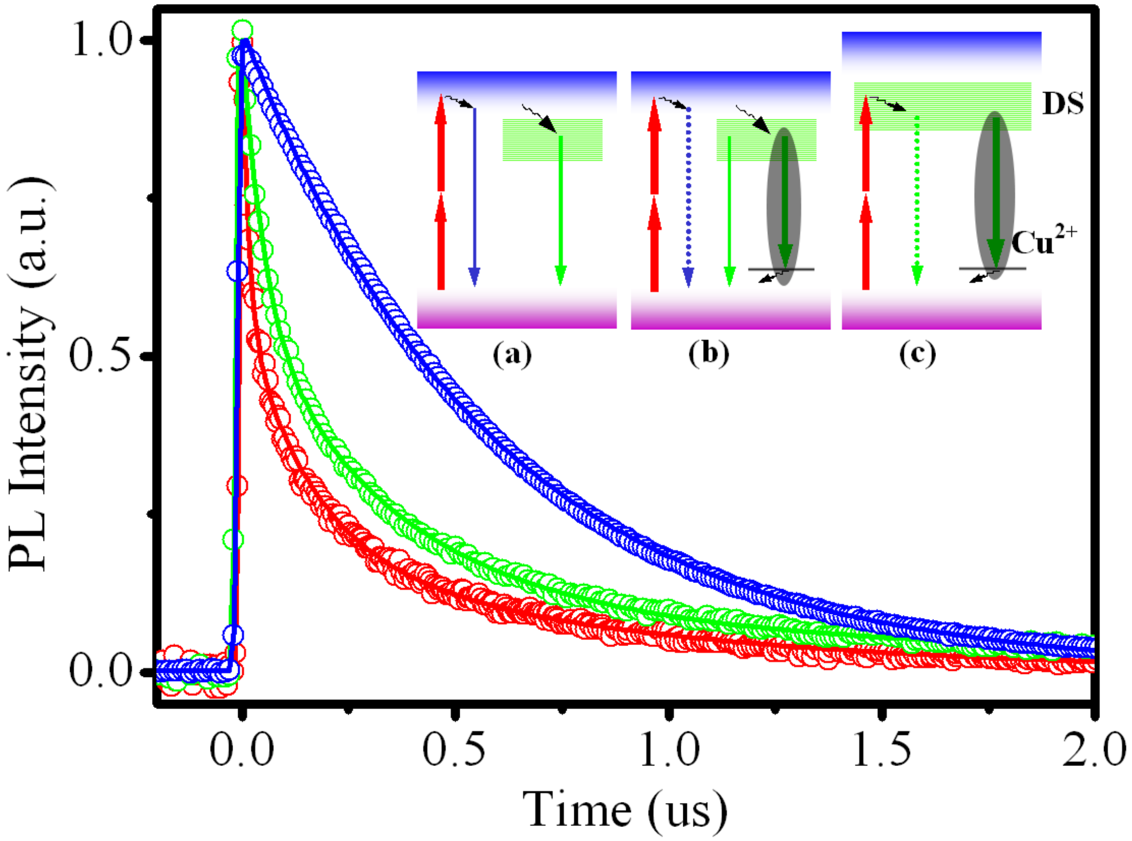

Figure 6.9. Two-1.55-eV-photon-absorption-induced 500 (± 5) nm PL decay curves and the multi-exponential fittings for 4.4-nm-sized ZnSe/ZnS (**Red**), 4.1-nm-sized Zn(Cu)Se/ZnS (**green**), and 3.2-nm-sized Zn(Cu)Se/ZnS (**blue**). The insets (a), (b) and (c) schematically illustrate the corresponding 2PA and electron dynamics through band edge and shallow traps (Blue, **I**), defect states (Green, **II**) and Cu-related states (marked in gray, **III**).

TABLE 6.1. Lowest excitonic transition, 2PA cross-section, quantum yield, bandedge, defect and copper related states PL dynamic constant and weightage.

	ZnSe/ZnS (A)	ZnSe(Cu)/ZnS (B)	ZnSe(Cu)/ZnS (C)
$1S_{1/2}(e)\rightarrow 1S_{3/2}(h)$ (eV)	3.2	3.4	3.96
2PA cross-section σ_2 (cm^{4}s/photon)	1.4×10^{-49}	7.2×10^{-49}	1.5×10^{-49}
Quantum yield (ŋ: %)	1.4	27	62
A_1	66%	×	×
τ_1 (us)	0.05	×	×
A_2	34%	73%	×
τ_2 (us)	0.58	0.13	×
A_3	×	27%	100%
τ_3 (us)	×	1.02	0.58

Experimental uncertainly: ±50%. Size dispersion of QDs: ≤20%.

In un-doped QDs-A, the 50-ns PL decay is originated from the bandedge state and shallow trap states emission. The 580-ns PL decay is assigned to the defect states emission [6.22]. The transition from the bandedge and shallow trap states emission to defect states emission can be clearly seen in the time-resolved PL spectrum (Figure 6.10 (a) and (b)).

In Cu-doped QDs-B, the lattice distortion enhances the defect states. The Cu doping also introduces new Cu related states. These enhanced defect states and Cu related states accelerate the electron trapping from the bandedge and shallow trap states to these states. Therefore, the bandedge and shallow trap states emission is almost invisible (See Figure 6.11 (a)). Furthermore, the Cu related states also trap the electrons from the defect states. Upon the Cu doping, the defect states emission is shortened to 130 ns in QDs-B. The copper related emission lifetime is around 1020 ns in these 4.1-nm-sized QDs.

In 3.2-nm-sized Cu-doped QDs-C, since most electrons were directly excited to the defect states, the processes of carrier-carrier scattering and phonon mediated charge carrier cooling within the conduction band are totally eliminated. Moreover, the process of phonon mediated charge carrier trapping from the band edge and shallow trap states to the defect states is also eliminated. This greatly reduces the other possibilities during the carrier relaxation from the initially excited states to Cu-related states. Finally, the stronger quantum confinement enhances the probability of capturing the carriers from the defect states to the Cu-related states compared with Cu-doped QDs-B. Therefore, the upconversion PL quantum yield is strongly enhanced as shown in Figure 6.7(a). The lifetime of the Cu related emission is also shortened to 580 ns for the stronger quantum confinement. This kind of shortening is similar to the observation on the lifetime shortening of Mn dopant emission in ZnS QDs [6.9].

The 2PA and 2PA generated electron dynamics processes are schematically showed in the inset of Figure 6.9 (a), (b) and (c) for the QDs-A, -B and -C respectively. For clear observation of above discussed processes, the short time range time resolved PL spectrum for corresponding QDs are shown in Figure 6.10(a), 6.11(a) and 6.12(a), and long time range ones are shown in Figure 6.10(b), 6.11(b) and 6.12(b), respectively. Figure 6.10(a) clearly shows there is a transition from the band edge states emission to the defect states emission in the undoped 4.4-nm-sized ZnSe/ZnS QDs-A. However, in the 4.1-nm-sized Cu-doped ZnSe/ZnS QDs-B, the band edge emission is so fast that it becomes invisible. The transition from defect state emission to Cu-related emission dominates in the time resolved spectrum (Figure 6.11). For 3.2-nm-sized Cu-doped ZnSe/ZnS QDs-C, the emission spectrum is much simpler and only mono exponential decreasing with time (Figure 6.12).

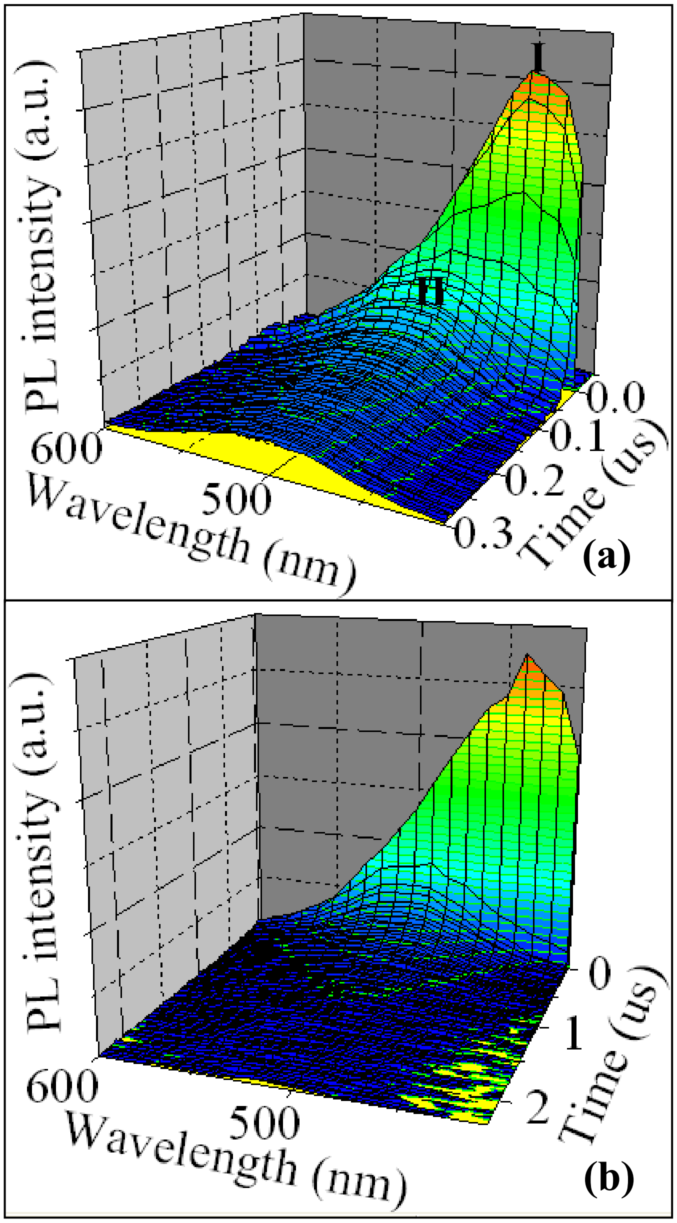

Figure 6.10. Temporal evolution of the 2PA-induced PL spectrum in (a) short time range and (b) long time range for 4.4-nm-sized ZnSe/ZnS QDs-A.

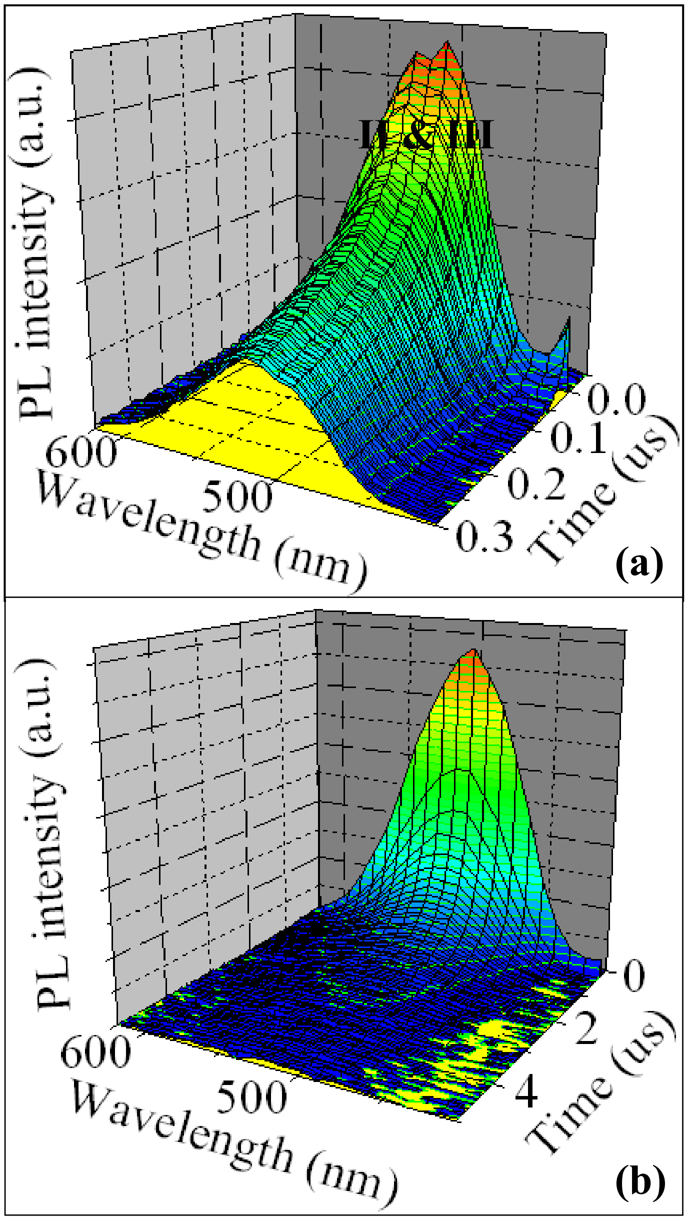

Figure 6.11. Temporal evolution of the 2PA-induced PL spectrum in (a) short time range and (b) long time range for 4.1-nm-sized Cu-doped ZnSe/ZnS QDs-B.

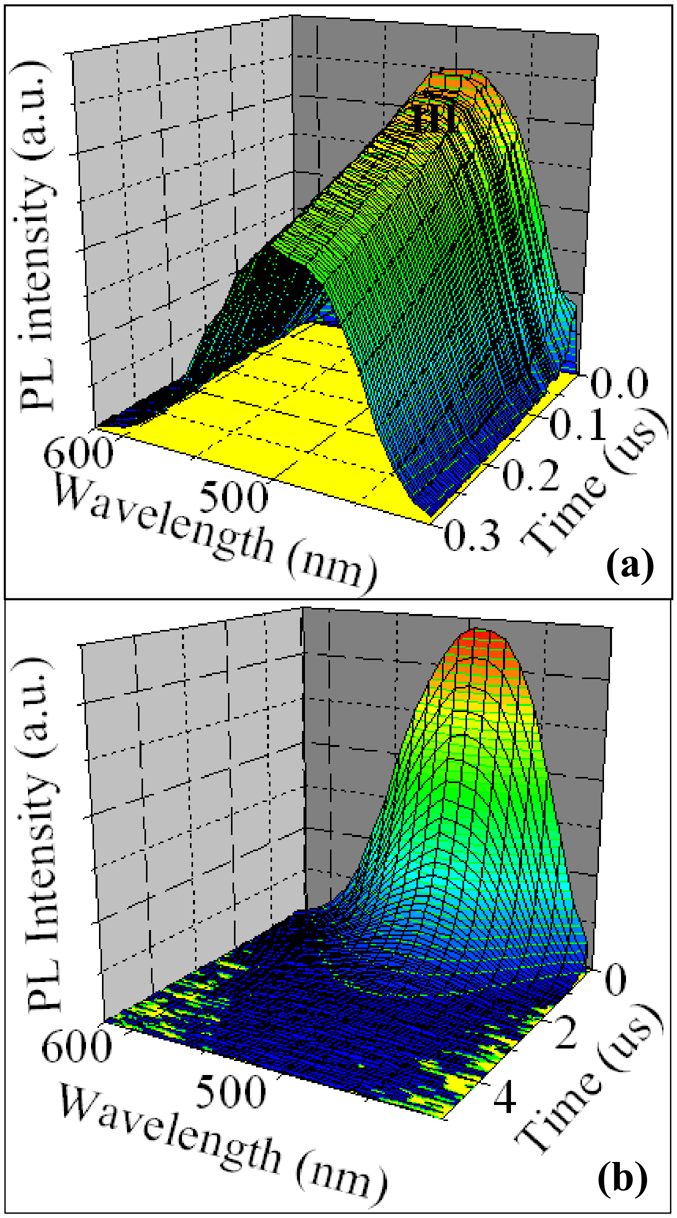

Figure 6.12. Temporal evolution of the 2PA-induced PL spectrum in (a) short time range and (b) long time range for 3.2-nm-sized Cu-doped ZnSe/ZnS QDs-C.

6.7 Conclusion

In conclusion, the upconversion PL of water soluble ZnSe/ZnS QDs can be greatly enhanced by Cu-doping at an optimal wavelength for commercial Ti:sapphire femtosecond lasers. This kind of enhancement can also be achieved by directly exciting electrons to the defects states, though 2PA cross-section is reduced due to the greatly enhanced quantum yield. By doing so, the 2PA generated electrons are near single exponential decay from the copper related defect states to t_2 energy level of Cu^{2+} ions. These experimental findings open a new approach for the application of Cu-doped semiconductor QDs into upconversion lasing, multiphoton imaging and optical data storage.

References:

[6.1] D. J. Norris, A. L. Efros, and S. C. Erwin, “Doped nanocrystals,” *Science* **319**, 1776 (2008).

[6.2] C. Wang, B. L. Wehrenberg, C. Y. Woo, and P. Guyot-Sionnest, “Light emission and amplification in charged CdSe quantum dots,” *J. Phys. Chem. B* **108**, 9027 (2004).

[6.3] N. Pradhan, D. Goorshkey, J. Thessing, and X. Peng, “An alternative of CdSe nanocrystal emitters: pure and tunable impurity emission in ZnSe nanocrystals,” *J. Am. Chem. Soc.* **127**, 17586 (2005).

[6.4] D. Yu, C. Wang, and P. Guyot-Sionnest, “n-Type conducting CdSe nanocrystal solids,” *Science* **300**, 1277 (2003).

[6.5] D. J. Norris, N. Yao, F. T. Charnock, and T. A. Kennedy, “High-quality manganese-doped ZnSe nanocrystals,” *Nano Lett.* **1**, 3 (2001).

[6.6] N. Pradhan, D. M. Battaglia, Y. Liu, and X. Peng, “Efficient, stable, small, and water-soluble doped ZnSe nanocrystal emitters as non-cadmium biomedical labels,” *Nano Lett*. **7**, 312 (2007).

[6.7] Al. L. Efros, E. I. Rashba, and M. Rosen, “Paramagnetic ion-doped nanocrystal as a voltage-controlled spin filter,” *Phys. Rev. Lett.* **87**, 206601 (2001).

[6.8] A. A. Bol and A. Meijerink, “Long-lived Mn^{2+} emission in nanocrystalline ZnS:Mn^{2+},” *Phys. Rev. B* **58**, R15997 (1998).

[6.9] C. Gan, Y. Zhang, D. Battaglia, X. Peng, and M. Xiao, “Fluorescence lifetime of Mn-doped ZnSe quantum dots with size dependence,” *Appl. Phys. Lett.* **92**, 241111 (2008).

[6.10] J. F. Suyver, T. van der Beek, S. F. Wuister, J. J. Kelly, and A. Meijerink, "Luminescence of nanocrystalline ZnSe:Cu," *Appl. Phys. Lett*. **79**, 4222 (2001).

[6.11] Y. Zheng, Z. Yang, Y. LI, and J. Y. Ying, "From glutathione capping to crosslinked, phytochelatin-like coating of quantum dots," *Adv. Mater.* **20**, 3410 (2008).

[6.12] G. C. Xing, W. Ji, Y. Zheng, and J. Y. Ying, "High efficiency and nearly cubic power dependence of below-band-edge photoluminescence in water-soluble, copper-doped ZnSe/ZnS quantum dots," *Opt. Express* **16**, 5710 (2008).

[6.13] G. S. He, K-T. Yong, Q. Zheng, Y. Sahoo, A. Baev, A. I. Ryasnyanshiky, and P. N. Prasad, "Muti-photon excitation properties of CdSe quantum dots solutions and optical limiting behavior in infrared range," *Opt. Express* **15**, 12818 (2007).

[6.14] M. A. Albota, C. Xu, and W. W. Webb, "Two-photon fluorescence excitation cross sections of bimolecular probes from 690 to 960 nm," *Appl. Opt.* **37**, 7352 (1998).

[6.15] G. C. Xing, W. Ji, Y. G. Zheng, and J. Y. Ying, "Two- and three-photon absorption of semiconductor quantum dots in the vicinity of half of lowest exciton energy," *Appl. Phys. Lett*. **93**, 241114 (2008).

[6.16] A. D. Lad, P. P. Kiran, D. More, G. R. Kumar, and S. Mahamuni, "Two-photon absorption in ZnSe and ZnSe/ZnS core/shell quantum structures," *Appl. Phys. Lett*. **92**, 043126 (2008).

[6.17] A. P. Alivisatos, "Semiconductor clusters, nanocrystals, and quantum dots," *Science* **271**, 933 (1996).

[6.18] G. S. He, K. T. Yong, Q. D. Zheng, Y. Sahoo, A. Baev, A. I. Ryasnyanskiy, and P. N. Prasad, "Multi-photon excitation properties of CdSe quantum dots solutions and optical limiting behavior in infrared range," *Opt. Express* **15**, 12818 (2007).

[6.19] S. C. Pu, M. J. Yang, C. C. Hsu, C. W. Lai, C. C. Hsieh, S. H. Lin, Y. M. Cheng, and P. T. Chou, "The empirical correlation between size and two-photon absorption cross section of CdSe and CdTe quantum dots," *Small* **2**, 1308 (2006).

[6.20] L. A. Padilha, J. Fu, D. J. Hagan, E. W. V. Stryland, C. L. Cesar, L. C. Barbosa, and C. H. B. Cruz, "Two-photon absorption in CdTe quantum dots," *Opt. Express* **13**, 6460 (2005).

[6.21] L. A. Padilha, J. Fu, D. J. Hagan, E. W. V. Stryland, C. L. Cesar, L. C. Barbosa, C. H. B. Cruz, D. Buso, and A. Martucci, "Frequency degenerate and nondegenerate two-photon absorption spectra of semiconductor quantum dots," *Phys. Rev. B* **75**, 075325 (2007).

[6.22] R. Sharma and H. S. Bhatti, "Photoluminescence decay kinetics of doped ZnS nanophosphors," *Nanotech.* **18**, 465703 (2007).

Chapter 7

Conclusions

The main objective of research presented in this thesis is to investigate the multiphoton absorption (MPA), and multiphoton excited charge carrier dynamics in ZnSe/ZnS and transition-metal-doped ZnSe/ZnS core/shell semiconductor QDs. The main results described in the previous chapters will be summarized in this chapter. The major contributions of this work are highlighted and suggestions for future work are also presented.

7.1 Summary and results

In the applications of semiconductor QDs in multiphoton bio-imaging, upconversion lasing and three dimension data storage, the two-photon absorption (2PA), three-photon absorption (3PA) in ZnSe/ZnS and Cu- and Mn-doped ZnSe/ZnS QDs were systematically investigated. Transition metal doping not only enhances the quantum yields of semiconductor QDs, but also enlarges the 2PA and 3PA cross-sections in the interested range of photon energies. The later is mainly caused by the introduced new doping levels as well as defect energy levels by the incorporated transition metal ions. The transition metal doping provides a new approach to manipulate the MPA cross-sections other than the size of semiconductor QDs. With this approach, the tailoring of the MPA cross-sections and emission wavelength could be realized with the addition of dopant and tuning of QD size. Furthermore, an experimental methodology has also been developed and demonstrated to separate the 2PA and 3PA contributions in semiconductor QDs when the excitation photon energy is near half of the bandgap.

As discussed in Chapter 3, 3PA and three-photon-excited photoluminescence (PL) of ZnSe/ZnS and Zn(Cu)Se/ZnS QDs in aqueous solutions have been unambiguously determined by Z-scan and PL measurements with femtosecond laser pulses at 1000 nm, which is close to a semi-transparent window for many biological specimens. The 3PA cross-section is as high as 3.5×10^{-77} cm^6 s^2 $photon^{-2}$ for the 4.1-nm-sized, Zn(Cu)Se/ZnS QDs, while their below-band-edge PL has a nearly cubic dependence on excitation intensity, with a quantum efficiency enhanced by ~ 20 fold compared to the undoped ZnSe/ZnS QDs.

Previous investigation of MPA in semiconductor QDs were mainly focused on 2PA in $\frac{E_g}{2} < \hbar w < E_g$ range and 3PA in $\frac{E_g}{3} < \hbar w < \frac{E_g}{2}$ range. However, when the photon energy is near half of the QD's bandgap, both 2PA and 3PA would contribute to the nonlinear absorption with equal significance. This scenario has never been previously investigated. In Chapter 4, we demonstrated that the 2PA and 3PA contributions to the semiconductor QDs in a matrix can be unambiguously determined under this situation. In the spectral region where the photon energy is greater than but near $E_0 / 2$, the 2PA coefficient is determined by open-aperture Z-scans at relatively lower irradiances, and the 3PA coefficient is then extracted from open-aperture Z-scans conducted at higher irradiances. At photon energies below but close to $E_0 / 2$, both open-aperture Z-scans and multiphoton-excited PL measurements have to be employed to distinguish between 2PA and 3PA.

With the methodology discussed above, the 3PA cross-sections of 4.4-nm-sized ZnSe/ZnS QDs and 4.1-nm-sized Mn-doped ZnSe/ZnS QDs were unambiguously determined in a wide spectral range (from 800 nm to 1064 nm) in Chapter 5. The two-photon-enhanced three-photon absorption in transition-metal-doped ZnSe/ZnS QDs was revealed by comparing the theoretically calculated 3PA cross-sections with the experimentally measured ones in the near infrared spectral region. Due to the degeneracy between two-photon transitions mainly to the states of dopants and three-photon transition to the excitionic state, the 3PA cross-section is enhanced by two orders of magnitude at 1064 nm. Taking into account of the enhancement in PL, such double enhancements make ZnSe/ZnS QDs doped with transition-metal ions a promising candidate for applications based on three-photon-excited fluorescence.

In Chapter 6, it was showed that the PL can be further increased by directly exciting electrons from the ground states to the defect states, rather than to the conduction bands in ZnSe/ZnS QDs. Although 2PA cross-section is reduced somewhat when the size is decreased from 4.1 nm to 3.2 nm, the overall two photon action cross-section ($\sigma_2\eta$) is increased at an optimal wavelength of commercial Ti:sapphire femtosecond lasers (800nm), due to the compensation of larger quantum yield. Moreover, the 2PA-generated electrons are nearly single exponential decayed with a lifetime of ~ 580 ns from the copper-related defect states to t_2 energy level of Cu^{2+} ions. These results could possibly lead to a new avenue for the applications of Cu-doped semiconductor QDs into upconversion lasing, multiphoton imaging and optical data storage.

7.2 Highlight of contributions

The major contributions of this thesis are summarized here.

- Provided an idea to tailoring the MPA cross-sections of semiconductor QDs with the transition metal doping. Many previous researches were focused on tuning the MPA cross-sections of semiconductor QDs with the size and different materials, while the idea of utilizing transition-metal-doping had never been reported.
- Development of a method to determine the 2PA and 3PA coefficients unambiguously when the excitation photon energy is in vicinity to half the semiconductor QDs.
- Investigation of 2PA and 3PA in ZnSe/ZnS and Cu- and Mn-doped ZnSe/ZnS QDs in a wide spectrum range. While previous experiments only characterized the 2PA and 3PA of ZnSe/ZnS at few selected wavelengths, the results obtained here are essential for applications of these high efficiency Cu- and Mn-doped ZnSe/ZnS QDs in multiphoton bioimaging, upconversion lasing and three dimension data storage.

7.3 Suggestions for future work

There are several interesting directions for future work in the areas of the research presented in this thesis.

One possible avenue of future work is to investigate the dependence of the MPA on doping concentration of transition metal ions in semiconductor QDs. In this thesis, the Cu^{2+} and Mn^{2+} doping concentration were restricted to 1%. However, the doped semiconductor QDs electronic energy levels and wavefunctions are strongly dependent on the doping concentration of transition metal ions. The MPA is determined by the electronic energy levels, wavefunctions and the selected excitation wavelength. Therefore, experimental investigation of this dependence is of crucial importance for the real applications of these doped QDs. However, the synthesis of different doping concentration semiconductor QDs is still a challenge.

Another direct extension of the work would be to perform the detail theoretically calculation of the 2PA and 3PA based on the real energy levels of the transition-metal-doped semiconductor QDs. Previous theoretical calculation of MPA in semiconductor QDs was mainly based on four band model or KP methods for strongly confined intrinsic semiconductor QDs. The extension of these methods to the transition-metal-doped semiconductor QDs will provide more useful and insightful understanding.

7.4 Conclusion

The thesis has systematically investigated the MPA and multiphoton excited charge carrier dynamics in ZnSe/ZnS and transition-metal-doped ZnSe/ZnS semiconductor QDs. The main contributions of the work are in the development of a method to clearly determine the 2PA and 3PA in semiconductor QDs and using this method to investigate the enhancement of MPA in a wide spectral range by transition metal doping.